Study on Metal-Ligand Interactions: Infrared Ion Spectroscopy of Coordination Compounds

by

Madison M. Foreman

B.S. University of Texas at Austin, 2018

A thesis submitted to the Faculty of the Graduate School of the University of Colorado in partial fulfillment of the requirements for the degree of Doctor of Philosophy

Department of Chemistry

2023

Committee Members:

J. Mathias Weber

Niels Damrauer

Joel Eaves

Veronica Vaida

Heather Lewandowski

Foreman, Madison (Ph.D., Chemistry, Department of Chemistry)

Study on Metal-Ligand Interactions: Infrared Ion Spectroscopy of Coordination Compounds

Thesis directed by Professor J. Mathias Weber

Coordination compounds are essential to a vast array of important areas of chemistry. They play catalytic and structural roles in biochemistry, perform industrial functions as catalysts, and participate in atmospheric reactions across the globe. The ubiquity of coordination chemistry is due to the ability of nearly all metals to form coordinated complexes with organic ligands, which allows chemical access to over half of the periodic table. Metal-ligand interactions govern many of these compounds' functions and influence the structure and charge distribution of the complex, making them vital to understand on a molecular level in order to progress our comprehension and development of coordination chemistry. Infrared (IR) spectroscopy offers a powerful probe into these molecular details. In solutions, analysis is complicated by interaction with the chemical environment and the speciation present in most applications. Mass spectrometric preparation of cold ionic complexes bypasses many of the solution-induced challenges in connecting IR spectroscopic information to detailed knowledge about complex molecular systems.

Bipyridines are a well-known class of CO_2 reduction catalysts that consist of a transition metal center surrounded by bipyridine-based ligands. We investigated how the addition of formate (a product of CO_2 reduction catalysis) to the complex changed the overall molecular structure, and how different metal centers bound to the formate adduct. This work elucidated the formate-metal binding motif and how it differs across metal centers. The charge distribution throughout each complex was found to be significantly influenced by the local

electronic geometry and consequent coordination chemistry of the metal, which illuminated the ligands' role as charge reservoirs.

EDTA is a prototypical chelator of metal cations and serves as a molecular model for protein binding pockets. We investigated EDTA bound to a series of alkaline earth metal dications and found that the size of the bound ion determines the geometry of the EDTA framework, impacting the dynamics and selectivity of the binding pocket. Upon successive hydration from one water molecule to full solvation, the binding pockets of each complex opened, further exposing the bound ion to the chemical environment. We then carried out measurements on a series of transition metal-EDTA complexes, in which we characterized the influence of d-electrons on the geometry of the EDTA chelator, spin state of each complex, and changes in EDTA spectral signatures.

The symmetric (ν_s) and antisymmetric (ν_{as}) OCO stretching modes of carboxylate containing compounds encode structural information that is both difficult to decipher and desirable to model due to the sensitivity of these spectral features to small shifts in charge distribution and structure, as well as the anharmonicities of these two vibrational modes. We have developed a relation between the frequency of these modes and the geometry of the carboxylate group, showing that the splitting between ν_s and ν_{as} can be accurately predicted based only on the OCO bond angle obtained from quantum chemical calculations (± 58 cm^{-1}, $R^2 = 0.992$). The relationship is shown to hold for IR spectra of carboxylato groups in a variety of molecules measured *in vacuo*.

We have collected and interpreted IR spectra on a variety of coordination compounds, identifying fundamental characteristics of their chemical abilities and developing a new model for spectral analysis. These advances will lead to more understanding and informed design of coordination compounds from biology to industry.

To all of my family, friends, and teachers who encouraged me to keep asking "why?".

Acknowledgements

This work has been a labor of love not only on my part, but also from the many supportive people that I have been so incredibly fortunate to be surrounded by.

First, I would like to thank Mathias, who has been a shining example of mentorship and grace since our first meeting. I was encouraged to join his group on the advice that he held his students to an extremely high standard, and did everything in his power to help them meet that standard. Those statements have held true. He possesses the unique talent of being able to get students to understand that they are capable of meeting the bar, no matter how high, and has consistently gone above and beyond to provide me with guidance and support over the years. He has given me not only technical training, but personal advice, words of encouragement, and plenty of puns and Star Wars jokes. Joining the Weber group is easily one of the best decisions I have ever made, and I am grateful that I had the opportunity to be a part of it.

The other members of this lab have all been a tremendous source of help and friendship. When I joined, the group consisted of three other graduate students — Wyatt Zagorec-Marks, Curtis Beimborn, and Rebecca Hirsch — as well as a post-doc, Leah Dodson. Wyatt was my predecessor on the instrument and trained me in nearly all aspects of the experimental and analytical methods that I have used to complete my graduate work. He is knowledgeable, gifted with teaching, and endlessly patient, which is everything one could want in a mentor. I am grateful not only for all of the in-lab training I received from him, but for the example he set in calmly and confidently addressing problems as they arose, with the mindset that anything could be fixed with enough skill, Swagelok, and epoxy. The piece of advice he most often gave me has proven true over the years, and bears repeating: “It’s a marathon, not a sprint.” Curtis worked on a different project in a different lab, and was always a breath of fresh air to visit with. He is now the head of the Keck Lab at JILA, and still comes by the group office

for lunch and to tell me that things in lab are probably going better than I think they are. Rebecca largely worked on separate projects than me, and we only overlapped instrumentally for a brief time. The time that we did not spend together in research we spent outside of lab on hikes, by fire pits, cooking way too much food, and ending workouts early to watch our favorite shows. Leah Dodson left the lab after my first year to start her own research group at the University of Maryland, and she made quite an impact on me in the time we worked together. In addition to her work ethic and brilliance, she was always willing to drop what she was doing to help me with a problem. To this day, she responds to my texts and emails no matter how inane my questions and hugs me at conferences.

In the time that I have been in Mathias's group, several fantastic students have joined: Heinrich Salzmann, River Leversee, Lane Terry, and Maddie Klumb. Heinrich has been an excellent lab mate. We worked on the same project for a time and dealt with many new challenges, and I greatly appreciated and admired his ability to remain upbeat and focused when faced with a conundrum. He knows how to tell just the right joke to boost morale and has spearheaded the revival of an entire instrument and line of research. River is also working on his project solo, and has made tremendous developments. He is genuinely one of the smartest, hardest-working people I have ever met, and his kindness and enthusiasm are a wonderful addition to the group. I have so enjoyed bonding with him over gluten-free Oreos and Thai food. Lane is my successor on the instrument, and I have no doubt that she will continue to succeed with it. She has already gathered an outstanding amount of data, developed an intuition for the experiment faster than I thought possible, and has brought such a brightness to the group with her personality. I am thankful that I had her as a trainee, as it isn't very hard to teach a person who picks everything up right away. More than that though, I really delighted in spending time with someone who possesses such a high degree of scientific and emotional intelligence. Maddie Klumb joined the group just as I was phasing out of lab to write, but we are desk neighbors and I have had the pleasure of sharing lunch and laughs with her on multiple occasions. She is bright and hardworking, and I look forward to hearing about all of the exciting research that she and Lane accomplish down the road.

There are many other JILAns that I am lucky to have crossed paths with. Nearly every staff member in the shops has fielded questions from me, and they have always done so with the upmost patience and passion for what they do. I would like to specifically acknowledge Jim McKown, Eric Alvarado, and J.R. Raith from the computing group, Terry Brown from the electronics shop, and Adam Ellzey, Hans Green, and James Uhrich in the machine shop for their consistent support over the years. The members of JILA that I have had the pleasure of working on service committees with have been wonderful, and I have learned so much from them. Beth Kroger has been a role model in compassion and effective communication and is an all-around lovely person. Andreas Becker has provided me with opportunities to lead and to learn, and has supported many efforts to improve the lives of the people he works with.

Outside of JILA, there are a few mentors without whom I would not be writing this dissertation. Dr. John Markert at UT Austin, my undergraduate Physics II professor, gave me a chance to join his lab at a time when I was unsure of my ability to succeed in science. I had been turned away from multiple research groups for lack of a competitive GPA, but Dr. Markert invited me to join his lab simply because I liked superconductors. He instilled in me the belief that scientists are people who are curious and willing to troubleshoot, and I will forever be grateful that he welcomed me into the world of research with open arms. Dr. John Stanton was also an undergraduate professor of mine; he was the first professor I had that held office hours 24/7. I often dropped by to ask about the homework, if orbitals were real, or if he'd read about any weird molecules recently (he always had). I thank John for convincing me that I not only *could* pursue a graduate degree, but should. I have had the great joy of seeing him on his regular visits to Boulder or at conferences, and am now collaborating with him on a paper — for which he assigned me homework.

Now, I would like to thank my family and friends. Rebecca, Max, Robyn, Morgan, and Kevin: thank you for being a family to me. You are all without a doubt the highest quality of human beings the world has to offer, and I am so honored to be your friend. To my sister, Jasmine: thank you for steadfastly believing that I can reach any goal, and for being an inspiration to do scary, exciting things. I look up to you so much for your bravery, perseverance, and never-ending good nature. To my parents: I cherish so much your good advice, boundless love and support, and that you always pick up the phone (even when I'm leaving campus at 5 am). Dad — thank you for showing me that the best kind of person to be is a people person, for raising me to be one, and for always letting me drive the golf cart. Mom — thank you for being my first teacher. For teaching me to think for myself, pay attention, appreciate good food, and love creepy crawlies, and that I can always count on you. Through all of the days that we spent in the kitchen and the backyard — you made me a scientist.

Contents

List of Tables

List of Figures

List of Schemes

1. Introduction

The study of large, complex molecules in the gas phase at times seems oxymoronic to me, which makes for a very fascinating puzzle. Each of the compounds examined in this dissertation exists primarily in solution, at room temperature, with a variety and abundance of other chemical species in the mix, possibly with an electric current flowing through it. The search for a deeper understanding of underlying chemical and physical properties in these bulk systems requires consideration and control of a great many variables, nearly all of which affect the species of interest, the application of measurement techniques, or both. We circumvent many of these complications by bringing isolated chemical targets into the gas phase, thereby allowing us to pare things down and probe for specific molecular-level details related to their functionality. In short, we devote time and consideration to learning about the typical environments in which these compounds live and work — so that we may then promptly strip it all away. Studying molecules with this approach — shifting from the macro- to the nanoscale — provides a multitude of opportunities for exploration and instills an appreciation for tiny forces with big effects.

A wide array of important chemistries, from biochemical transport of ions and gases to industrial electrocatalysis and contaminant sequestration, are performed by coordination compounds. The ubiquity of coordination chemistry arises from the fact that nearly all metals can form coordinated complexes with organic ligands — providing chemical access to over half of the periodic table. Metal-ligand interactions are at the core of many of these compounds' functions; they exert influence on molecular geometry and charge distribution, which in turn govern bonding, reactivity, and solubility. Thorough, precise knowledge about these systems is essential in furthering our comprehension and development of coordination chemistry. Towards this goal, we employ infrared spectroscopy as a powerful probe into metal-ligand interactions. Vibrational spectra indirectly encode the very information we are interested in — structure and charge distribution — and can provide detailed knowledge about complex molecular systems.

As mentioned above, these compounds are difficult to study in the condensed phase. In most circumstances, coordination complexes are subject to an ever-evolving chemical environment, as is certainly the case for catalysts and biomolecules. Solvents and other solvated species not only interact with the target molecule itself, but with any means of measurement. Speciation in solution can involve (but is by no means limited to) the presence of free ligands and metals, mixtures of isomers, and multiple charge states — all of which may produce a spectroscopic response and alter that of other species. Spectra taken from such solutions can contain several different signatures that are entangled to the point of rendering the spectrum uninterpretable, the spectral congestion hindering comparison with other data or with calculations. Furthermore, condensed-phase spectroscopy is often carried out at room temperature where thermal excitation leads to broad absorption bands without resolvable detail. Gas-phase analysis offers answers to several of these difficulties in the form of cold ionic complexes prepared by way of mass spectrometry and buffer gas cooling. Mass-selection circumvents many speciation-induced hurdles by supplying precisely selected species of interest, and cryogenic temperatures ensure that molecules are in their vibrational ground state. These methodologies combined provide the ability to connect infrared spectroscopic information to detailed knowledge about complex molecular systems — the overarching theme of this dissertation.

This body of work comprises infrared photodissociation spectroscopy experiments conducted on a number of coordination complexes of fundamental and applied interest prepared in the manner described above, as well as a brief foray into pen-and-paper theory. A detailed account of the experimental methods utilized is given in Chapter 2, Chapters 3 and 4 each focus on a different coordinating organic framework investigated in a range of chemical contexts, and Chapter 5 illustrates a model for connecting carboxylate infrared signatures to specific structural information. The first experiments presented involve catalyst species composed of metal centers bound to ligands in the bipyridine family, which are well-known for their role in CO_2 reduction catalysts. Chapter 3 explores two avenues: the addition of a formate adduct to the catalyst, and the effects of different metal centers (Co, Ni, and Cu) on the complex. Chapter 4 focuses on EDTA, one of the most widely used chelating agents in the world and a useful model system for the ion binding pocket in certain proteins. Infrared spectra were collected for EDTA bound to a series of alkaline earth metal atoms (Mg, Ca, Sr, Ba), as well as the microhydrated and fully solvated species thereof. Additionally, experiments were carried out on compounds of EDTA coordinated to a variety of dicationic first-row transition metals (Mn, Co, Ni, Cu, Zn). Lastly, Chapter 5 puts forth a semi-empirical model relating carboxylate stretching modes to the O–C–O bond angle. Through the lens of normal mode analysis, a discussion is presented on the relation and its physical origins.

2. Methodology

I. Instrumentation

In this chapter, an overview of the experimental procedure is given. More in-depth discussion is presented for select processes that the author believes deserve individual consideration regarding the work described in this dissertation.

a. Overview

The aim of our experimental setup is to measure well-resolved infrared spectra of mass-selected ionic species in the gas phase. To this end, the experimental apparatus consists of four main operational stages: ion production, cluster preparation, mass selection, and spectroscopic analysis, as shown in Figure 2.1. [1]

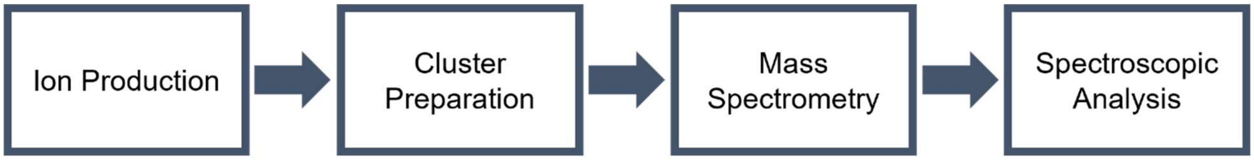

Figure 2.1. Block diagram of experimental process. From left to right: Ions are first produced via electrospray ionization and guided through a differential pumping scheme by a series of ion skimmers and multipole ion guides. Next, ions undergo collisions with a buffer gas in a cryostat-mounted Paul trap, where they are cooled and tagged with neutral messenger molecules. So-prepared clusters are ejected into a time-of-flight mass spectrometer and investigated using infrared photodissociation spectroscopy.

Electrospray ionization is used to generate charged microdroplets of sample solutions. These aerosolized particles travel to and through a desolvation capillary, losing solvent molecules along the way and leaving only bare gas-phase ions. The ions are then transported through multiple differential pumping stages by a series of ion skimmers and multipole ion guides, which serve to collimate and direct the ion beam, respectively, until the ions arrive in a cryogenically cooled Paul trap. Here, the ions are cooled via buffer gas collisions and form clusters with neutral, weakly bound molecules (see Section c.1.). These ion-tag clusters are then ejected from the trap into the acceleration region of a Wiley-McLaren time-of-flight mass spectrometer. [2] A pulsed mass gate is used to select ionic clusters by their mass-to-charge ratio, after which they are irradiated with the output of a tunable infrared optical parametric converter system. Upon absorption of a photon, the acquired vibrational energy is redistributed throughout the cluster, causing the loss of the tag molecule. The resulting photofragments – fragment ion and neutral tag – are separated from one another and from undissociated parent clusters by a two-stage reflection, and the target ions are directed into a microchannel plate detector. Intensity of the fragment ion signal is measured as a function of photon energy and processed by normalizing to the measured photon fluence and subtracting shot-for-shot background signal arising from random noise and unimolecular or collision-induced decay of clusters. Numerous spectra are collected over several days to ensure reproducibility, and the spectra are averaged to improve the signal-to-noise ratio. A top-down view of the instrument is shown in Figure 2.2.

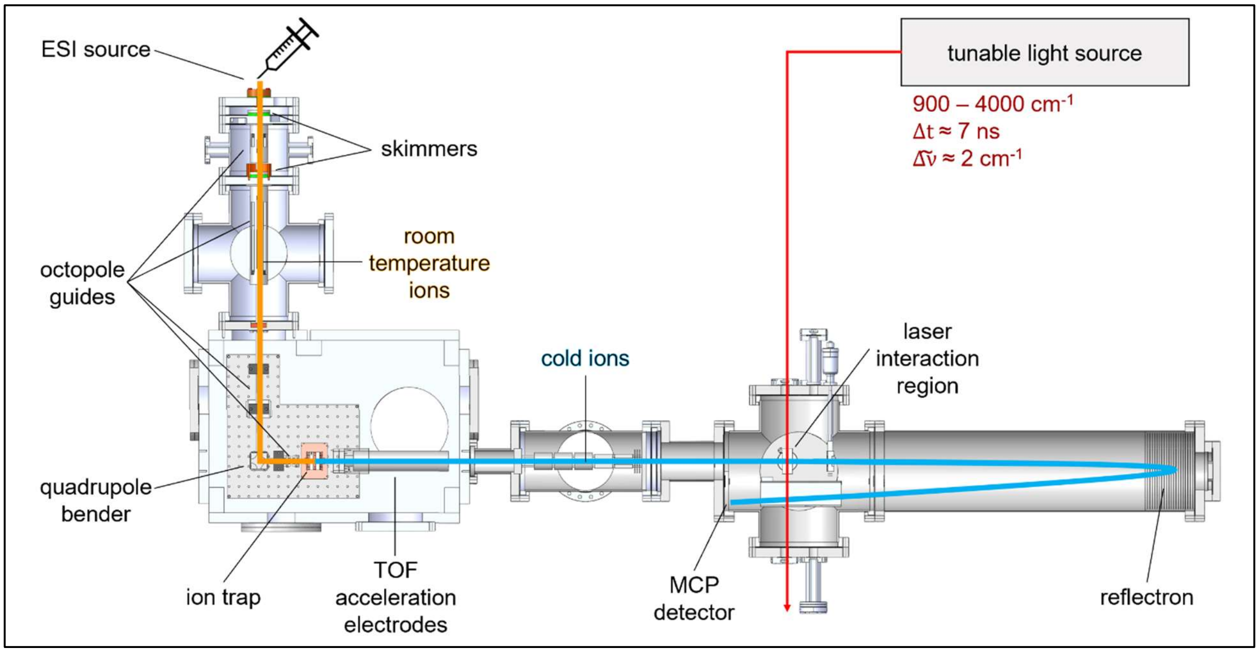

Figure 2.2. Top-down view of the experimental apparatus used in this work.

b. Ion Production

b.1. Electrospray Ionization

Here, we discuss the experimental rationale for employing electrospray ionization before describing its procedural mechanics. Electrospray ionization (ESI) stands out among the assortment of available ion generation techniques for its ability to introduce large, often multiply charged molecules into the gas phase. [3] Additionally, it allows preparation of gas phase ions as close as possible to their solution phase state. The development of electrospray ionization in the 1980s revolutionized the field of mass spectrometry, and its creator, John Fenn, was awarded the 2002 Nobel Prize in Chemistry for the innovation of this powerful technique. [4] ESI has since gained widespread appreciation for its myriad applications and unique experimental benefits.

Ion sources can be generally classified as performing "hard" or "soft" ionization. Hard ionization methods impart large amounts of energy into target samples, often resulting in fragmentation of the molecules and yielding a high number of low-mass fragments. Soft ionization methods are less prone to causing fragmentation, which results in wholly intact, charged molecules and high-mass fragments. As a soft ionization technique, ESI allows us to study large, intact chemical systems even if they are rather delicate.

A unique ability of ESI is the creation of highly charged ions, which offers several experimental advantages. Ion detectors for mass spectrometry report on ions within a certain range of mass-to-charge (m/z) ratios. Generation of highly charged ions via ESI makes feasible analysis of heavy species that would otherwise be outside detection limits by increasing the charge on the molecule, lowering its m/z ratio, and thus effectively increasing the mass range of the detector. Additionally, ESI has opened the door to investigation of systems that exist in their native environments as highly charged ions by giving researchers the means to bring those ions into a controlled, gas-phase environment. For chemical species that have multiple possible charge states, ESI can afford access to many differently charged ions at once, permitting comparison across different charge states of the same molecule.

The production of ionic species via ESI occurs by two main channels: accessing pre-existing ions in solution or altering molecular charge during the electrospray process. The primary method employed in this work is the former.

The preparation of analyte solutions is the first step in an ESI experiment. Choice of solvent is governed largely by polarity and volatility, with additional (but minor) consideration paid to viscosity and surface tension. Polar solvents are used because of their compatibility with ionic analytes and their electrical conductivity, and volatile solvents benefit the ion intensity by evaporating from the microdroplets faster than solvents with low vapor pressure. Excessively high or low viscosity and surface tension may negatively impact the spray process. Typical solvents employed in ESI are acetonitrile, methanol, ethanol, and water; often, a mixture of solvents is used to tune ion solubility and solvent volatility for a given analyte solution.

Prepared sample solutions are fed through the highly charged ESI needle assembly (biased at ca. 2-4 kV magnitude) positioned a few millimeters from the opening of the desolvation capillary (biased ca. 0.1 – 0.5 kV magnitude). The drastic voltage difference between the needle and desolvation capillary creates a very strong electric field at the tip of the needle. The needle assembly consists of a fused silica spray capillary (75 mm ID, 193 μm OD, Polymicro Technologies) housed in a stainless-steel external sheath (Analytica of Branford) that allows optional use of an N_2 nebulizing gas to aid in spray production. At the outlet of the spray capillary, electrically conductive solution is exposed to the strong electric field. The strong electric field pulls liquid away from the capillary tip, forming a Taylor cone, from which a jet of liquid is generated, and ultimately producing a plume of charged droplets (see Figure 2.3). As these droplets travel through the ambient environment and desolvation capillary, solvent molecules evaporate. The droplets decrease in size until the electrostatic repulsion between particles with like charges overpowers the surface tension holding the droplet together, at which point Coulomb fission occurs. The desolvation-fission process repeats until, finally, gas-phase ions are formed. The ions pass through the desolvation capillary, a focusing lens, and a series of skimmers (stainless steel, 1.5 mm ID) and multipole ion guides before reaching the ion trap.

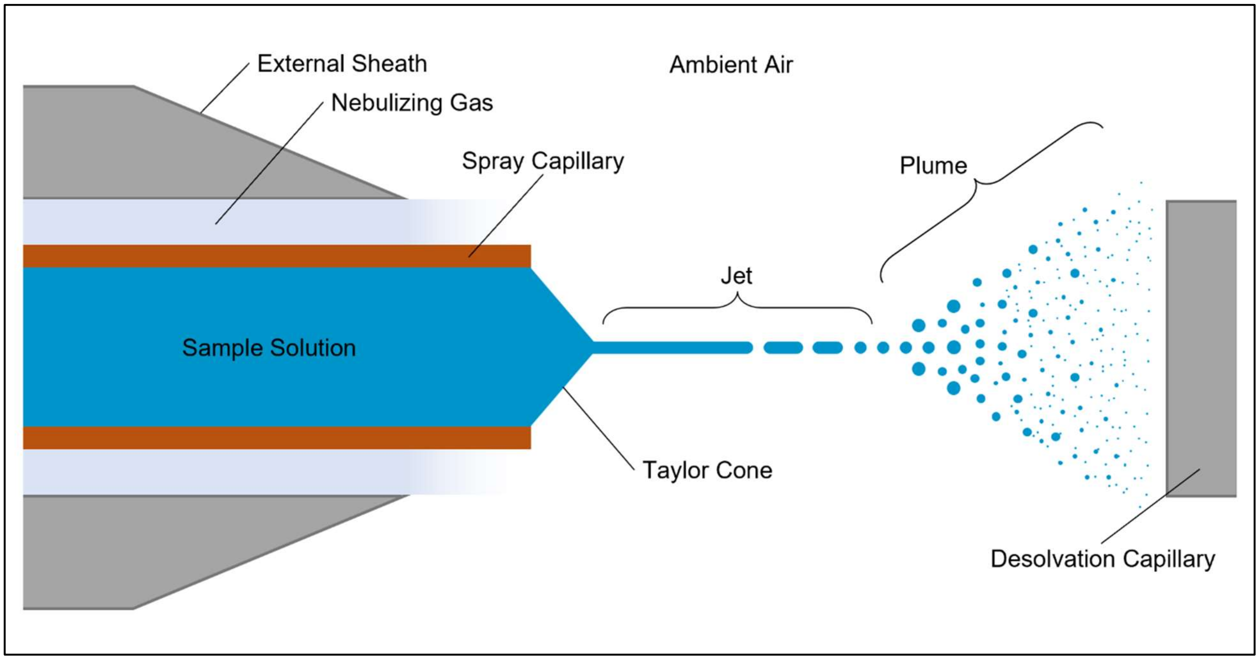

Figure 2.3. Schematic setup of the electrospray region. Sample solution is passed through the spray capillary and exposed to a strong electric field. A Taylor cone is formed, followed by emission of a jet and then formation of the aerosol plume.

b.2. Octopole Ion Guides

Multipole ion guides are employed ubiquitously in mass spectrometry to radially constrain charged particles around a desired beam path, effectively transporting ions with minimal loss. Multipole ion guides generally consist of an even number of metal rods – which may be round, rectangular, or hyperbolic – arranged symmetrically around a central axis. The instrument described in this work utilizes octopole guides constructed from 8 round stainless-steel rods.

The fundamental operating principle of multipole ion guides is the use of alternating electric fields to constrain ions in two Cartesian dimensions (typically the two dimensions which comprise the radial plane of a cylindrical guide), allowing movement along the third dimension. This strategy was developed as a superior alternative to focusing elements that rely only on electrostatic fields, the utility of which are limited by Earnshaw's theorem: "it is impossible to place a collection of bodies, subject only to electrostatic forces, in such a way that they remain in a stable equilibrium configuration." [5] While this statement does not explicitly preclude the focusing of moving ions with purely electrostatic potentials, lens-type optics are less adept at guiding ions with broad kinetic energy distributions over long distances and from high- to low-pressure regions without significant signal loss.

The effective electric field within a multipole ion guide is created by applying voltages of equal magnitude and opposite polarity to alternating rods around the central axis. As shown in Figure 2.4, this scheme places a positive potential on half of the rods, and a negative potential on the others. Were this a DC field, ions would collide with rods of attractive potential. Constraining ion motion is achieved by switching the polarity of each applied voltage at a set radio frequency (RF) (ca. 10 MHz in this instrument), whose time scale is very short compared to the typical time for motion of ions between rods. At any given point in time, ions are being accelerated toward the set of rods with an attractive potential. Before they collide with the rods, the polarity of the applied voltages is changed, diverting the ions toward the other set of rods. By optimizing the magnitude of the applied voltage (RF amplitude) and the oscillation rate of the rods' polarity (RF frequency), the ions can be prevented from colliding with the rods and converged along the center axis of the multipole in a time-averaged potential energy landscape that creates a minimum energy region around the multipole axis.

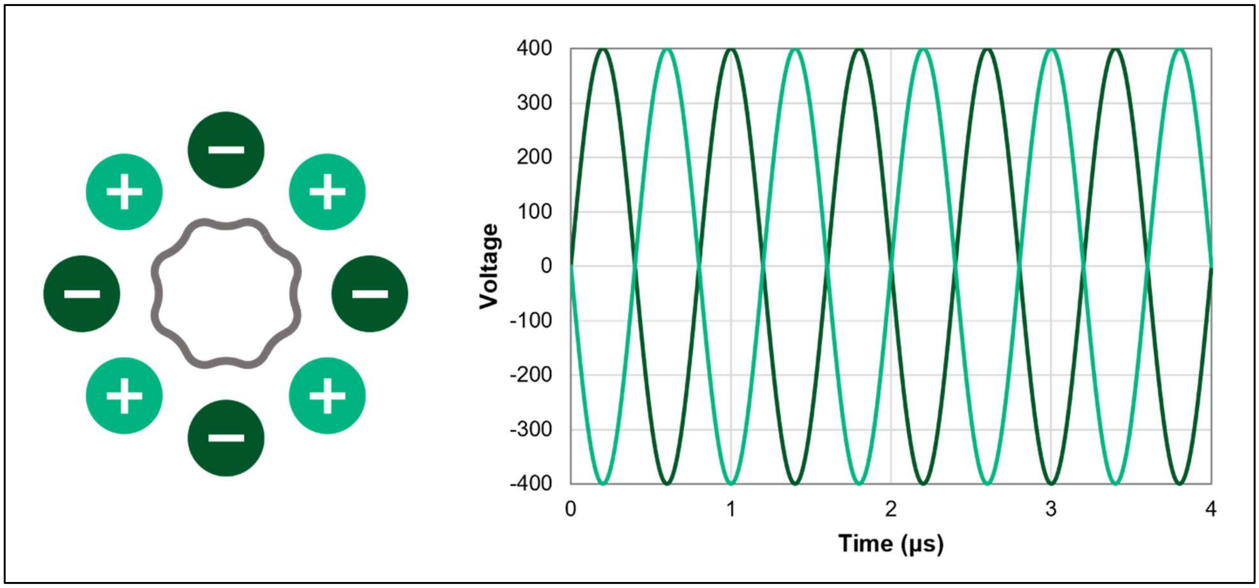

Figure 2.4. Left: Arrangement of rods around the central octopole axis with alternating opposite polarities. The effective electric field experienced by the ions is represented by the internal gray line. **Right:** The voltage fluctuation experienced by each set of rods as a function of time when the polarity of each potential is switched at a rate of 10 MHz.

b.3. Quadrupole Bender

While multipole ion guides are typically straight, certain functions require a bent ion guide. The instrument described in this work includes a bent quadrupole ion guide (bender) whose purpose is to remove any neutral particles or large droplets that may remain in the molecular beam before injection into the ion trap; neutral molecules may participate in unwanted collisions with ions in the trap or flight tube. The bender is able to deflect ions along its ca. 90° turn, but neutrals will not respond to the electric field, instead continuing to travel straight until they strike the wall behind the bender. In this way, the potentially detrimental neutral particles are removed from the molecular beam while maintaining the population of analyte ions in the beam.

c. Cluster Preparation

c.1. 3D Paul Trap

The trapping and storage of ions relies on the use of RF fields to spatially control ions, similarly to the strategy discussed previously for multipolar ion guides. However, ion trapping requires confinement of ions in all three dimensions, thus requiring different electrode geometries. While there exists a variety of trap geometries, the experimental apparatus used in this work contains a 3D Paul Trap. This hyperbolic quadrupole ion trap was developed in the late 1950's by Wolfgang Paul, earning him the 1989 Nobel Prize in Physics. Figure 2.5 shows the hyperbolic ring electrode and two hyperbolic endcap electrodes that comprise the Paul Trap.

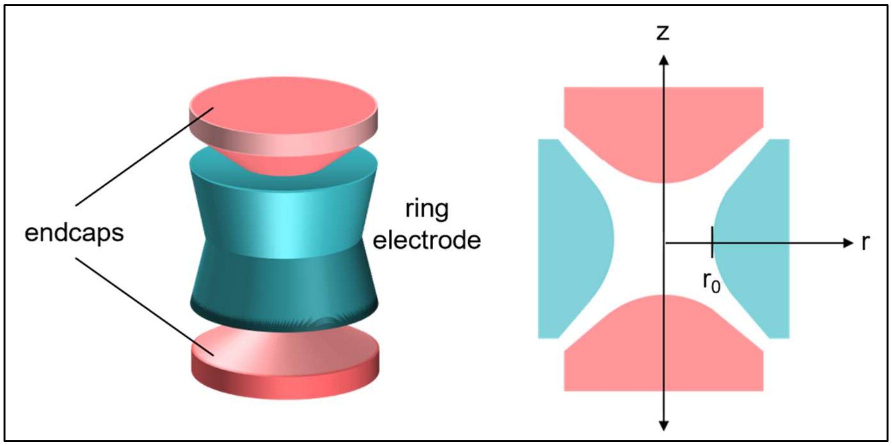

Figure 2.5. Left: Simplified depiction of 3D Paul Trap geometry, showing both endcap electrodes and central ring electrode. **Right:** Cross-sectional view of the trap denoting z and r axes, as well as the distance between the center of the trap and the inside of the ring electrode, r_0.

The 3D Paul trap generates internally a quadrupolar potential ϕ, which can be described in Cartesian coordinates by the following equation, where A and C are constants:

$$\phi(x, y, z) = A(\lambda x^2 + \sigma y^2 + \gamma z^2) + C \tag{1}$$

This expression can be modified by the application of Laplace's equation and careful choice of the coefficients λ, σ, and γ to yield a potential that is most suitably described in a polar coordinate system:

$$\phi(r, z) = A(r^2 - 2z^2) + C \tag{2}$$

A full derivation of the equations of motion for ions within the trap is beyond the scope of this dissertation, but a brief overview is given to explain the stability, and thus successful trapping, of ions. The acceleration of an ion inside of the trap can be expressed in the form of Mathieu's differential equation, shown here for motion along the z-axis:

$$\frac{d^2z}{dt^2} + (a_z - 2q_z \cos 2t)z = 0 \tag{3}$$

where a_z and q_z are parameters. Radial motion can be characterized analogously. Solutions to the Mathieu equation obtained for any given values of a and q are generally referred to as Mathieu functions. A consequence of Mathieu's equation being a second order differential equation is that there exist two independent solutions. If q is real, specific values of a will produce one solution that is periodic in nature, and one nonperiodic solution (this is essentially a summary of Floquet's and Ince's theorems). The periodic solutions are stable – that is, bounded. The nonperiodic solutions are unstable – they are unbounded, approaching infinity in z or r over time. If an ion's equation of motion is stable, it will remain trapped, while ions with unstable equations of motion will stray from the center of the trap and collide with the trap electrodes or be ejected out of the trap. One can use Mathieu functions to construct stability diagrams that graphically depict whether an ion will be successfully trapped in the z- and/or r-dimensions as a function of the a and q values associated with its equation of motion. Simplified expressions for q and a are shown in eqs. 4 and 5. Both coefficients depend on the mass-to-charge ratio of the ion (usually denoted m/z but labeled in this section as m/Q for clarity) and the RF frequency (Ω), but only q is linearly proportional to the RF amplitude applied to the trap (V), while only a is linearly proportional to the DC offset (U).

$$q \propto \left|\frac{e}{m} \cdot \frac{V}{\Omega^2}\right| \tag{4}$$

$$a \propto \left|\frac{e}{m} \cdot \frac{U}{\Omega^2}\right| \tag{5}$$

Mathematically describing the motion of ions within a trap is nontrivial, requiring a compilation of several periodic functions for both the z- and r-dimensions. The frequencies of each of these functions are called secular frequencies, integer multiples of the fundamental (lowest) frequency which predominates. A secular frequency depends on both an ion's mass-to-charge ratio as well as the applied RF amplitude. The maximum possible secular frequency for an ion occurs at bounds of the Mathieu functions: the high-amplitude limit of q and the low-voltage limit of a.

Since a quadrupole ion trap utilizes rapidly oscillating electric fields in much the same way as a quadrupole guide, the field inside of the trap is similarly time-averaged to effectively provide a constant restoring force toward the center of the trap. This restoring force can be modeled as a harmonic pseudopotential well, with the depth of the well correlating to how strongly an ion is held in either dimension. From this approximation, two valuable relations pertaining to the well depth, D_z and D_r (in axial and radial directions, respectively), can be extracted:

$$\overline{D_z} \propto \frac{e}{m} \cdot \frac{V^2}{\Omega^2} \tag{6}$$

$$\overline{D_z} = 2\overline{D_r} \tag{7}$$

Major consequences of these expressions include:

i. All else constant, lower m/Q ions are held more strongly than higher m/Q ions.
ii. All else constant, higher RF amplitudes trap ions more strongly.

iii. If V/Ω^2 is held constant, a higher RF frequency will lead to stronger ion confinement.

iv. Ions are confined more strongly axially than radially, making ion loss more likely in the r-dimension than the z-dimension.

The quadrupole ion trap used in this work consists of three copper electrodes — central ring electrode and two hyperbolic endcaps — spaced by ceramic rings. The trap is mounted on the cold head of a closed cycle helium cryostat (Sumitomo F-70L, 1.5 W at 4.2 K) via a sapphire place and OFHC copper mounts. It is equipped with a resistive heater to allow temperature control from 4 – 300 K and is enclosed in an electrically grounded OFHC copper heat shield (l: 66.6 mm, w: 90 mm, h: 95.2 mm) mounted to the outer edge of the cold head (ca. 40 K).

c.2. Ion Injection

Ion traps must be provided with ions in some manner, and there exist two approaches to do so: internal or external ionization. Internal ionization refers to creating ions within the trap, often accomplished by filling the trap with neutral molecules and then ionizing them via electron impact. External ionization is the practice of creating ions elsewhere in the apparatus and then injecting them into the trap – this is the strategy used for this work. In our experimental setup, ions are generated via electrospray ionization and then transported into the Paul trap through holes in the endcaps. There are a variety of factors to consider regarding the injection of ions into a quadrupole trap. Discussed herein are the kinetic energy of the incoming ions, usage of a buffer gas, and the phase angle of the RF field.

The kinetic energy of externally produced ions plays a large role in determining whether or not those ions will be successfully trapped. For an ion to be injected into the trap, it must have enough kinetic energy to overcome the potential energy barrier at the boundary of the trapping field. As a consequence, the ion will then also have enough energy to escape the trapping field by overcoming that same barrier at the exit aperture of the trap. In order to introduce ions into the trap and keep them there, their kinetic energy must be damped after injection. It is therefore desirable to minimize the kinetic energy of incoming ions, reducing the amount of energy that must be removed from them in the trap. As such, a conscious effort is made to maintain relatively low potential differences between many of the ion guides between the ESI source and the trap, in order to lessen the energy conferred to the ions during their transport.

The reduction of an ion's kinetic energy after it has entered the trap is achieved largely via collisions with neutral buffer gas molecules – typically He, D_2, or mixtures thereof. The buffer gas is in thermal equilibrium with the walls of the trap, which may vary from room temperature to cryogenic temperatures. Once ions are injected into the trap, their kinetic, vibrational, and rotational energy is brought close to thermal equilibrium with the buffer gas via repeated elastic collisions. Kinetic energy is transferred from the ions, allowing for stable ion trapping. In our experiments, buffer gas is admitted into the ion trap at the same time as the ions by a pulsed valve (Parker General Valve Series 99), and the ions are held in the trap for 45 or 95 ms depending on the repetition rate of the experiment (20 Hz or 10 Hz, respectively).

Injection efficiency is also affected by the phase angle of the trap's RF field. During the negative portion of the RF, anions are repelled from the entrance of the trap, while cations are accelerated into the trapping field. The inverse applies for the positive portion of the RF. For both cases, the phase angles that are amenable to trapping are quite narrow. In the case of continuous ion collection, as performed in this work, the cyclic and scarce acceptance of ions results in relatively low injection efficiency. This small window in which ions can travel across the threshold of the trap also affects ion ejection. A strategy employed in this work to combat this is the pulsed ejection of ions from the trap. When the ejection pulse is triggered, the voltage of the endcaps is increased sharply, with the entrance gaining a repulsive potential, and the exit an attractive potential. Ions are pushed from the trap synchronously with damping of the RF amplitude down to the ring bias potential, improving the ejection efficiency of the ion packet.

c.3. Ion Tagging

One of the primary advantages of using a cryogenically cooled ion trap is the ability to attach weakly-bound neutral adducts (often referred to as tags or messenger molecules) to ions of interest. The utility of this approach will be elaborated upon in part I.e., while the process of tagging ions is discussed here.

Tagged ion complexes are formed via three-body ion-tag collisions wherein the internal energy after complex formation does not exceed the binding energy of the tag. [6] This requires the ions to be relatively cold, as typical binding energies of these complexes are on the order of 10^2 – 10^3 cm^{-1}. [6-8] Traps are typically held at 5 – 70 K, depending on the nature of the tag. Common messenger species include H_2, D_2, He, and N_2, as they typically have high enough vapor pressures to be present in sufficient quantities at such low trap temperatures. While temperature and choice of messenger species are the primary controllables considered when tagging ions, the generation of tagged complexes is additionally influenced by their interaction time and the trapping parameters.

d. Mass Spectrometry

d.1. Time-of-Flight Mass Spectrometry

The core principle of time-of-flight mass spectrometry (TOFMS) is that the time it takes an ion to move from an acceleration region to an ion detector is directly related to its m/z ratio. This can be derived directly from the formula for kinetic energy (KE):

$$KE = V_a \cdot Q = \frac{1}{2}mv^2 \tag{8}$$

where V_a is the acceleration voltage, Q is the ion charge, m is the mass of the ion and v is its velocity. Rearrangement yields an expression for time as a function of distance traveled (d), m/z ratio, and the electric potential through which the ion is passing (V):

$$t = d\sqrt{\frac{m}{z} \cdot \frac{1}{2V_a}} \tag{9}$$

In TOFMS, d equates to the length of the flight tube, and V_a is typically a very large voltage – such that any kinetic energy conferred to the ions from previous ion optics is negligible in comparison. Both of these parameters are fixed, allowing t to vary proportionally to the square of the m/z ratio. This leads to the fundamental relation for TOFMS:

$$\frac{m}{z} \propto c(t^2) \tag{10}$$

in which c is a proportionality constant based on experimental parameters. With this knowledge, the arrival time of an ion at the detector can be used to extract the ion's m/z ratio. In most applications, a calibrant of known m/z is used to either measure c or provide a benchmark arrival time that can be used to determine an unknown target's m/z with a simple ratio.

d.2. Pulsed Mass Gate

There are two devices within this experimental apparatus whose main purpose is to separate ions by their m/z ratio: the pulsed mass gate and the reflectron. These devices serve as mass selection and mass separation steps directly before and after dissociation of the ion-tag complex, respectively.

The first of these tools – the pulsed mass gate – filters out unwanted ions to ensure spectroscopic observation of a well-defined target species, without possible background signals from other ions that may be caused by larger species breaking apart into fragments of the same *m/z* as the laser-induced fragment being observed.

The mass gate consists of a stack of parallel shims (technical details here) that, for most of the operational cycle of the experiment, are held at a potential of ± 400 V, with opposite polarities on alternating shims. This creates an electric field which deflects all incident ions from trajectories leading to detection. Once per cycle, when the desired ions reach the mass gate, the plates are pulsed to ground potential for ca. 500-2000 ns to allow the target ions passage through to the flight tube. The gate filters the ejected contents of the ion trap by only accepting ions within a certain range of *m/z* values, since only those species will arrive at the mass gate during the period in which it is held at ground.

d.3. Reflectron

The second mass selector is the reflectron, which has two repulsive electric field regions and approximately doubles the flight distance – leading to improved mass resolution and separation of the undissociated ion-tag complex and fragments (the original ion and the tag) after irradiation. The reflectron serves as an ion mirror, and the depth to which an ion penetrates the reflectron's electric field depends on its kinetic energy. The further an ion travels into the field before turning around, the longer its path length, making higher energy ions travel a longer distance than lower-energy ions. In this way, the reflectron narrows the arrival time distribution of ions with the same *m/z* that entered the flight tube with different kinetic energies. Additionally, the reflectron essentially doubles the flight path of the ions, improving mass resolution to within a fraction of an amu.

e. Spectroscopic Analysis

e.1. Action Spectroscopy

Traditional absorption spectroscopy is performed by monitoring the intensity of light before and after it passes through a sample to measure the number of photons absorbed as a function of wavelength. While commonly employed in solution-phase experiments with molecular densities in excess of 10^8 cm^{-3}, this approach is not feasible for the low ion amounts – both in terms of total number of ions (ca. 10^3 – 10^5) and number density (ca. 10^5 – 10^7 cm^{-3}) – typically present in mass-selective experiments [6]. The attenuation of light by such a small number of absorbers would be imperceptible. Instead, spectroscopic information is obtained through action spectroscopy: the detection of a photon-induced event as a function of photon energy. One simplified way to consider these approaches is that traditional absorbance spectroscopy measures the effect of a sample on light, while action spectroscopy measures the effect of light on a sample.

In this work we employ photodissociation spectroscopy, in which ion complexes are irradiated with a tunable light source and, upon absorption of a photon, undergo unimolecular decay into fragment ions with different *m/z* ratios. Fragment formation is measured as a function of wavelength to obtain a spectrum. Infrared spectroscopy presents a challenge in that a single photon is not energetic enough to break a covalent chemical bond, which prevents molecular fragmentation from being a viable dissociation pathway to monitor. To collect vibrational spectra, we attach weakly bound messenger molecules (typically N_2, though He, D_2, and Ar may also be used) to ionic species of interest. When an ion-tag complex absorbs a photon of sufficient energy, the absorbed energy is vibrationally redistributed throughout the complex, leading to the loss of the messenger molecule from the complex. This method is also referred to as vibrational predissociation spectroscopy.

The messenger tagging and dissociation processes for a cationic species (M^+) with an N_2 tag are described by eq. 11:

$$M^+ + N_2 \rightarrow [M \cdot N_2]^+ \xrightarrow{+h\nu} [M \cdot N_2]^{+*} \rightarrow M^+ + N_2 \qquad (11)$$

In the first step, species M^+ is tagged with a neutral N_2 molecule to form $[M{\cdot}N_2]^+$. This complex is mass-selected by the pulsed mass gate and irradiated with infrared light. In the second step, a photon is absorbed, and a hot complex – $[M{\cdot}N_2]^{+*}$ – is formed. In the final step, the absorbed energy in the hot complex is vibrationally redistributed, and the complex dissociates. The species ultimately being measured as a function of photon wavelength is M^+ after the predissociation process takes place. It is important to note that it is also possible to attach more than one tag to a complex. Photon absorption can then lead to the loss of several messenger tags, depending on the photon energy, complex temperature, and tag binding energy.

e.2. Light Source

The light source used for the experiments discussed herein is an infrared optical parametric converter (OPC) system (LaserVision) consisting of an optical parametric oscillator (OPO) and optical parametric amplifier (OPA) and pumped by a Nd:YAG laser. This setup produces 900 to 4000 cm^{-1} light (linewidth ca. 2 cm^{-1}, 5 ns pulse, ca. 1 – 15 mJ/pulse depending on wavelength). The setup is as follows:

The system is pumped by 1064 nm light produced by a Nd:YAG laser (Innolas Spitlight 600, 5ns pulse, 500 mJ/pulse) run at 10 Hz repetition rate, although lower repetition rates can be achieved by operating the Q-switch of the pump laser at integer fractions of the flashlamp repetition rate (10 Hz). The 1064 nm beam is first split into two beams with 66% and 33% of the incident power. The low power beam is passed through a half-wave plate ($\lambda/2$) and then frequency doubled in a potassium titanyl phosphate (KTP) crystal to 532 nm, before it is directed by dichroic mirrors into the OPO stage, which consists of two KTP crystals in a broadband resonator. The OPO generates a signal and an idler wave (λ_{signal} = 710 – 880 nm, near IR; λ_{idler} = 1345 – 2122 nm, intermediate IR), the combined energy and momentum of which conserve the 532 nm pump photon energy and momentum. The output of the OPO enters a dove prism and undergoes one total internal reflection that rotates the beam shape by 90° followed by a half-wave plate where the beam undergoes a 90° polarization rotation. It then passes through a Si filter to remove residual pump and signal photons before entering the OPA stage simultaneously with the aforementioned 66% of the 1064 nm pump beam, which at this point has been passed through a half waveplate and thin film horizontal polarization filter. The OPA consists of two pairs of potassium titanyl arsenate (KTA) crystals. The idler radiation from the OPO is amplified in these crystals, and the 1064 nm pump light are difference-frequency mixed by the OPA to generate mid IR radiation (ν_{mid} = 2100 – 4000 cm^{-1}). Residual 1064 pump photons are removed from the beam using a dichroic beam splitter. At this point, the laser setup depends on the experiment being performed. For mid IR spectroscopy, the idler is discarded by a Brewster stack-of-plates Si polarizer, leaving only the mid IR signal. For far IR spectroscopy, both the signal and idler are overlapped and routed into a silver gallium selenide ($AgGaSe_2$) crystal. By difference frequency mixing, the crystal produces a far IR beam (ν_{far} = 900 – 2150 cm^{-1}), and a Ge filter removes residual mid IR and idler light from the beam. A potassium bromide (KBr) window in the beamline reflects a small fraction (on the order of a few percent) of the beam into a pyroelectric joulemeter to monitor the pulse energy. The beamline is almost entirely enclosed – beginning shortly before the first 1064 nm beam splitter and connecting to the KBr window into the flight tube of the mass spectrometer. The enclosure is continuously purged with dry nitrogen to remove ambient water and CO_2, which are strong IR absorbers that can significantly attenuate the IR beam.

e.3. Microchannel Plate Detector

Detection of ions is performed using a microchannel plate (MCP) detector positioned opposite the reflectron. The detector consists of two 40 mm diameter microchannel plates assembled one behind the other in a chevron configuration (Jordan TOF Products, C-726, Dual Microchannel Plate Detector). MCP detectors are highly sensitive, capable of single particle detection. An ion impinging on the detector causes a cascade of electrons to propagate through the channel in which it entered. The electrons exit the first plate and initiate the cascade in the next plate. This process amplifies the original signal by a factor of ca. 10^6, and an anode placed at the exit of the microchannels collects the electrons and reports signal intensity.

III. Data Handling

a. Acquisition

The experiments described in this dissertation were performed with the mass spectrometer operating at 20 Hz and the laser/OPC system at 10 Hz in order to perform shot-for-shot background subtraction. The signal reported by the MCP detector is routed to two oscilloscopes (Tektronix TDS 2022), each triggered at 10 Hz. The oscilloscopes are triggered on alternating pulses of the 20 Hz cycle of the mass spectrometer, with one of the scopes triggered simultaneously with the laser system and the other triggered with the laser off. These display fragment ion signal with and without laser irradiation, respectively, and the oscilloscope triggering in tandem with the laser pulse also measures the laser pulse energy measured by the pyroelectric joulemeter inside the beamline enclosure. The oscilloscope which displays the ion signal with laser interaction is referred to as the “signal oscilloscope” and the other the “background oscilloscope”. The background oscilloscope monitors noise which results primarily from collision-induced dissociation. The signals on both oscilloscopes are averaged over 16 shots per data point to improve the signal-to-noise ratio. The settings of the oscilloscopes are such that only a 25 ns window of time is displayed, centered on the fragment ion peak. This window is narrow enough to exclude the baseline on either side of the peak being monitored, effectively operating the oscilloscopes as boxcar averagers. A custom LabVIEW program is used to read in data from both oscilloscopes, as well as direct the OPC system to scan through the desired wavelength range. At the beginning of each scan, the program records the signal, background, and laser power ("baseline values") with the laser shuttered. During the measurement of a spectrum, the program collects the signal, background, and the laser power as a function of the wavelength of the OPC output.

b. Processing

Multiple spectra are collected over the course of at least two days to improve the signal-to-noise ratio and ensure reproducibility. Signal data gathered by the LabVIEW program is corrected with the baseline values recorded before each scan, the shot-for-shot background, and photon fluence to obtain the ion yield Y according to eq. 12:

$$Y = [(S - S_0) - (B - B_0)] \cdot \frac{\nu}{(P - P_0)} \tag{12}$$

For each data point collected during a scan, S and B are the ion intensity from the signal and background oscilloscopes, S_0 and B_0 are their baseline values, ν is the wavenumber, P is the laser pulse energy measured by the joulemeter within the beam enclosure, and P_0 is the joulemeter's baseline value. This procedure first corrects the signal, background, and laser pulse energy readings for their baseline values. Then, the background ion signal is, in theory yielding fragment intensity solely due to laser-induced dissociation. The second part of the product in eq. 12 is proportional to the number of photons per laser pulse, and the laser-induced dissociation signal is divided by this number to correct for the photon fluence.

IV. References

(1) Xu, S.; Gozem, S.; Krylov, A. I.; Christopher, C. R.; Mathias Weber, J., Ligand influence on the electronic spectra of monocationic copper–bipyridine complexes. *PCCP* **2015**, *17* (47), 31938-31946.

(2) Wiley, W. C.; McLaren, I. H., Time-of-Flight Mass Spectrometer with Improved Resolution. *Review of Scientific Instruments* **1955**, *26* (12), 1150-1157.

(3) Fenn, J. B.; Mann, M.; Meng, C. K.; Wong, S. F.; Whitehouse, C. M., Electrospray ionization for mass spectrometry of large biomolecules. *Science* **1989**, *246* (4926), 64.

(4) Griffiths, J. A Brief History of Mass Spectrometry. *Anal. Chem.* **2008**, 80, 15, 5678–5683

(5) Earnshaw, S., On the Nature of the Molecular Forces which Regulate the Constitution of the Luminiferous Ether. *Trans. Cambridge Philos. Soc.* **1847**, *7*, 97

(6) Garand, E., Spectroscopy of Reactive Complexes and Solvated Clusters: A Bottom-Up Approach Using Cryogenic Ion Traps. *J. Phys. Chem. A* **2018**, *122*, 32, 6479–6490

(7) Weber, J. M.; Robertson, W. H.; Johnson, M. A., Argon predissociation and electron autodetachment spectroscopy of size-selected CH3NO2−·Arn clusters. *The Journal of Chemical Physics* **2001**, *115* (23), 10718-10723.

(8) Xu, S.; Smith, J. E. T.; Weber, J. M., The electronic spectrum of cryogenic ruthenium-tris-bipyridine dications in vacuo. *The Journal of Chemical Physics* **2016**, *145* (2), 024304.

3. Bipyridine

This chapter has been reproduced in part from the following previously published article:

Madison M. Foreman, Rebecca J. Hirsch, and J. Mathias Weber, “Effects of Formate Binding to a Bipyridine-Based Cobalt-4N Complex” *The Journal of Physical Chemistry A* **2021** *125* (33), 7297-7302
DOI: 10.1021/acs.jpca.1c06037

I. Introduction

Catalytic reduction of carbon dioxide (CO_2) is at once an immensely valuable and deeply challenging chemistry. CO_2 reduction catalysis provides a viable avenue for counteracting excess amounts of atmospheric CO_2 while also having applications in the production of fuels either by traditional electrocatalysis or catalysis driven by solar energy. [1,2] Research in the field of catalytic CO_2 reduction has been ongoing for several decades, and is an ever-growing area of study. [3–6] Presently available catalysts for the reduction of CO_2 do not yet meet the required efficiency, selectivity, and stability for use on an industrial scale. In order to design catalysts suitable for industrial use, a detailed molecular understanding of the mechanisms of CO_2 reduction is needed.

In many organometallic catalysts, transition metal centers are surrounded by organic ligands that coordinate to the metal center through four nitrogen atoms (M-4N complexes). [7–11] Of these systems, those with bipyridine-based ligands are often highly effective, and are able to rapidly convert CO_2 into carbon monoxide (CO). [12–15] The choice of organic ligand is crucial in optimizing the performance of a catalytic molecule, as demonstrated by Smieja et al. in 2010. [4] They began with one of the most widely known members of the bipyridine catalyst family: Lehn's [Re·(bpy)·$(CO)_3$·Cl] (bpy = 2,2′-bipyridine) catalyst. [16] They modified the catalyst’s ligand framework by placing *tert*-butyl groups at the 4,4′-positions of the bpy ligand, forming [Re·(bpy-*t*Bu)·$(CO)_3$·Cl] (bpy-*t*Bu = 4,4′-di-*tert*-butyl-2,2′-bipyridine) — this change garnered an order-of-magnitude improvement in both the turnover frequency and turnover number by stabilizing a radical Re(0) intermediate and reducing dimer formation that impedes catalysis.

Organic ligands exert control over the functionality of a catalyst by electrostatically and sterically governing access to the metal center (by solvent or substrate molecules) and acting as charge reservoirs that modulate the redox properties of the metal center. Over the course of a catalytic cycle, the ligand framework shifts both structurally and electronically to accommodate substrate docking, reaction intermediates, and product formation. These changes in geometry and charge distribution are vital to understand in the endeavor to create better catalysts, but are difficult to study in the condensed phase. Under turnover conditions, interactions with an ever-evolving chemical environment and high degree of speciation complicate the characterization of molecular-level details.

By collecting infrared spectra of cold gaseous ions which are mass-selected, many solution-induced challenges can be circumvented. Vibrational spectra indirectly encode the very information we are interested in — structure and charge distribution — and can provide detailed knowledge about complex molecular systems.

The work described herein investigates $[Co\cdot(bpy\text{-}t\mathrm{Bu})_2]^{2+}$ and complexes of the form $[M\cdot(bpy\text{-}t\mathrm{Bu})_2\cdot HCOO]^+$ where M is either Co, Ni, or Cu. The metal center is coordinated to two bpy-*t*Bu ligands and has the ability to bind a formate ($HCOO^-$) ligand, one of several possible CO_2 reduction products (shown in Scheme 3.1).[17–19] We use infrared photodissociation spectroscopy enabled by N_2 messenger tagging to investigate changes in the properties of the catalyst species upon i) formate complexation, and ii) variation of the metal center. We compare our experimental results with predicted infrared spectra based on density functional theory (DFT) calculations.

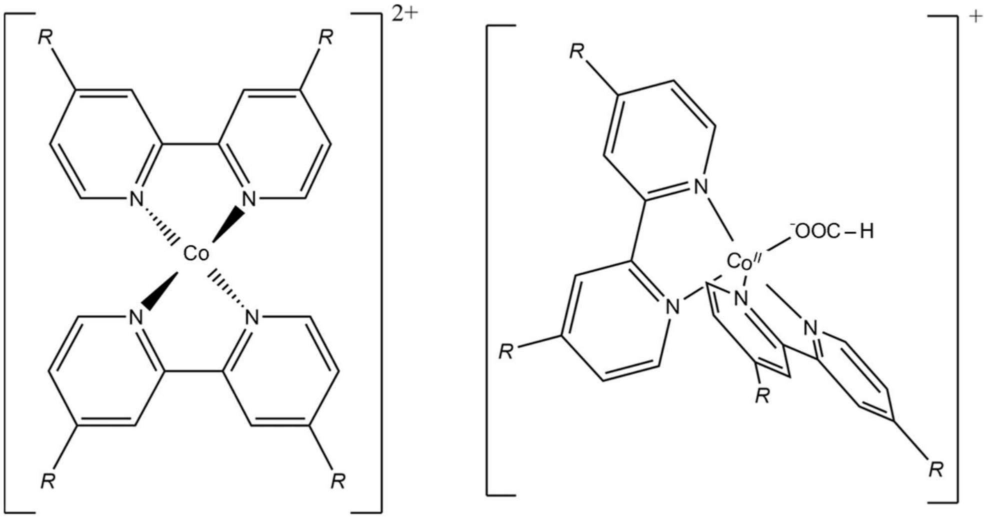

Scheme 3.1. Line structures of $[Co{\cdot}(bpy\text{-}tBu)_2]^{2+}$ **(left)** and $[Co{\cdot}(bpy\text{-}tBu)_2{\cdot}HCOO^{-}]^{+}$ **(right)**, with R = *tert*-Butyl.

II. Methods

a. Experimental

Solutions of $[M{\cdot}(bpy\text{-}tBu)_2]^{2+}$ (M = Co, Ni, Cu) were prepared by dissolving ca. 5–10 μmol of $Co(NO_3)_2{\cdot}6H_2O$, $Ni(NO_3)_2{\cdot}6H_2O$, or $Cu(NO_3)_2{\cdot}(H_2O)_3$ and ca. 10–20 μmol of bpy-*t*Bu (Sigma-Aldrich, 98%) in 5.75 mL of methanol (Macron, ≥99.8%). Adding formate to these solutions at ca. 100-fold excess resulted in preparation of $[M{\cdot}(bpy\text{-}tBu)_2{\cdot}HCOO]^{+}$ complexes. Formate was produced by titrating formic acid (Sigma-Aldrich, ≥95%) with aqueous KOH (Fisher-Scientific) until a pH of 8– 9 was achieved to ensure the formic acid was completely converted to formate anions. All chemicals were used as purchased, and all solutions were sprayed without further purification.

The experimental setup is described in Chapter 2.

b. Computational

Geometry optimizations and vibrational spectra of all complexes under study were performed by using spin-unrestricted DFT (B3LYP functional [20], LANL2DZ [21] basis sets for all atoms). These calculations were rather costly, owing to the size of the molecules under study. On average, 40-100 CPU hours were required to complete the combined optimization and frequency calculations. They were also challenging, due to the electronic structure of the transition metals, and required extensive testing of methodologies to find a suitable approach. Other attempted strategies included standard B3LYP, restricted open shell (RO)B3LYP, and ωB97XD, as well as other basis sets (cc-pVDZ, def2-SVP, def2-TZVP). Each of these methods failed for some number of the metals due to spin contamination, particularly in high spin states, despite multiple attempts.

The harmonic frequencies from these calculations were scaled by 0.975 to provide the best match to the experimental spectrum of $[Co\cdot(bpy\text{-}t\mathrm{Bu})_2]^{2+}$, since the ligand vibrations proved to be least sensitive to the identity of the metal for all complexes. All calculations were performed using Gaussian 16. [22]

III. Results and Discussion

a. Addition of a Formate Ligand

The bare cobalt complex, $[Co\cdot(bpy\text{-}t\mathrm{Bu})_2]^{2+}$, has two possible spin states: a quartet and a doublet. These complexes take on a geometry between tetrahedral and octahedral, and the calculated structures are nearly identical. Figure 3.1 shows the experimental spectrum of $[Co\cdot(bpy\text{-}t\mathrm{Bu})_2]^{2+}$ in the fingerprint region compared to the predicted infrared spectra for each spin state.

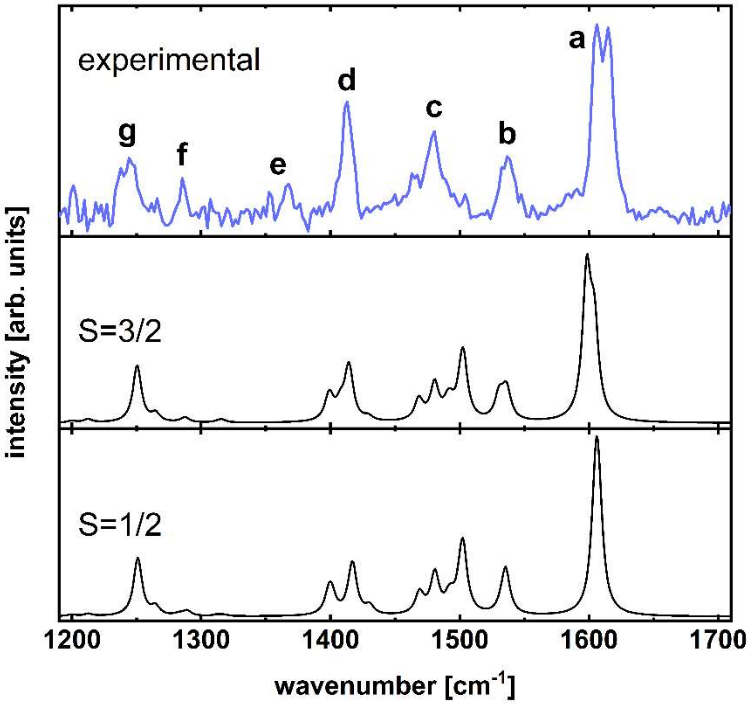

Figure 3.1. Comparison of the experimental spectrum (top trace, light blue) and calculated spectra (lower traces, black) of the doublet and quartet spin states of [Co·(bpy-tBu)2]2+ tagged with one N2 molecule. See Appendix A for discussion of N_2 tagging position. The calculated data are labeled with their spin states.

Table 3.1. Calculated energies and spin states of [Co·(bpy-*t*Bu)$_2$]$^{2+}$ and different isomers of [Co·(bpy-*t*Bu)$_2$·HCOO]$^+$ complexes, as well as Co-O distances for the latter.

Complex	Spin	Relative Energy [meV]	Co-O [pm]
[Co·(bpy-*t*Bu)$_2$]$^{2+}$	3/2	111	
	1/2	0	
[Co·(bpy-*t*Bu)$_2$·HCOO]$^+$			
Isomer Co-QA	3/2	0	221
Isomer Co-QB		224	197, 336
Isomer Co-DA	1/2	163	200, 253
Isomer Co-DB		281	192, 335
Isomer Co-DC		380	192, 336

The most prominent features in the experimental spectrum can be assigned by comparison with the calculated spectrum. Peaks with energies greater than 1560 cm^{-1} are associated primarily with bipyridine modes, while lower energy features also involve t-Bu vibrations. Peak **a**, the highest energy and most intense feature, is a doublet with peaks at 1606 and 1615 cm^{-1}. The modes giving rise to this feature combine C–C stretching and in-ring-plane CH wagging motions, with the bipyridine rings of each ligand vibrating in-phase in the lower energy peak and out of phase in the higher energy peak. The two components can be assigned to modes in the bipyridine rings of the ligands that combine C–C stretching and in-ring-plane CH wagging motions, where the motions of each bipyridine ring are coupled in phase in the lower frequency peak and out of phase in the higher frequency peak (patterns of motion illustrated in Figure 3.2).

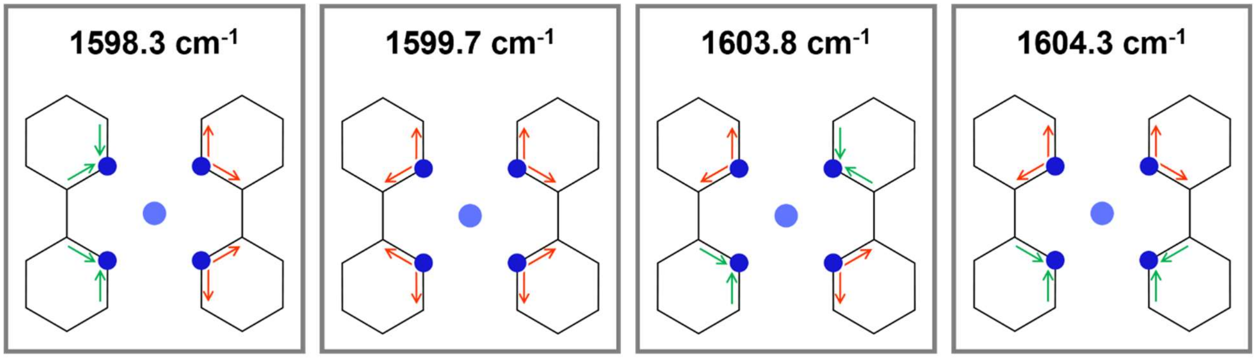

Figure 3.2. Simplified representation of vibrational patterns corresponding to the highest frequency spectral feature of [Co·(bpy-tBu)$_2$]$^{2+}$. Calculated frequencies scaled by 0.975 shown above each corresponding pattern of motion.

Feature **b**, at 1537 cm^{-1}, consists of antisymmetric C–N–C stretching (and accompanying C–C stretching and C–H wagging) modes, again localized on the bipyridine rings, with similar phase relations as those in the highest frequency peak pair. The broad envelope of **c** (maximum intensity at 1480 cm^{-1}) includes several unresolved transitions, with the most intense belonging to H–C–H bending modes on the t-Bu groups. Feature **d** (1413 cm^{-1}) appears experimentally as a strong peak with a low-energy shoulder. The main contributor of intensity in this feature is a group of bipyridine ring deformation modes that also involve CH_3 umbrella motions on the tert-butyl groups, and the left shoulder is the combined signature of several modes with C–H wagging on the rings and t-Bu methyl group umbrella motions. The weak doublet with peaks at 1353 cm^{-1} and 1367 cm^{-1} is labeled **e**, and neither peak is reproduced by either of the calculated spectra. Peak **f** at 1285 cm^{-1} is similarly low in intensity, but the calculated spectrum does predict a mode at this energy comprised largely of antisymmetric C–N–C and C–C stretching localized to the ring modes, with low-amplitude wagging motion throughout the rest of the ligands. Finally, peak **g** (1244 cm^{-1}) is attributed to a mode consisting of coupled C–C stretches throughout the complex.

The calculated structure of the high-spin quartet [Co·(bpy-*t*Bu)$_2$]$^{2+}$ complex is shown in Figure 3.3.

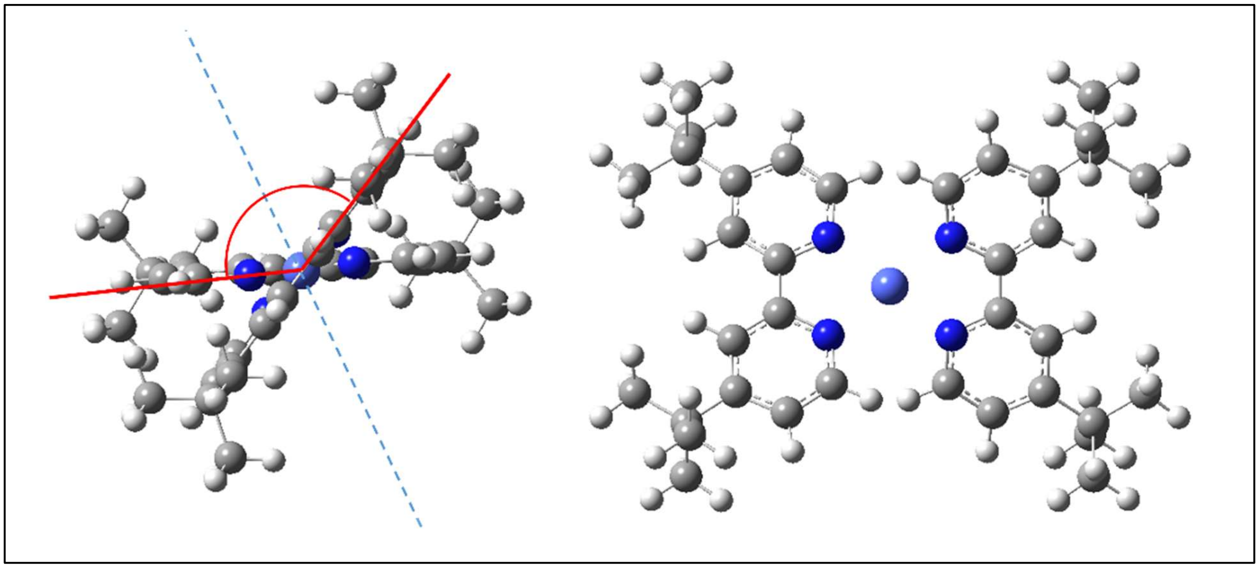

Figure 3.3. Calculated structure of [Co·(bpy-tBu)$_2$]$^{2+}$. **Left:** side view, with the C_2 symmetry axis of the complex shown as a dashed line and the N-Co-N angle between the bpy-*t*Bu planes indicated in red. **Right:** view along the symmetry axis. Color scheme: H = white; C = grey; N = dark blue, Co = light blue.

The complex has approximately *C_2* symmetry, and the coordination geometry of the ligands lies between square planar and tetrahedral. The bpy-*t*Bu ligands are very slightly buckled, and the N–Co–N angle between the ligands is 152°. The metal center is equidistant from each of the coordinating N atoms, with a Co–N distance of 206 pm. Upon addition of formate to form $[\mathrm{Co}\cdot(\mathrm{bpy}\text{-}t\mathrm{Bu})_2\cdot\mathrm{HCOO}]^+$, both spectral and structural changes appear. The vibrational spectra for $[\mathrm{Co}\cdot(\mathrm{bpy}\text{-}t\mathrm{Bu})_2]^{2+}$ and $[\mathrm{Co}\cdot(\mathrm{bpy}\text{-}t\mathrm{Bu})_2\cdot\mathrm{HCOO}]^+$ are shown in Figure 3.4 alongside calculated spectra for isomers of the formate-containing complex.

The modes of the bpy-*t*Bu ligands exhibit small red shifts (<25 cm^{-1}) upon formate complexation, and new features appear in the experimental spectrum which belong to the symmetric and antisymmetric O–C–O stretching modes (ν_s and ν_{as}, respectively). Both formate modes appear close to bpy-*t*Bu signatures, and identification of each formate peak is not immediately obvious. However, given the overall red shift observed in the bpy-*t*Bu modes, we expect that the bpy-*t*Bu features (**b** and **e** in Figure 3.1) which overlap with the new formate features will behave similarly.

Beginning with the formate O–C–O antisymmetric stretch, the high-energy doublet observed in the spectrum of $[\mathrm{Co}\cdot(\mathrm{bpy}\text{-}t\mathrm{Bu})_2\cdot\mathrm{HCOO}]^+$ shows peaks at 1533 cm^{-1} and 1544 cm^{-1}. Since only the low-energy peak is red of the original bpy-*t*Bu mode, **b**, we assign that feature as such and ascribe the high-energy peak to ν_{as} (the free formate stretches appear at ν_s = 1314 cm^{-1} and ν_{as} = 1622 cm^{-1}). [23]

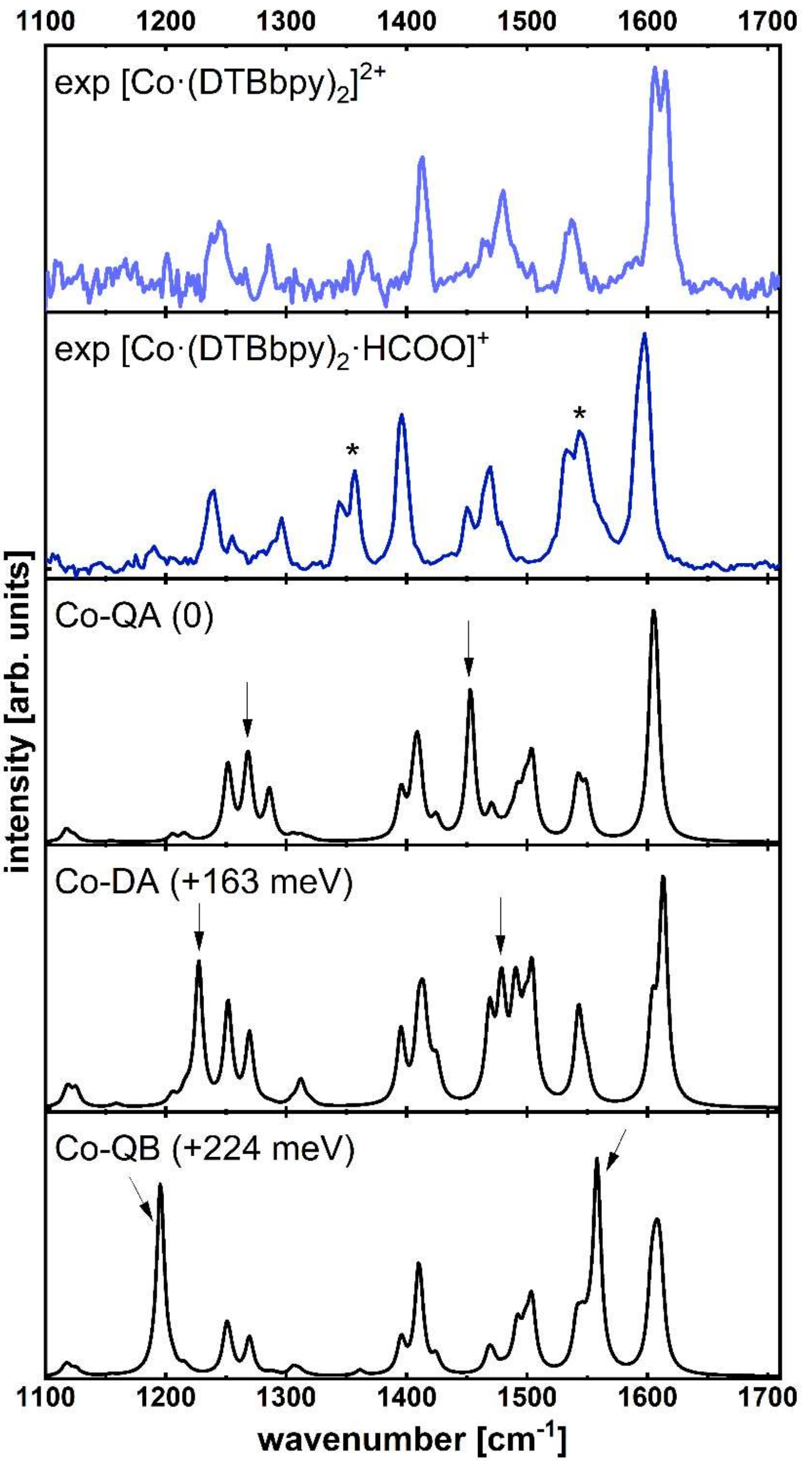

Figure 3.4. Comparison of the experimental spectra of $[Co\cdot(bpy\text{-}tBu)_2]^{2+}$ (top, light blue) and $[Co\cdot(bpy\text{-}tBu)_2\cdot HCOO]^+$ (second from top, dark blue) with calculated spectra for the isomers of $[Co\cdot(bpy\text{-}tBu)_2\cdot HCOO]^+$ (bottom traces, black, isomer labels and relative energies given as in Table 3.1). The signatures of the formate OCO stretching vibrations in the experimental spectrum are marked with asterisks, while their positions in the calculated spectra are marked with arrows, with ν_s being the lower frequency feature.

In the region of ν_s, there exists a doublet in both spectra, though it is not very intense for the bare complex. Additionally, both peaks in the [Co·(bpy-*t*Bu)$_2$·HCOO]$^+$ spectrum are lower in energy than those in the spectrum of [Co·(bpy-*t*Bu)$_2$]$^{2+}$ (**e** in Figure 3.1), preventing assignment based on frequency alone. Looking at the relative intensities, it is apparent that the left half of the doublet in the formate-containing complex is comparable to the intensity of the **e** peaks in the bare complex, while the right half of the [Co·(bpy-*t*Bu)$_2$·HCOO]$^+$ doublet is substantially stronger. Since none of the other bpy-*t*Bu peaks exhibit meaningful changes in relative intensity, we assign the peak at 1344 cm^{-1} as the bpy-*t*Bu feature and the 1357 cm^{-1} peak as ν_s.

It is of note that, in all calculated isomers, the normal modes associated with ν_s and ν_{as} are not purely characterized by the symmetric and antisymmetric stretching motions — ν_s and ν_{as} are strongly coupled to the O–C–O bend and C–H wag in the formate plane, respectively. This coupling, in addition to the changes in geometry, charge density, and charge distribution of the formate moiety result in the observed blue shift of ν_s and red shift of ν_{as}, reducing the splitting between the two modes.

DFT calculations produced five minimum energy structures, two with a quartet spin state and three with a doublet spin state. The lowest energy isomer of the formate complex (Co-QA) is in a quartet state (Table 3.1) and is the only calculated isomer in which the formate binds to the Co atom in a symmetric and bidentate position, as shown in Figure 3.5.

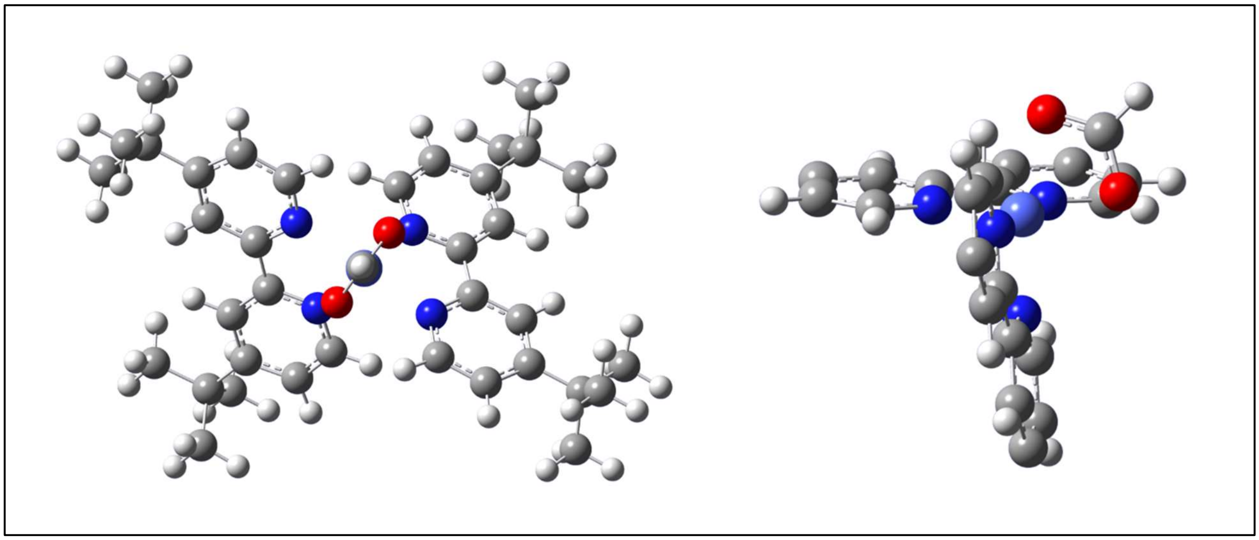

Figure 3.5. Lowest energy structure of [Co·(bpy-tBu)$_2$·HCOO]$^+$ (isomer Co-QA). **Left:** Structure viewed along the CH bond axis of the formate ligand to highlight the orientation of the formate relative to the metal atom. **Right:** Structure viewed from the side to highlight formate orientation relative to bpy-*t*Bu ligands. Color scheme: H = white, C = gray, N = dark blue, Co = light blue, O = red.

The other isomers all have an asymmetric formate binding motif with varying degrees of asymmetry and different orientations to the bpy-*t*Bu ligands (see Appendix A). The addition of the formate ligand forces the bpy-*t*Bu planes to adopt a more acute angle than in the bare complex. In the formate complex, the N–M–N angle shrinks to 97° for Co-QA and 95°–100° in the other calculated isomers. This geometry change is observed for all metals studied here, with approximately the same calculated N–M–N angles for [M·(bpy-*t*Bu)$_2$]$^{2+}$ and [M·(bpy-*t*Bu)$_2$·HCOO]$^+$ (M = Co, Ni, Cu). All of the calculated structures adopt a distorted octahedral coordination of the metal atom.

The calculated spectra reproduce the experimental pattern with varying degrees of success. On the whole, they match the bpy-*t*Bu features well, but do poorly for the formate O–C–O stretches. This trend carries to the spectra of Ni- and Cu-complexes as well. In such a case where the absolute positions of ν_s and ν_{as} are not recovered by the calculated spectra, we may look to the splitting between these peaks to identify the most likely isomer. The experimental

ν_s–ν_{as} splitting is 187 cm^{-1}, and the splitting in the Co-QA calculated spectrum is 185 cm^{-1}. All other isomers have a much larger splitting, less compatible with the experimental value.

The mismatch between the absolute frequencies of the formate modes between experiment and calculation can be attributed to an underprediction of the C–O bond strength. Using the IR spectrum of Ar-tagged formate as an experimental benchmark, the computational method employed here does a marginally better job recovering the O–C–O stretching frequencies (experimental: 1314 cm^{-1} and 1622 cm^{-1}, scaled harmonic frequencies: 1230 cm^{-1} and 1567 cm^{-1}), but still underestimates their absolute frequencies. [23] However, it is fairly successful in capturing their ν_s–ν_{as} splitting (experimental: 308 cm^{-1}, calculated: 337 cm^{-1}). The absolute frequencies of these stretches are sensitive to the partial charge on the carboxylate group, as changes in electron density will affect the C–O bond strengths. The ν_s–ν_{as} splitting, on the other hand, reports on the local symmetry of the C–O bonds and the O–C–O bond angle (see Chapter 5 for a discussion on this relationship).

The excellent match for the ν_s–ν_{as} splitting together with being the lowest energy isomer indicate that Co-QA is the most likely structure of $[\mathrm{Co}\cdot(\mathrm{bpy}\text{-}t\mathrm{Bu})_2\cdot\mathrm{HCOO}]^+$, and that the formate adopts a symmetric, bidentate metal binding motif.

b. Exchange of the Metal Center

The experimental spectra for all three formate complexes — $[\mathrm{M}\cdot(\mathrm{bpy}\text{-}t\mathrm{Bu})_2\cdot\mathrm{HCOO}]^+$ (M = Co, Ni, Cu) — are compared in Figure 3.6. The features representing the bpy-*t*Bu ligands are identical within the bandwidth of our light source, indicating that the geometries of these ligands are insensitive to exchange of the metal center. This is in agreement with the calculated structures for each complex, with the lowest energy isomers for each metal having approximately the same N-M-N angles (ca. 100°).

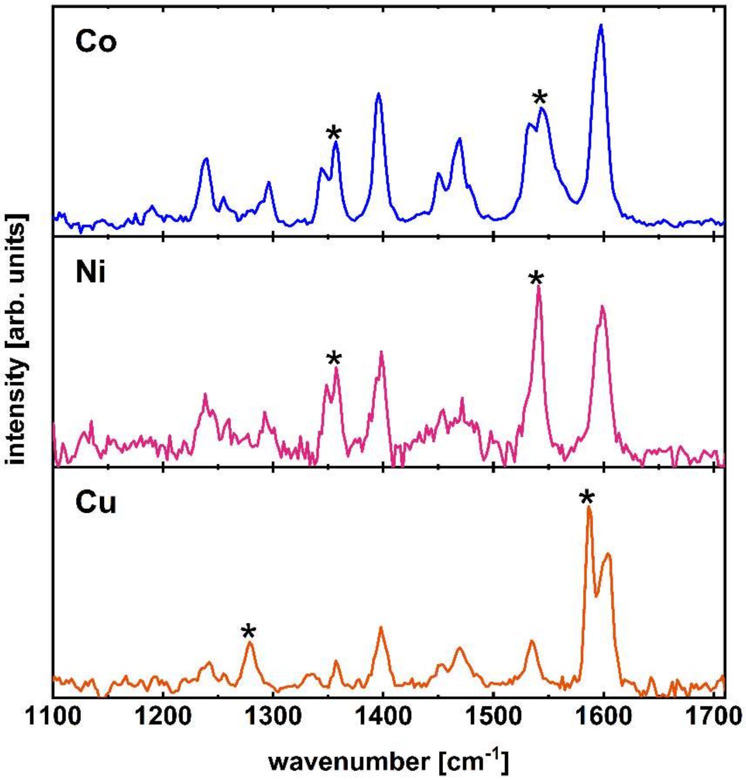

Figure 3.6. Comparison of the spectra of [M·(bpy-tBu)$_2$·HCOO]$^+$ (M = Co, Ni, Cu). Metal identity is given in each panel (Co = dark blue, Ni = pink, Cu = orange). The positions of ν_s and ν_{as} are identified in each case by asterisks.

Additionally, the formate stretching modes (assigned based on comparison with the spectra of [Co·(bpy-*t*Bu)$_2$·HCOO]$^{2+}$ and [Co·(bpy-*t*Bu)$_2$·HCOO]$^+$) are very similar in the Co and Ni complexes, which suggests that their formate binding orientations are also alike.

Figure 3.7 shows a comparison between the experimental spectrum of [Ni·(bpy-*t*Bu)$_2$·HCOO]$^+$ and the calculated spectra of the six minimum energy structures produced by DFT calculations (see Appendix A). Their relative energies and Ni-O distances are given in Table 3.2. As with Co, the Ni complex has two possible spin states — here a triplet and a singlet — and the high-spin state is lowest in energy. The calculated energy difference between low- and high-spin states is more pronounced for the Ni formate complexes than for Co, with calculations predicting a gap of ca. 1 eV for Ni. It is of note that calculations of the [Ni·(bpy-

*t*Bu)$_2$]$^{2+}$ catalyst without the formate are predicted to have a singlet ground state that is lower in energy by 355 meV than the corresponding triplet state. This suggests that formate complexation causes a change in spin state for the Ni complex.

The similarities between the Ni and Co complexes carry through to their calculated structures. The lowest energy isomer for [Ni·(bpy-*t*Bu)$_2$·HCOO]$^+$ (Ni-TA) is structurally similar to Co-QA, with the formate bound to the metal center in a symmetric, bidentate orientation (see Figure 3.8). The two complexes differ in the degree to which their calculated isomers vary across spin states. The singlet states of the Ni complex predict bpy-*t*Bu modes (C–C stretching and in-ring-plane C–H wagging motions on the bpy rings) much higher in energy than the highest frequencies observed experimentally. The triplet structures result in a superior spectral match to the bpy-*t*Bu modes, and there are stark differences in energy between the singlet and triplet states (ca. ≥350 meV). Based on these observations, it is clear that the spin state of the ground state of [Ni·(bpy-*t*Bu)$_2$·HCOO]$^+$ is a triplet.

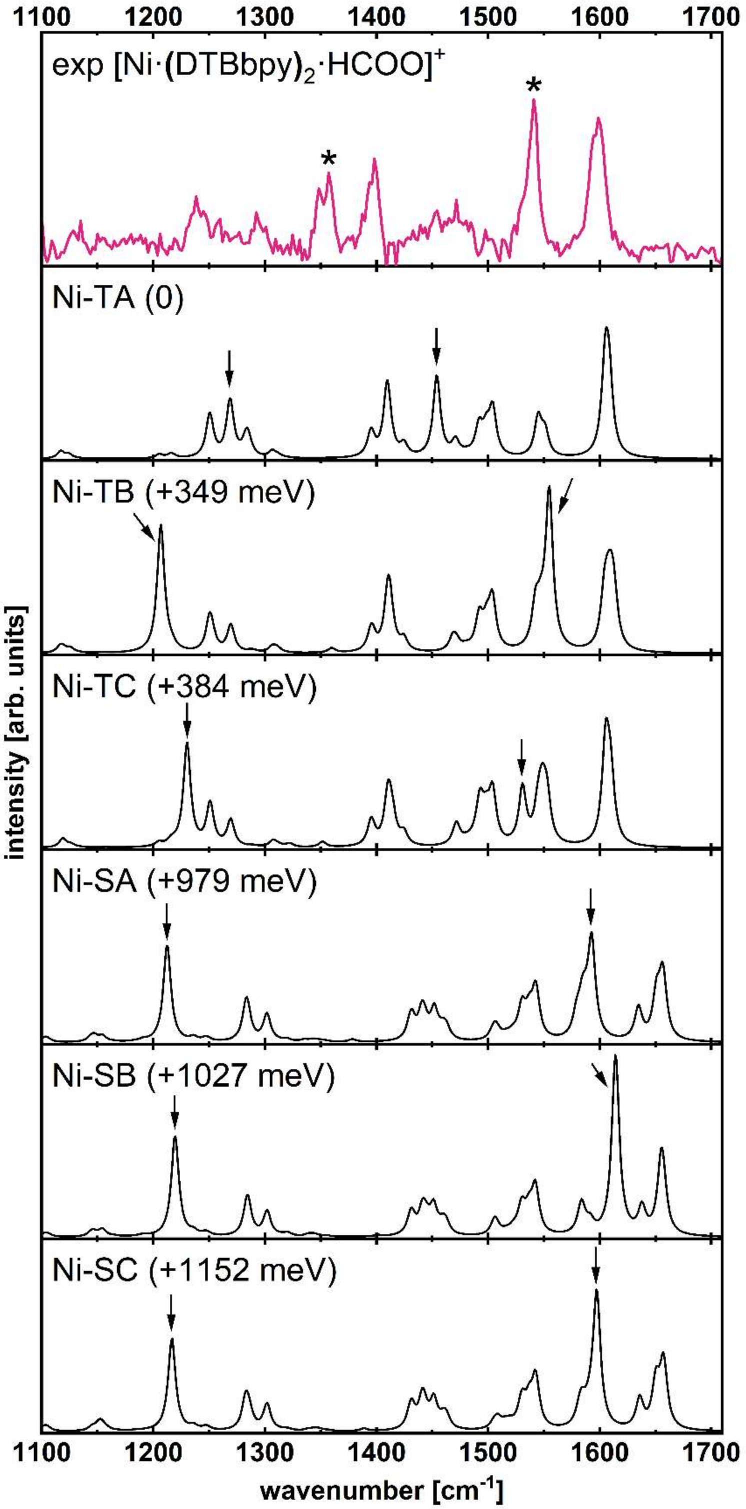

Figure 3.7. Comparison of the experimental spectra of [Ni·(bpy-*t*Bu)$_2$·HCOO]$^+$ (top, pink) with calculated spectra for the isomers of [Ni·(bpy-*t*Bu)$_2$·HCOO]$^+$ (bottom traces, black, isomer labels and relative energies given as in Table 3.2). The signatures of the formate OCO stretching vibrations in the experimental spectrum are marked with asterisks, while their positions in the calculated spectra are marked with arrows, with ν_s being the lower frequency feature.

Table 3.2. Calculated energies, spin states, and Ni-O distances for different isomers of [Ni·(bpy-*t*Bu)$_2$·HCOO]$^+$ complexes.

Complex	Spin	Relative Energy [meV]	Ni-O [pm]
Isomer Ni-TA	1	0	217
Isomer Ni-TB		349	197, 334
Isomer Ni-TC		348	197, 340
Isomer Ni-SA	0	979	190, 302
Isomer Ni-SB		1027	189, 335
Isomer Ni-SC		1152	189, 325

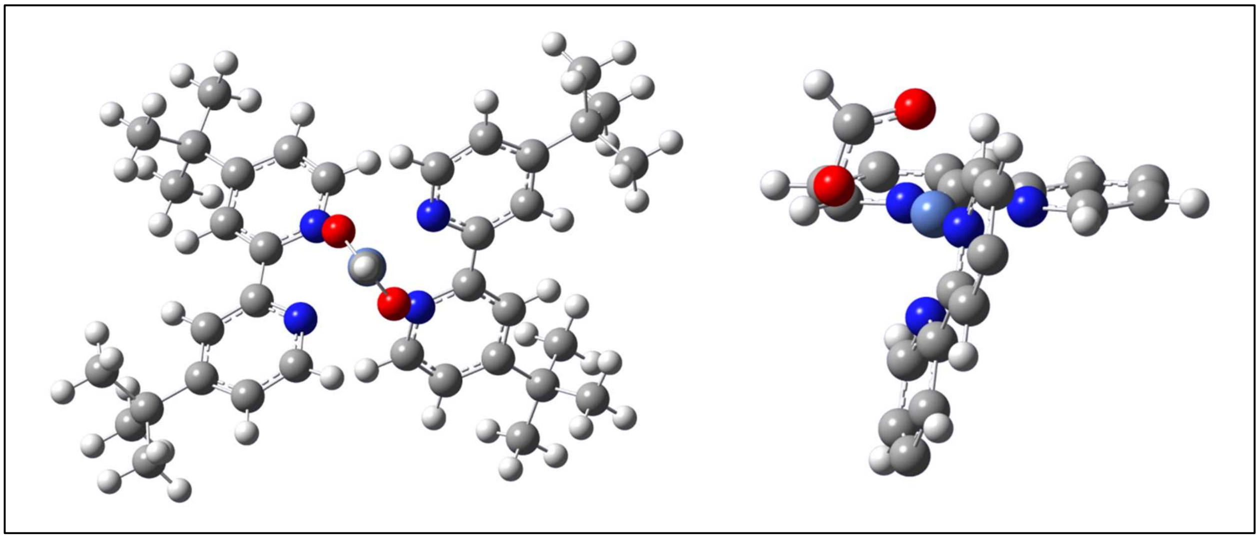

Figure 3.8. Lowest energy structure of [Ni·(bpy-tBu)$_2$·HCOO]$^+$ (isomer Ni-TA). **Left:** Structure viewed along the CH bond axis of the formate ligand to highlight the orientation of the formate relative to the metal atom. **Right:** Structure viewed from the side to highlight formate orientation relative to bpy-*t*Bu ligands. Color scheme: H = white, C = gray, N = dark blue, Ni = light blue, O = red.

As is the case with the Co complex, the computed isomers of the Ni complex fail to reproduce the absolute energies of the formate modes, but successfully recover the ν_s–ν_{as} splitting (184 cm^{-1}). Ni-TA achieves a quantitative match with a ν_s–ν_{as} splitting of 186 cm^{-1}.

While the other calculated structures do appear to recover the absolute energy of ν_{as} well, this may be serendipitous, as they miss the mark entirely for ν_s and have ν_s–ν_{as} splittings of greater than 300 cm^{-1}. Based on this analysis, we assign Ni-TA the most likely isomer of $[Ni\cdot(bpy\text{-}tBu)_2\cdot HCOO]^+$.

The structural assignment of $[Cu\cdot(bpy\text{-}tBu)_2\cdot HCOO]^+$ is simplified by the ground state only allowing one possible electron configuration: a doublet. The vibrational spectrum of $[Cu\cdot(bpy\text{-}tBu)_2\cdot HCOO]^+$ is presented in comparison with the simulated spectra of the three minimum-energy structures produced by DFT calculations (see Appendix A) in Figure 3.9. The energies and Cu-O distances of each isomer are reported in Table 3.3.

In line with the other two formate complexes, the lowest energy isomer (Cu-A) best captures the splitting between the formate O–C–O stretches yet does not accurately predict their absolute energies. The experimentally observed ν_s–ν_{as} splitting is 307 cm^{-1}, and the calculated splitting for Cu-A is 303 cm^{-1}. This makes Cu-A the best spectral match, as both other isomers have associated ν_s–ν_{as} splittings in excess of 370 cm^{-1}. In parallel with the other metals, we ascribe the experimental spectrum to the lowest energy isomer, Cu-A.

Notably, the splitting between formate modes in $[Cu\cdot(bpy\text{-}tBu)_2\cdot HCOO]^+$ is over 60% greater than in the analogous Co and Ni complexes. More differences emerge between Cu and the other metal centers when considering the structure of the lowest-energy isomer (shown in Figure 3.10). While the formate ligand is still bound in a bidentate manner, it is oriented asymmetrically to the metal center. This offset leads to a considerable difference between the Cu–O bond lengths — the disparity in Cu-A is 82 pm. The inequality between M-O bond lengths appears to increase in tandem with the ν_s–ν_{as} splitting, consistent with the idea that the splitting between O–C–O stretching modes reports on the symmetry between the two constituent C-O bonds.

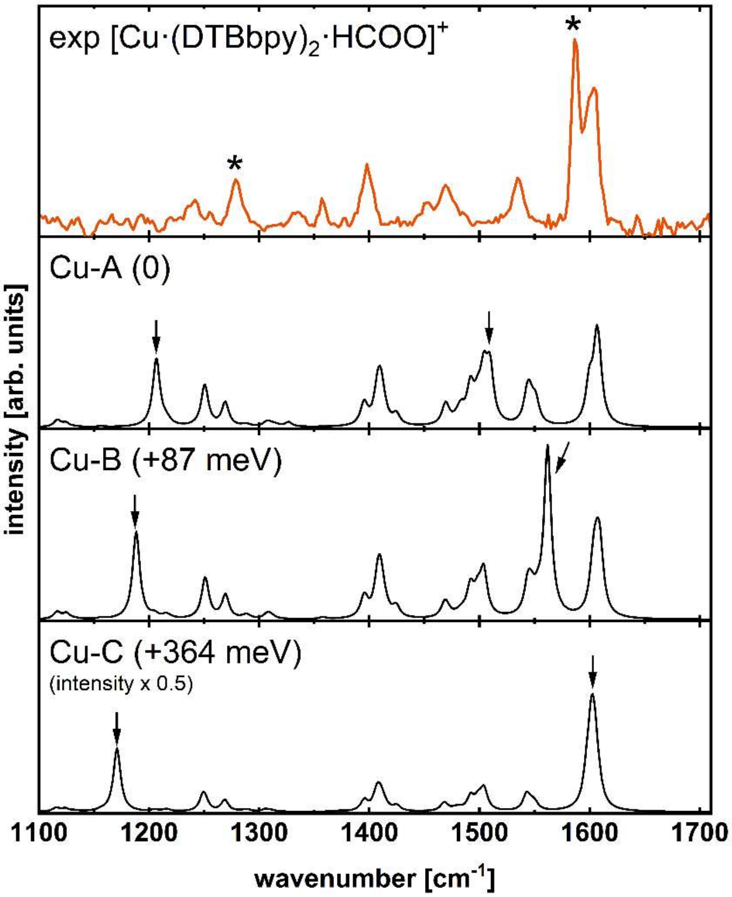

Figure 3.9. Comparison of the experimental spectra of $[Cu\cdot(bpy\text{-}tBu)_2\cdot HCOO]^+$ (top, orange) with calculated spectra for the isomers of $[Cu\cdot(bpy\text{-}tBu)_2\cdot HCOO]^+$ (bottom traces, black, isomer labels and relative energies given as in Table 3.3). The signatures of the formate OCO stretching vibrations in the experimental spectrum are marked with asterisks, while their positions in the calculated spectra are marked with arrows, with ν_s being the lower frequency feature.

Table 3.3. Calculated energies and spin states of different isomers of $[Cu\cdot(bpy\text{-}tBu)_2\cdot HCOO]^+$ complexes.

Complex	Relative Energy [meV]	Cu-O [pm]
Isomer Cu-A	0	201, 283
Isomer Cu-B	87	196, 334
Isomer Cu-C	364	194, 415

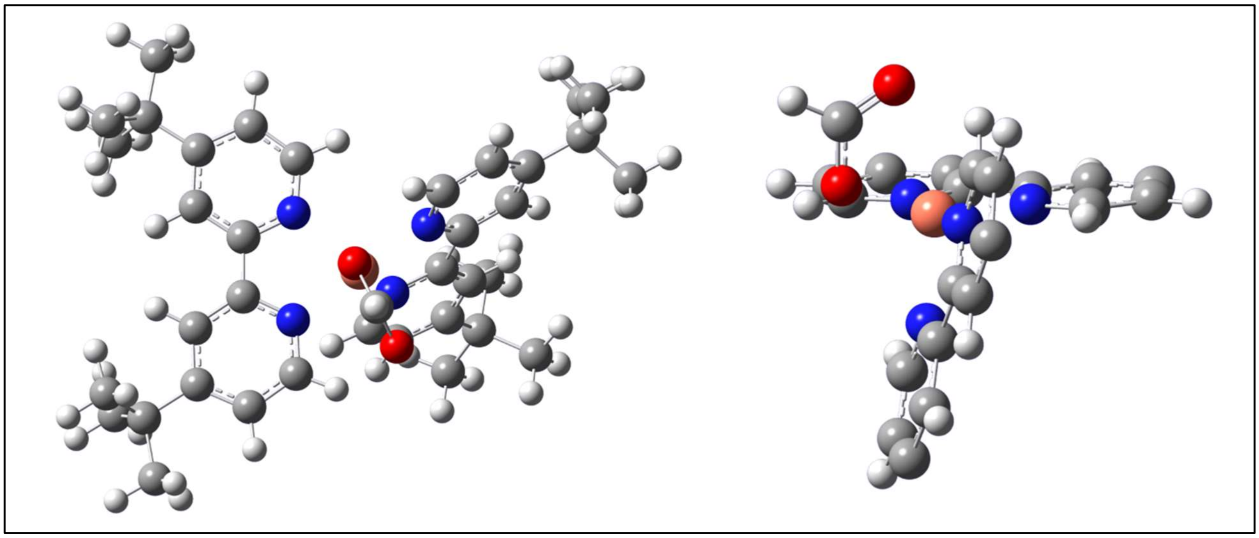

Figure 3.10. Lowest energy structure of $[Cu{\cdot}(bpy\text{-}tBu)_2{\cdot}HCOO]^+$ (isomer Cu-A). **Left:** Structure viewed along the CH bond axis of the formate ligand to highlight the orientation of the formate relative to the metal atom. **Right:** Structure viewed from the side to highlight formate orientation relative to bpy-*t*Bu ligands. Color scheme: H = white, C = gray, N = dark blue, Cu = orange, O = red.

Formal discussion of electron configurations is typically based on integer charges, but the fractional charges produced by natural population analysis still lend themselves to a qualitative discussion. The calculated charge distributions for each complex can be found in Table 3.4, and the spin density is primarily localized on the metal atoms. This is of interest in the context of catalysis, wherein the organic ligands are key in tuning the effective oxidation state of the metal. In each complex studied here, the bpy-*t*Bu ligands hold approximately half of the total positive charge within the complex. While no population analysis should be considered exact, this nonetheless highlights the ability of the ligand framework to accommodate a significant amount of charge transfer to the metal center and therefore act as charge reservoirs for the complex. Natural population analysis also depicts substantial charge transfer from the formate moiety to the catalyst structure, amounting to ca. -0.4 *e* in all complexes. Perhaps the most interesting aspect of the partial charge distributions is that all metal atoms have approximately half of their formal charge. Each complex was prepared with M(II) salts, which may lead to the natural assumption that the metal atoms would be formally characterized as M^{2+}. Yet, computational analysis predicts charges between +0.87 *e* and +1.1 *e* for them all. This further demonstrates the high degree of charge transfer throughout this complex as a result of the interplay between the initially positive metal, neutral bpy-*t*Bu ligands, and negative formate.

Table 3.4. Calculated charge distributions (in *e*) for each complex from natural population analysis.

Complex	Metal	bpy-*t*Bu Ligands	Formate
$[Co{\cdot}(bpy\text{-}t\mathrm{Bu})_2]^{2+}$	0.877	1.123	-
$[Co{\cdot}(bpy\text{-}t\mathrm{Bu})_2{\cdot}HCOO]^{+}$ (Isomer Co-QA)	1.034	0.602	-0.636
$[Ni{\cdot}(bpy\text{-}t\mathrm{Bu})_2{\cdot}HCOO]^{+}$ (Isomer Ni-TA)	0.938	0.670	-0.608
$[Cu{\cdot}(bpy\text{-}t\mathrm{Bu})_2{\cdot}HCOO]^{+}$ (Isomer Cu-A)	0.986	0.650	-0.636

IV. Conclusions

We used infrared photodissociation spectroscopy to measure the vibrational spectra of $[Co{\cdot}(bpy\text{-}t\mathrm{Bu})_2]^{2+}$ and $[M{\cdot}(bpy\text{-}t\mathrm{Bu})_2{\cdot}HCOO]^{+}$ (M = Co, Ni, Cu) in the fingerprint region. The vibrational modes of the bpy-*t*Bu ligands are well recovered by scaled harmonic DFT calculations, and show small red shifts upon addition of a formate ligand to the Co complex. These shifts are likely due to additional negative charge accommodated by the bpy-*t*Bu ligands. The complexation of a formate ligand generates new, intense features in the IR spectrum, namely the formate O–C–O symmetric (ν_s) and antisymmetric (ν_{as}) stretches. Simulated spectra do not accurately predict the absolute energies of these modes, but do quantitatively describe the splitting between them. The presence of the formate ligand is shown to sterically distort the orientation of the bpy-*t*Bu ligands, narrowing their angle relative to each other.

The identity of the metal center has a demonstrable effect on the formate binding motif: in both Co and Ni, the adduct binds in a symmetric, bidentate fashion. In Cu, it has a bidentate coordination to the metal center but is bound asymmetrically. This structural difference is encoded in the vibrational spectra vis-à-vis the ν_s–ν_{as} splitting, which increases in tandem with increased disparity in the C–O bond lengths. The calculated charge distributions of all complexes show that substantial charge transfer takes place between all three moieties: metal center, bpy-*t*Bu ligands, and formate. In the $[M\cdot(\text{bpy-}t\text{Bu})_2\cdot\text{HCOO}]^+$ complexes, the metal atoms carry a charge of less than +0.5 *e* despite their initial +2 oxidation state, while the bpy-*t*Bu ligands adopt nearly +1 *e* in their role as a charge reservoir for the catalyst.

V. References

(1) Sampson, M. D., Froehclich, J. D., Smieja, J. M., Benson, Sharp, I. D., Kubiak, C. P., Direct observation of the reduction of carbon dioxide by rhenium bipyridine catalysts. *Energy Environ. Sci.*, **2013**, 6, 3748-3755

(2) Benson, E. E., Kubiak, C. P., Sathrum, A. J., Smieja, J. M. Electrocatalytic and homogeneous approaches to conversion of CO2 to liquid fuels. *Chem. Soc. Rev.,* **2009**, *38*, 89-99

(3) Costentin, C., Robert, M., Saveant, J-M., Catalysis of the electrochemical reduction of carbon dioxide. *Chem. Soc. Rev.*, **2013**,*42*, 2423-2436

(4) Smieja, J. M., Kubiak C. P., Re(bipy-tBu)(CO)3Cl−improved Catalytic Activity for Reduction of Carbon Dioxide: IR-Spectroelectrochemical and Mechanistic Studies. *Inorg. Chem*. **2010**, *49*, 20, 9283–9289

(5) Costentin, C., Drouet, S., Robert, M., Saveant, J-M., A Local Proton Source Enhances CO2 Electroreduction to CO by a Molecular Fe Catalyst. *Science*. **2012**, *338*, 6103, 90-94

(6) Cosnier, S., Deronzier, A., Moutet, J-C., Electrocatalytic reduction of CO2 on electrodes modified by fac-Re(2,2'-bipyridine)(CO)3Cl complexes bonded to polypyrrole films. *J. Mol. Catal.* **1988**, *45*, 3, 380-391

(7) Saveant, J.-M. Molecular Catalysis of Electrochemical Reactions. Mechanistic Aspects. *Chem. Rev*. **2008**, *108*, 2348−2378.

(8) Manbeck, G. F.; Fujita, E. A Review of Iron and Cobalt Porphyrins, Phthalocyanines and Related Complexes for Electrochemical and Photochemical Reduction of Carbon Dioxide. *J. Porphyrins Phthalocyanines* **2015**, *19*, 45−64.

(9) Lin, S.; Diercks, C. S.; Zhang, Y.-B.; Kornienko, N.; Nichols, E. M.; Zhao, Y.; Paris, A. R.; Kim, D.; Yang, P.; Yaghi, O. M.; et al. Covalent Organic Frameworks Comprising Cobalt Porphyrins for Catalytic CO2 Reduction in Water. *Science* **2015**, *349*, 1208−1213.

(10) Beley, M.; Collin, J. P.; Ruppert, R.; Sauvage, J. P. Electrocatalytic Reduction of CO2 by Ni Cyclam2+ in Water: Study of the Factors Affecting the Efficiency and the Selectivity of the Process. *J. Am. Chem. Soc*. **1986**, *108*, 7461−7467.

(11) Ogata, T.; Yanagida, S.; Brunschwig, B. S.; Fujita, E. Mechanistic and Kinetic Studies of Cobalt Macrocycles in a Photochemical CO2 Reduction System - Evidence of Co-CO2 Adducts as Intermediates. *J. Am. Chem. Soc*. **1995**, *117*, 6708−6716.

(12) Hawecker, J.; Lehn, J. M.; Ziessel, R. Electrocatalytic Reduction of Carbon Dioxide Mediated by Re(Bipy)(CO)3Cl (Bipy = 2,2′- Bipyridine). *J. Chem. Soc., Chem. Commun.* **1984**, 328−330.

(13) Keith, J. A.; Grice, K. A.; Kubiak, C. P.; Carter, E. A. Elucidation of the Selectivity of Proton-Dependent Electrocatalytic CO2 Reduction by fac-Re(Bpy)(CO)3Cl. *J. Am. Chem. Soc.* **2013**, *135*, 15823−15829.

(14) Takeda, H.; Koizumi, H.; Okamoto, K.; Ishitani, O. Photocatalytic CO2 Reduction Using a Mn Complex as a Catalyst. *Chem. Commun*. **2014**, *50*, 1491−1493.

(15) Tanaka, K.; Ooyama, D. Multi-Electron Reduction of CO2 Via Ru-CO2, -C(O)OH, -CO, -CHO, and -CH2OH Species. *Coord. Chem. Rev*. **2002**, *226*, 211−218.

(16) Hawecker, J., Lehn, J-M., Ziessel, R., Electrocatalytic Reduction of Carbon Dioxide Mediated by Re(bipy)(CO)3Cl (bipy = 2,2'-bipyridine) . *J. Chem. Soc., Chem. Commun*., **1984**, 328-330

(17) Shimoda, T.; Morishima, T.; Kodama, K.; Hirose, T.; Polyansky, D. E.; Manbeck, G. F.; Muckerman, J. T.; Fujita, E. Photocatalytic CO2 Reduction by Trigonal-Bipyramidal Cobalt(II) Polypyridyl Complexes: The Nature of Cobalt(I) and Cobalt(0) Complexes Upon Their Reactions with CO2, CO, or Proton. *Inorg. Chem*. **2018**, *57*, 5486−5498.

(18) Bochlin, Y.; Korin, E.; Bettelheim, A. Different Pathways for CO2 Electrocatalytic Reduction by Confined CoTMPyP in Electrodeposited Reduced Graphene Oxide. *ACS Appl. Energy Mater*. **2019**, *2*, 8434−8440.

(19) Dey, S.; Todorova, T. K.; Fontecave, M.; Mougel, V. Electroreduction of CO2 to Formate with Low Overpotential Using Cobalt Pyridine Thiolate Complexes. *Angew*. *Chem., Int. Ed.* **2020**, *59*, 15726−15733.

(20) Becke, A. D. Density-Functional Thermochemistry 0.3. The Role of Exact Exchange. *J. Chem. Phys*. **1993**, *98*, 5648−5652.

(21) Hay, P. J., Wadt, W. R., *Ab initio* effective core potentials for molecular calculations. Potentials for K to Au including the outermost core orbitals. *J. Chem. Phys*. **82**, *299* (1985)

(22) Frisch, M. J.; Trucks, G. W.; Schlegel, H. B.; Scuseria, G. E.; Robb, M. A.; Cheeseman, J. R.; Scalmani, G.; Barone, V.; Petersson, G. A.; Nakatsuji, H.; et al. Gaussian 16, Rev. C.01; Gaussian Inc.: Wallingford, CT, **2016**.

(23) Gerardi, H. K.; DeBlase, A. F.; Su, X.; Jordan, K. D.; McCoy, A. B.; Johnson, M. A. Unraveling the Anomalous Solvatochromic Response of the Formate Ion Vibrational Spectrum: An Infrared, Ar-Tagging Study of the HCO 2 $^{-}$, DCO 2 $^{-}$, and HCO 2 $^{-}$ ·H 2 O Ions. *J. Phys. Chem. Lett*. **2011**, 2 (*19*), 2437–2441.

4. EDTA

This chapter has been reproduced in part from the following previously published articles:

Madison M. Foreman and J. Mathias Weber, "Ion Binding Site Structure and the Role of Water in Alkaline Earth EDTA Complexes" *The Journal of Physical Chemistry Letters* **2022** *13* (36), 8558-8563
DOI: 10.1021/acs.jpclett.2c02391

Madison M. Foreman, Maristella Alessio, Anna I. Krylov, and J. Mathias Weber, "Influence of Transition Metal Electron Configuration on the Structure of Metal–EDTA Complexes" *The Journal of Physical Chemistry A* **2023** *127* (10), 2258-2264
DOI: 10.1021/acs.jpca.2c07996

I. Introduction

Supramolecular structures that bind metal dications are involved in a wide array of chemical and biological processes, from metal-binding proteins operating in signal transduction and muscle action, [1–3] removal of toxic metal cations, [4] and electrolytes for flow batteries [5]. Ethylenediaminetetraacetic acid (EDTA) is an incredibly versatile chelator for metal cations and will bind most metal 2+ and 3+ ions with its four carboxylate groups and two nitrogen atoms forming the binding pocket (see Scheme 4.1). [6]

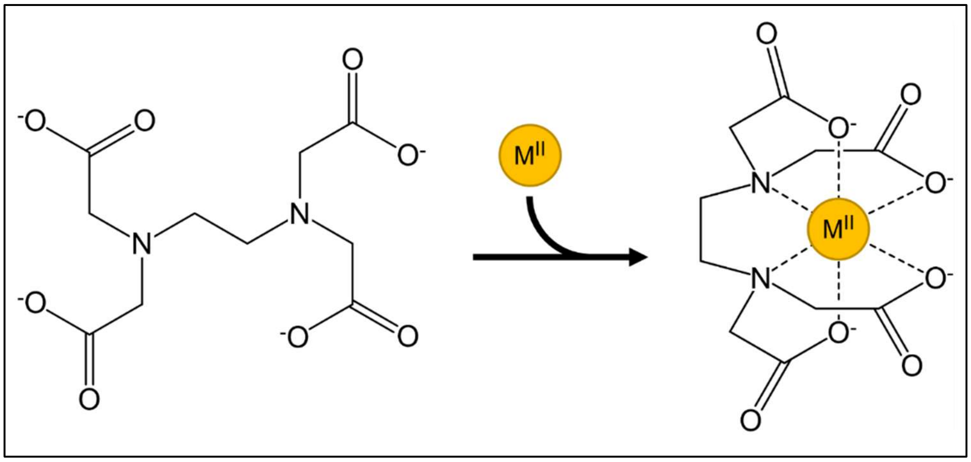

Scheme 4.1. The deprotonated form of EDTA binds metal dications and, in the case of alkaline earth metals, typically forms a hexa-coordinated complex.

The ubiquity of EDTA is owed in large part to the flexibility with which it accommodates atoms of varying size and electronic structure. Its binding pocket can expand and contract to hold metal ions through a range of atomic radii, and it can adopt different binding motifs based on the identity of the bound ion. [7–10] While Ca^{2+} and the other alkaline earth metals present to their chemical environment as simple, spherically symmetric charge distributions, transition metal ions structure their environment through the occupation of their d-orbitals. In response to these changes in electron geometry, EDTA forms hexacoordinate complexes with C_2 symmetry for alkaline earth metals (Figure 4.1) and is able to adopt a multitude of additional structural motifs for transition metals.

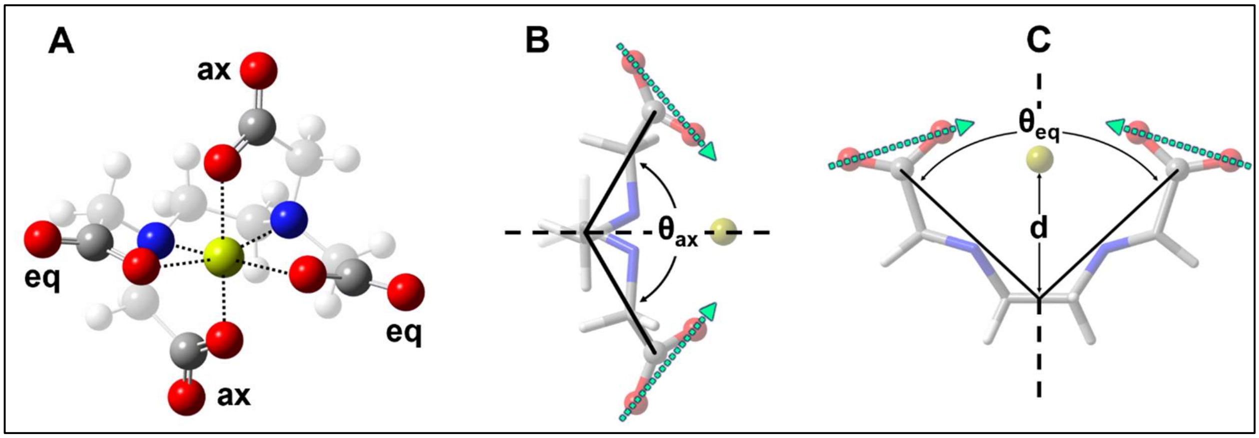

Figure 4.1. Geometry of EDTA complexes with alkaline earth dications. **A)** Calculated ball-and-bond type structure of $[M(II)\cdot EDTA]^{2-}$ highlighting the binding pocket. Axial and equatorial carboxylate ligands are labeled "ax" and "eq", respectively. **B)** Axial slice of $[M(II)\cdot EDTA]^{2-}$ with the definition of the axial opening angle, θ_{ax}. **C)** Equatorial slice of $[M(II)\cdot EDTA]^{2-}$ with the definition of the equatorial opening angle, θ_{eq}, and the ion position, d. In parts B and C, the C_2 axis is shown as a dashed line, and green dashed arrows indicate the direction of the transition dipole in each carboxylate group. Colors for the highlighted atoms: red for O, dark gray for C, blue for N, and yellow for the metal ion.

One of the many applications of EDTA is its use as a model system for Ca^{2+} binding pockets in calmodulin and other proteins in the EF hand structural family, which are similarly constructed from carbonyl and carboxylate functional groups that interact with the ion.

[3,15,16] The properties of these binding sites are dependent on the structure of the binding pocket and electrostatic interactions with the bound ion, and these parameters are influenced by the chemical environment surrounding the pocket. Not only does the environment created by the protein around the pocket affect its characteristics, but the presence of water molecules can affect the host-guest interactions between pocket and cation by interacting with both the metal and the constituents of the binding pocket. Hydration-induced effects regulate the relative competitiveness of ion binding vs. hydration, leading to macro-scale differences in ion binding and selectivity. [17–18]

In the present work, we use cryogenic ion vibrational spectroscopy to characterize the IR signatures encoding the structure of EDTA binding two series of metallic dications: the alkaline earth metals Mg, Ca, Sr, and Ba and the transition metals Mn, Co, Ni, Cu, and Zn. We additionally probe the binding pocket's response to hydration by measuring the vibrational spectra of the alkaline earth metal complexes in clusters with one or two water molecules as well as in solution.

II. Methods

a. Experimental

Electrospray solutions of $[M(II)\cdot EDTA]^{2-}$ (M = Mg, Ca, Sr, Ba, Mn, Ni, Co, Cu, Zn) were prepared by first making ca. 5 mM aqueous stock solutions titrated to a pH of 12-14 with KOH (Fisher-Scientific). Aliquots of stock solution were diluted to final concentrations of ca. 0.3–1 mM; for preparation of the bare complexes, acetonitrile (Fisher-Scientific) was used, while for the hydrated complexes, the electrosprayed solutions had a 50:50 (by volume) mixture of water and acetonitrile as solvent. Stock solutions of $[Mg(II)\cdot EDTA]^{2-}$ and $[Ca(II)\cdot EDTA]^{2-}$ were prepared with EDTA magnesium disodium salt and EDTA calcium disodium salt, respectively (both Fisher-Scientific). For M = Sr, Ba, Mn, Ni, Co, Cu, and Zn, solutions were prepared with

EDTA and the corresponding metal salt ($MnCl_2$, $CoCl_2$ or $Co(NO_3)_2{\cdot}(H_2O)_6$, $Cu(NO_3)_2{\cdot}(H_2O)_3$, $ZnCl_2$, and $Ni(NO_3)_2(H_2O)_3$). Solutions of Mn(II) ions and EDTA were adjusted to pH 5 using KOH and HCl to optimize ion production. Similarly, solutions of EDTA with Zn(II) and Ni(II) were adjusted to pH = 8−12. We note that we were unable to generate analogous Fe(II) complexes. This problem has been commented on by Wang and co-workers, [10] who attributed the difficulty of electrospraying [Fe(II)·EDTA]2− to oxidation during the electrospray process and hypothesized that these complexes may not be electrochemically stable. All chemicals were used as received, and all solutions were sprayed without further purification.

Fourier Transform IR-Attenuated Total Reflection (FTIR-ATR) experiments were performed using an Agilent Cary 630 FTIR Spectrometer averaging 400 scans per spectrum. All solutions were prepared in D_2O (Cambridge Isotope Laboratories) at a concentration of ca. 40 mM. Solutions of $[Mg(II){\cdot}EDTA]^{2-}$ and $[Ca(II){\cdot}EDTA]^{2-}$ were prepared with EDTA magnesium disodium salt and EDTA calcium disodium salt, respectively (both Fisher-Scientific). $[Sr(II){\cdot}EDTA]^{2-}$ and $[Ba(II){\cdot}EDTA]^{2-}$ solutions were prepared by dissolving approximately equimolar amounts of EDTA and strontium nitrate or barium nitrate (both Sigma-Aldrich), respectively, and then titrating to a pD of 13-14.5 with NaOD (Thermo Scientific). Relative intensities I_a were extracted from the FTIR-ATR data for all complexes between 1500 cm-1 and 1700 cm-1 using the LabSpec V.5.64.15 program (Horiba). The baseline in this range was subtracted using a second order polynomial baseline fit, followed by Lorentzian peak fitting. We conservatively estimate the error bars to be a factor of two larger than those for the data points in vacuo.

The experimental setup for all *in vacuo* measurements is described in Chapter 2.

b. Computational

b.1. Alkaline Earth Metal Complexes

Geometry optimizations and vibrational spectra simulations of all complexes under study were performed using spin-unrestricted DFT (B3LYP functional [19,20] and def2-TZVPP basis set for all atoms). Exploratory calculations with the functionals PBE0 ωB97XD and M062X9 show that the results for B3LYP and PBE0 most closely resemble the relative intensity of I_a for the IR spectrum of $[Ca(II)\cdot EDTA]^{2-}$ in vacuo (see Appendix B for comparison). The B3LYP results were therefore taken as a reference point for the model described in the main text. All geometries shown in this work are minimum energy structures, and all complexes have singlet spin states. The infrared spectra of all complexes were calculated using the harmonic approximation. A scaling factor of 0.977 was applied to all O–C–O antisymmetric stretching vibrational frequencies, matching the calculated values for features a and b to the experimental spectrum of $[Ca(II)\cdot EDTA]^{2-}$. All other vibrational frequencies were scaled by 0.990 to achieve an optimal match with the lower frequency modes. Condensed phase IR spectra and structures were simulated employing a polarizable continuum model using the dielectric constant of water (78.36), the B3LYP functional and the same basis sets as for the calculations in vacuo. All calculations were performed using Gaussian 16. [21]

b.2. Transition Metal Complexes

Structures, adiabatic gaps, and IR spectra of the hexacoordinated $[M(II)\cdot EDTA]^{2-}$ ions under study were calculated in the framework of density functional theory (DFT) using two hybrid functionals (B3LYP [19,20] and B5050LYP [22]) and one long-range corrected hybrid DFT with empirical dispersion (ωB97X-D [23]). Scaled B3LYP, B5050LYP, and ωB97xD functionals provided similar-quality description of the main features in the spectra with respect to experiment, and we selected ωB97xD for all spectra presented in this work. The def2-TZVPP basis set [24] was used for all atoms. These calculations were performed using the Q-Chem electronic structure package. All frequencies were scaled by 0.950 to match the most intense feature of the antisymmetric O–C–O stretching region in $[Ca(II)\cdot EDTA]^{2-}$. All computational spectra were broadened by a Lorentzian with 8 cm^{-1} full width at half-maximum. Additionally, for $[Mn(II)\cdot EDTA]^{2-}$, to screen the spectrum of its low-lying spin states, we performed spin-flip time-dependent (SF-TD)-DFT calculations [22] (using B5050LYP and a noncollinear kernel [25,26]), which yielded sextet and quartet spin states. Simulations of the complexes in solution were carried out using a polarizable continuum model [27] with the dielectric constant of water (78.36), the ωB97X-D functional, and def2-TZVP basis sets for all atoms [24], employing Gaussian 16 [21].

III. Results and Discussion

a. Alkaline Earth Metal Complexes

The vibrational spectra of all four $[M^{II}\cdot EDTA]^{2-}$ (M = Mg, Ca, Sr, Ba) complexes are compared to their simulated counterparts in Figure 4.2. These complexes exhibit two major bands in the fingerprint region, corresponding to the carboxylate O–C–O symmetric (ν_s) and antisymmetric (ν_{as}) stretches which appear at 1340–1390 cm^{-1} and 1610–1690 cm^{-1}, respectively. This study focuses almost entirely on the antisymmetric stretching region, which is comprised of four linear combinations of in- and out-of-phase O–C–O antisymmetric stretching vibrations. Figure 4.3 illustrates the patterns of motion of each of the ν_{as} transitions.

The few very weak C–H wagging modes predicted by calculations below ca. 1350 cm^{-1} do not appear with enough intensity for any interpretation. In each spectrum, the symmetric stretching feature (ν_s) appears as a broad, low-intensity peak in the mid-1300 cm^{-1} range. While the peak does red shift across the series of bound metals (Mg = 1371cm^{-1}, Ca = 1365 cm^{-}

^{1}, Sr = 1362 cm^{-1}, and Ba = 1362 cm^{-1}), we do not resolve any meaningful changes in its substructure.

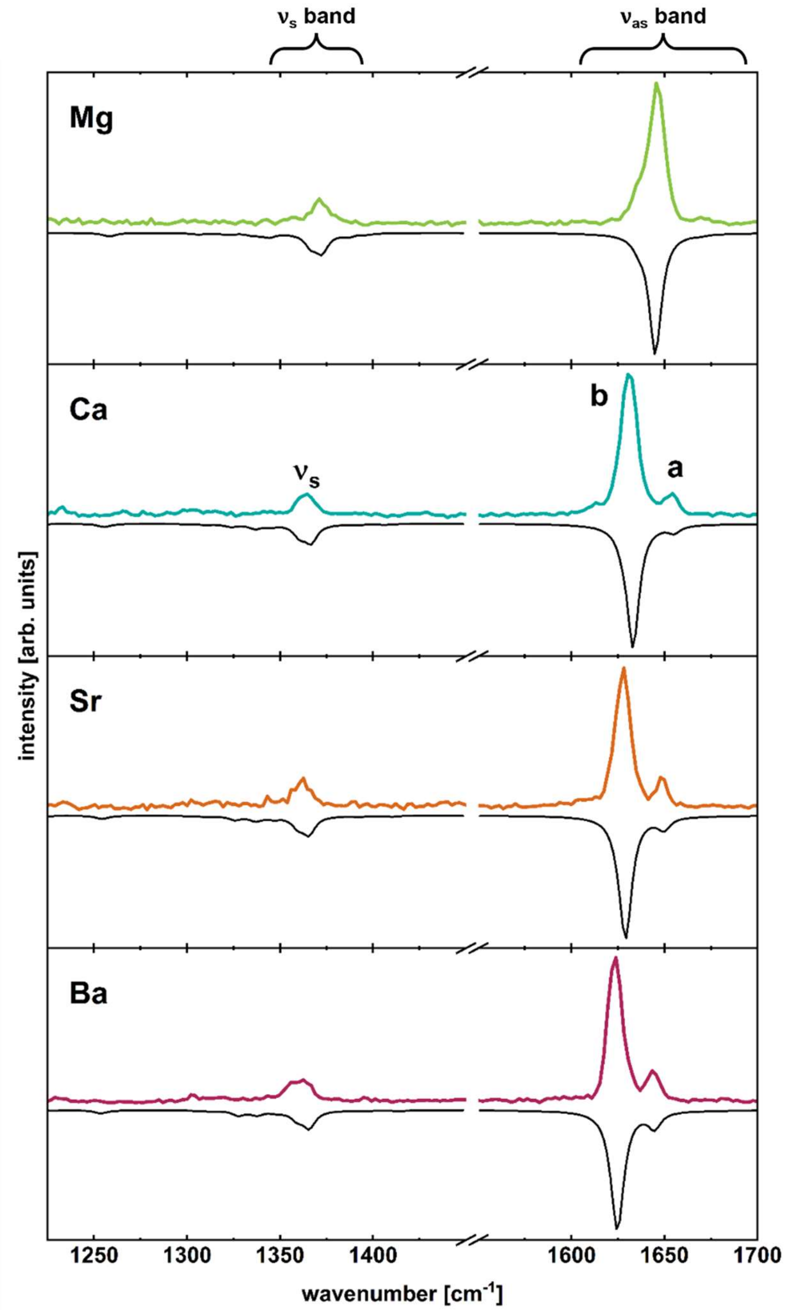

Figure 4.2. Comparison of experimental (upright traces) and simulated (inverted traces) spectra of [M(II)·EDTA]$^{2-}$ complexes. The metal is indicated above each set of traces (top to bottom: Mg, Ca, Sr, and Ba). Simulated IR spectra are based on scaled harmonic calculations with each mode represented by a Lorentzian line shape with an 8 cm^{-1} full width at half-maximum. See text for a discussion of features a and b.

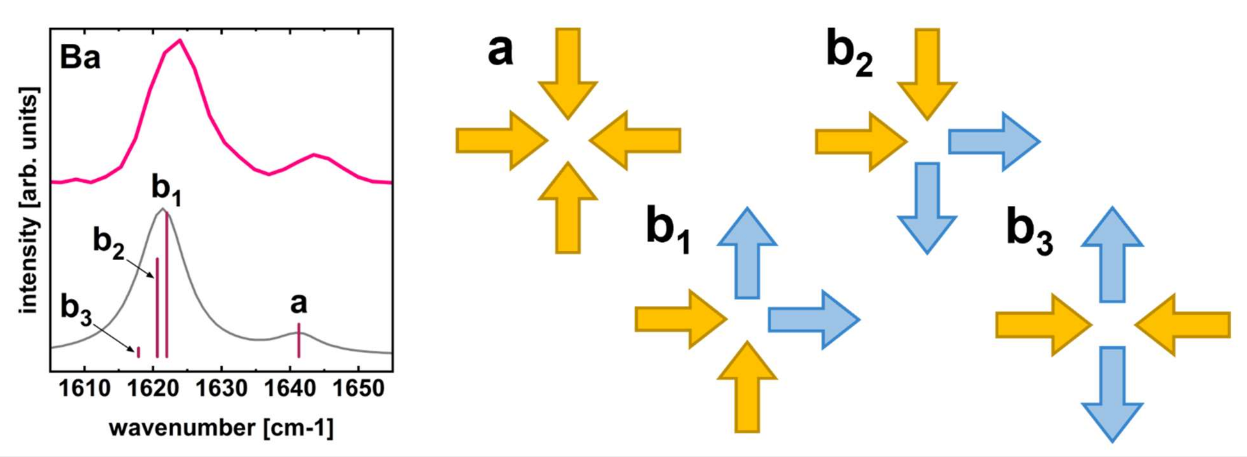

Figure 4.3. Antisymmetric O–C–O stretching modes of [M(II)·EDTA]$^{2-}$ complexes. **Left:** Experimental and simulated spectra of M = Ba with individual ν_{as} transitions labelled to illustrate frequency ordering. **Right:** Patterns of motion for the antisymmetric O–C–O stretching modes as denoted on the left. Note that the a, b_1, b_2, and b_3 labels only designate individual ν_{as} transitions and are not spectroscopic notation.

More interestingly, we also find that the intensity of peak **a** relative to that of peak **b** increases as the size of the bound ion increases. To quantify this observation, peaks **a** and **b** were fit with Lorentzian functions, and the area under each curve was taken. Peak **a** was fit with a single function, while peak **b** was fit with three to better reflect the nature of the feature (relevant largely for the Mg complex). The relative intensity of peak **a**, I_a, was found according to equation 1, where the A values are the area under each curve:

$$I_a = \frac{A_a}{A_a + A_{b1} + A_{b2} + A_{b3}} \tag{1}$$

The relationship between I_a and the size of the bound ion originates from changes in the local transition dipole moments in each carboxylate group as the binding pocket accommodates larger ions. For the mode associated with peak **a**, the O–C–O antisymmetric stretching transition dipoles of each equatorial and axial pair are antiparallel in the radial plane about the C_2 symmetry axis of the complex. As a result, only the component of each transition dipole moment along the symmetry axis is left to generate infrared activity for transition **a** (see Figure 4.4). As larger ions displace the carboxylate groups outward, the opening angles of the binding pocket increase, and the projection of the transition dipole along the C_2 axis increases as well. In short, the structural change results in the growth of I_a along the sequence from Mg^{2+} to Ba^{2+}.

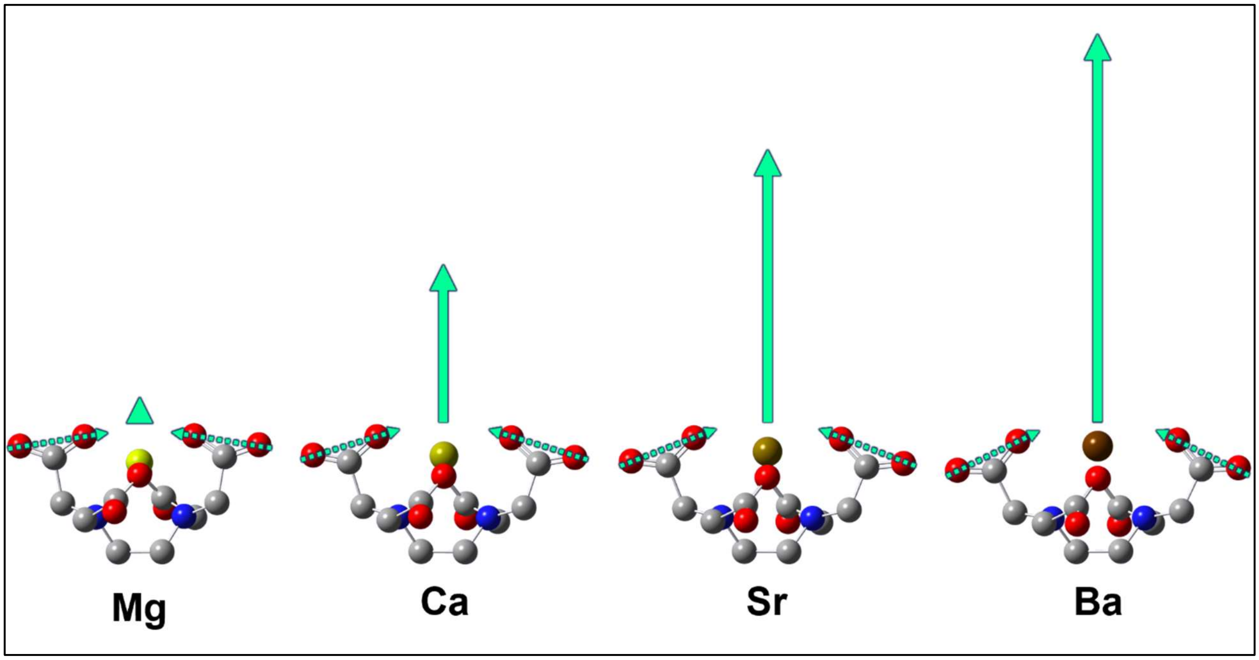

Figure 4.4. Graphical depiction of local O–C–O antisymmetric stretching transition dipole moments (μ_{loc}) producing the total transition dipole moment (μ_{tot}) for the mode associated with peak **a**. Equatorial slice shown for $[M(II)\cdot EDTA]^{2-}$ M = Mg, Ca, Sr, Ba. The dashed green arrows qualitatively represent μ_{loc} for each carboxylate group, the solid green arrows represent μ_{tot} and are quantitatively shown to scale with each other.

This direct correlation allows us to quantitatively model the binding pocket geometry by predicting the equatorial and axial opening angles, θ_{eq} and θ_{ax}, and the ion position, d, from fits of the calculated geometry parameters as a function of the calculated I_a (Figure 4.5). The ion position is linearly proportional to I_a, while the equatorial and axial angles can be described as in equation 2, where δ is a fitting parameter and θ denotes either the equatorial or axial angle:

$$I_a \propto \sin^2\left(\frac{\theta}{2} - \delta\right) \tag{2}$$

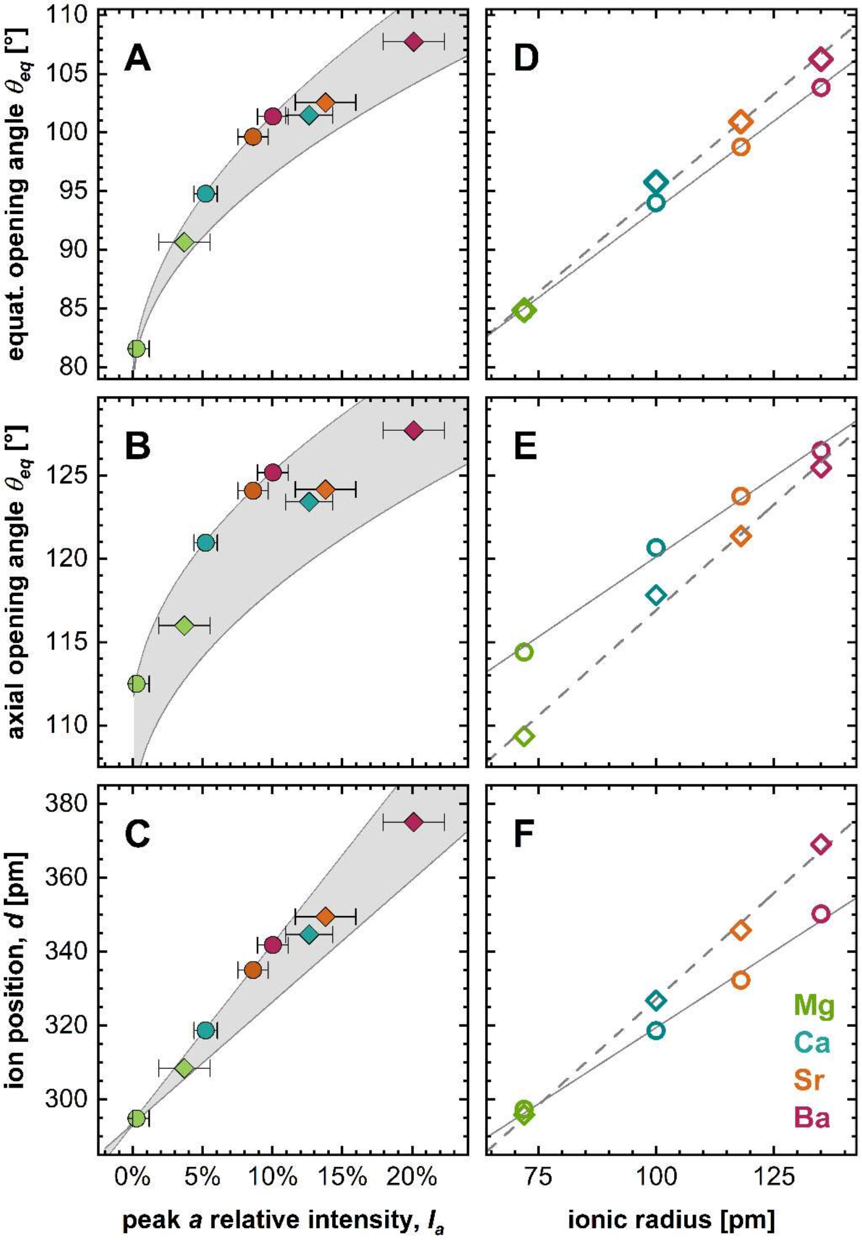

Figure 4.5. Correlation of the ion size and the relative intensity I_a with geometry parameters of the binding pocket. Data for hydrated complexes is discussed in part b of this section. Data points are color coded for each metal as shown in panel F. **A)** equatorial opening angle, **B)** axial opening angle, and **C)** ion position as defined in Figure 4.1, determined from the experimental relative intensity of peak a for each metal. **D)** Calculated equatorial opening angle, **E)** axial opening angle, and **F)** ion position as a function of ionic radius for each metal. Filled circles represent experimental data from $[M(II)\cdot EDTA]^{2-}$ complexes in vacuo. Filled diamonds show experimental data taken in aqueous solution (D_2O). Empty circles and diamonds represent calculated values for $[M(II)\cdot EDTA]^{2-}$ complexes in vacuo and with PCM, respectively. In each of the three data sets, I_a increases from Mg^{2+} to Ba^{2+}. The gray shaded areas, determined by using the calculations in vacuo and with the PCM model as limiting cases, allow estimates of the

geometry parameters of the EDTA binding pocket in aqueous solution. Error bars are ±1σ uncertainties arising from a nonlinear parameter fit of the peak areas for peaks a and b.

The linear correlation between d and I_a is empirical, while the behavior of θ is based on the physical model behind I_a (eq. 2). As the size of the chelated ion increases, both the calculated and (structurally dependent) experimental I_a values increase, which lends credence to the models extracted from computational data. Through the framework of these calculated relations, we can extract the geometry parameters in each EDTA complex from the experimental values of I_a, rather than relying on the calculated angles alone. Along the sequence of alkaline earth metals, the opening angles of the binding pocket and the distance of the ion from the central C–C bond increase (parameters defined in Figure 4.1), indicating that larger ions are bound closer to the mouth of the binding pocket, and that the overall bite angle of the pocket widens. The ionic radius increases along the sequence from Mg^{2+} to Ba^{2+}, so chemical intuition may lead one to expect this trend in geometry change (Mg^{2+}, Ca^{2+}, Sr^{2+}, and Ba^{2+} have ionic radii of 0.72, 1.00, 1.18, and 1.35 Å, respectively). [28] The correlation between ionic radius and each of the three geometry parameters modeled appears to be nearly linear, but we do not infer any (predictive) model with this purely empirical trend.

As a check on the validity of our use of I_a as a structural probe, we considered it prudent to take into account the influence of the chemical identity of the bound ion. To this end, we carried out ion-swapping tests based on a similar procedure by Mitra et al. We began with the calculated structure of one $[M^{II}\cdot EDTA]^{2-}$ complex (e.g., for M = Ca) and switched the metal center for another (e.g., Mg). The vibrational spectrum was then recalculated without reoptimizing the complex geometry, which tests the dependence of the vibrational spectrum on the local electric field around the ion, independent of changes in the geometry of the EDTA pocket. This process was carried out in parallel for two pairs of complexes: Mg/Ca and Ca/Ba. The results of these calculations are shown in Figure 4.6. In every test, I_a was insensitive to the change of ion, despite substantial shifts in the electric field within the binding pocket. It is worth noting that the swapping of ions leads to changes in the splitting between peaks **a** and **b** by up to 20%, and substitution of a smaller ion into a binding pocket caused higher frequencies to be predicted for these two features. Nonetheless, the ion-swap tests indicate that I_a is a robust probe for the local geometry of the binding pocket.

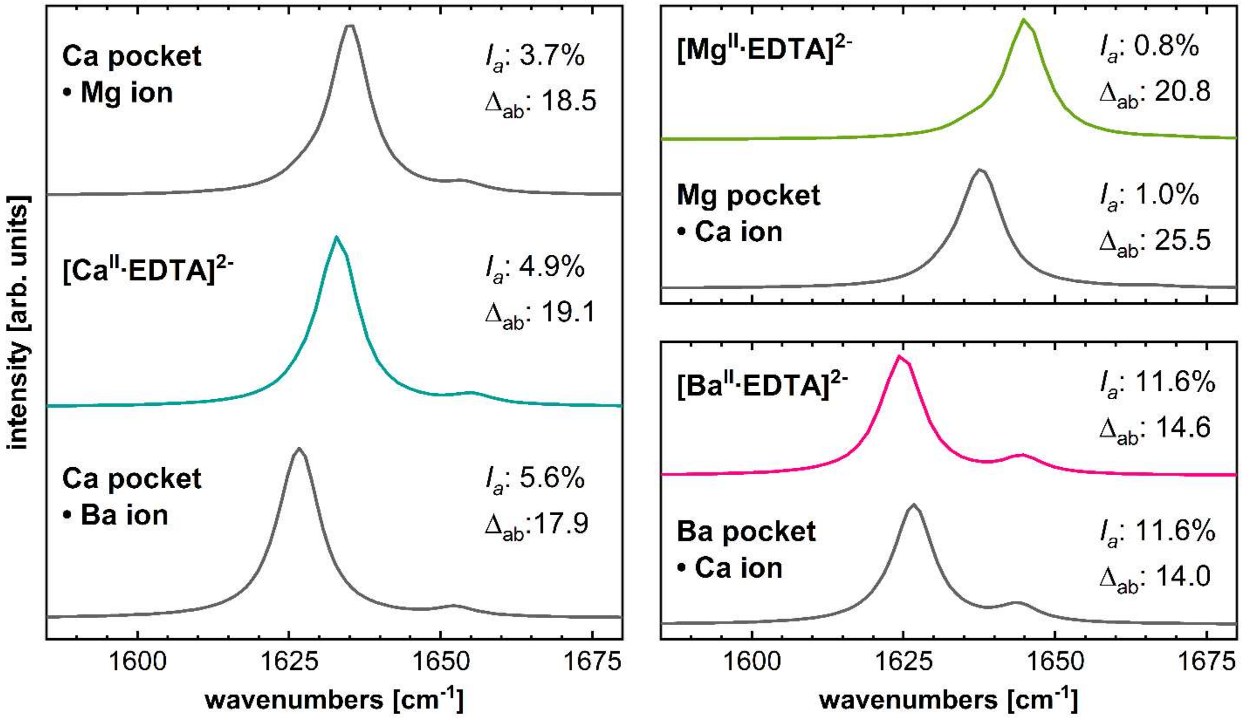

Figure 4.6. Comparison of simulated spectra for the region of the antisymmetric O–C–O stretching vibrations resulting from swapped calculations. Intensity I_a and splittings (in cm^{-1}) between peaks **a** and **b** for the swapped ion calculations are given for each simulation.

In addition to the changes in relative intensity observed as the spectra evolve from Mg^{2+} to Ba^{2+}, the frequencies of **a** and **b** shift as well (by a total of 23 and 19 cm^{-1}, respectively). The positions of these peaks relate in part to the geometry of the binding pocket but are impacted by other factors, in contrast to the intensity ratio. While one contribution is the overall complex geometry, the electric field generated by the metal ion at the positions of the carboxylate groups also impacts the vibrational frequencies, which can be qualitatively described in terms of the vibrational Stark effect. These two factors also influence one another (see Figure 4.6). An additional influence on the frequencies of **a** and **b** is the local asymmetry of the C–O bond lengths between the “inner” O atom coordinating the metal and the “outer”, free O atom in each carboxylate group (Figure 4.1 B, C). This asymmetry affects the local modes of each carboxylate group, in turn influencing the normal modes of the complex and therefore the splitting of peaks **a** and **b** of the combined antisymmetric stretches (see Chapter 5 for a longer discussion of factors governing carboxylate stretching modes). As a result of the subtle interplay of multiple factors, the frequency positions of the peaks are less straightforward to use as a tool for determining the geometry of the binding pocket quantitatively, but we can qualitatively associate a lower frequency with a more open binding pocket and an ion position closer to the rim of the pocket, at least for the case of alkaline earth ions. Section c will discuss the deviation from straightforward structural effects on peak positions due to the electron geometry of bound transition metal ions.

b. Hydration of AEM Complexes

Figure 4.7 shows the experimental spectra of $[M(II)\cdot EDTA]^{2-}$ (M = Mg, Ca, Sr, Ba) in the EDTA carboxylate antisymmetric stretching region with different levels of hydration: bare ion, presence of one water adduct, two water adducts, and fully hydrated in D_2O solution. It is readily apparent that evolution of the solvent environment brings about spectral changes that signal shifts in both the geometry and intramolecular electric fields of the complexes. Part of this change includes the convolution of the EDTA carboxylate ν_{as} modes and the water bending mode, whose native frequency is 1595 cm^{-1}. [29]

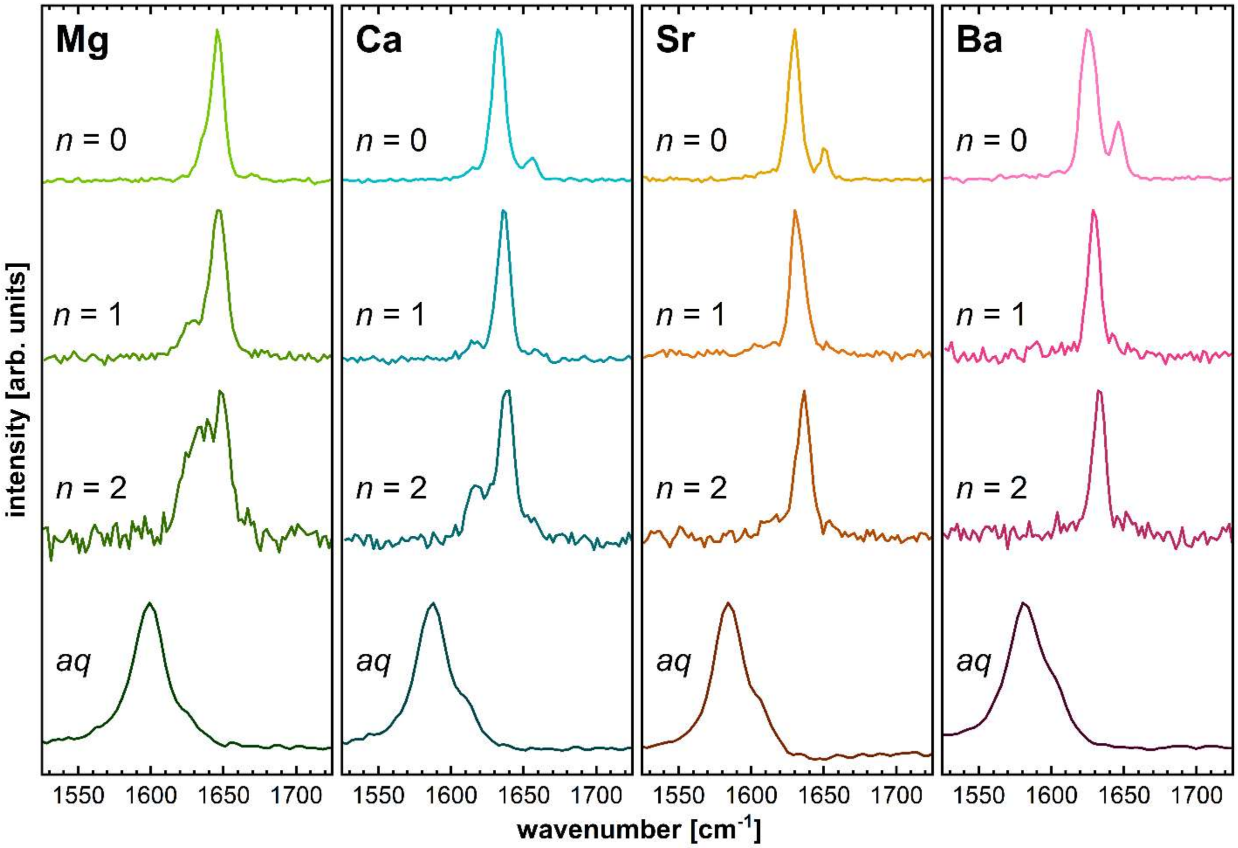

Figure 4.7. Experimental spectra of bare $[M(II)\cdot EDTA]^{2-}$ complexes (top row), $[M(II)\cdot EDTA]^{2-}\cdot(H_2O)_n$ cluster ions (second and third rows), and bulk solutions of $[M(II)\cdot EDTA]^{2-}$ in D_2O (bottom traces) in the antisymmetric O–C–O stretching region of the EDTA moiety. The metal ion is indicated in the top panel of each column. The colors in each column turn darker with increasing level of hydration.

In the singly and doubly hydrated complexes, the high energy peaks (denoted **a** exclusively for the bare complexes in Figure 4.2, but not so for the hydrated complexes where mixing with the water bend changes the nature of the modes) diminish, to the point of vanishing entirely in some spectra. In some cases, new features emerge as low-energy shoulders on the intense peaks — most notably for Mg and Ca, while Sr and Ba show little if no intensity to the red of the main peak. Addition of the first water molecule causes a small blue-shift of 1 – 4 cm^{-1} for the most intense peak, and the second water adduct brings about an additional 1 – 5 cm^{-1} energy increase.

Once fully hydrated, the complexes demonstrate a major red shift in the carboxylate antisymmetric stretching band — 45 – 47 cm^{-1} — but also recover the spectral pattern of the bare complexes with two partially resolved peaks corresponding to the **a** and **b** assignments discussed above (note that there is no water bending feature present, since D_2O is the solvent). This shift to lower frequencies is opposite to the shift observed for the microhydrated species, so we do not observe a smooth transition from the peak positions of the bare species to the hydrated complex as the solvent environment evolves.

Obtaining computational predictions that accurately capture the nature of each hydration state is nontrivial and becomes more challenging as the degree of hydration increases. The addition of solvent molecules raises the computational cost due to both the increase in total size of the system and the large number of possible solvent conformations around a solute complex as large as the ones studied in this work. While the mono- and di-hydrated complexes are still within the realm of feasible DFT calculations for us, calculations in which solvent molecules are explicitly accounted for with one or more full hydration shells (which could potentially include 4-10+ water molecules) [30,31] become prohibitively expensive. An alternate strategy is the use of polarizable continuum models (PCM) for solvation, which reduce computation time by neglecting the molecular structure of the solvent and, instead rely on modeling a dielectric medium around the solute. This simplification makes predictions less reliable, particularly in the case of water, which forms hydrogen-bonded solvation networks that influence the interactions between solute and solvent on a molecular level.

b.1. Full Hydration

The PCM calculations succeed in recovering the observed red shift of **b** in aqueous solution (see Figure 4.8). This is an indication that they capture some of the solvation-induced changes in the charge distribution throughout the carboxylate groups, since shifts in charge distribution will affect the force constants of the individual C–O oscillators and concomitantly affect the frequencies of the O–C–O stretching vibrations. In each of the solution-phase $[M(II)\cdot EDTA]^{2-}$ complexes, the relative intensity of peak **a** increases, signaling that the structure of the binding pocket adjusts to the new chemical environment.

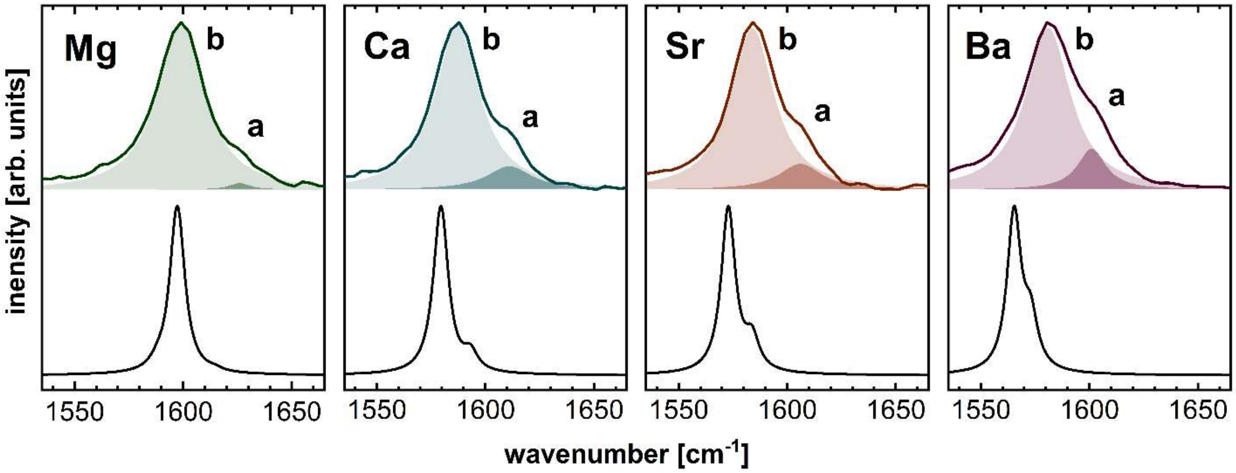

Figure 4.8. Comparison of experimental (top) and simulated (bottom) spectra of aqueous $[M(II)\cdot EDTA]^{2-}$ complexes. The identity of the metal is indicated at the top of each plot. Shaded curves represent Lorentzian fits to experimental peaks **a** and **b**. Simulated spectra obtained from PCM calculations, experimental spectra are of $[M(II)\cdot EDTA]^{2-}$ in D_2O.

We use the PCM calculations to expand the model shown in Figure 4.5 by constructing additional curves for the equatorial and axial opening angles and ion position as a function of I_a in the presence of a solvent. We note that while the calculations for bare complexes recover the splitting between peaks **a** and **b** quite well, the PCM calculations predict a narrowing of the splitting, while the experimental splitting increases for all metals under study, leading to a deviation of the calculations by a factor of 2. Additionally, the predicted values of I_a from the PCM calculations are a qualitatively worse match for the solution phase spectra than the computational–experimental comparison for the gas phase data. Taking into account these discrepancies, we judge that the accuracy of the PCM based curves in Figure 4.5 is lower than for the bare complexes, and we therefore treat the model curves from the two scenarios (bare ions vs PCM) as limiting cases for the modeled pocket geometry in aqueous solution to estimate the geometric parameters for the EDTA binding pocket from the experimental values of I_a in aqueous solution (gray shaded areas in Figure 4.5).

The model describes a less pronounced opening of θ_{ax} than θ_{eq} upon hydration because the EDTA framework relaxes not just by opening the bite angles of the ligands, but also by twisting the axial carboxylate groups around the C–C bond connecting them to the rest of the EDTA structure. Based on these model curves, which relate I_a to the geometry of the binding pocket, we predict that full hydration leads to a more open, and therefore shallower, binding pocket and a binding position of the ion closer to the rim of the pocket than in the bare complex. The opening angle increases by ca. 9° for Mg^{2+} and ca. 6° for Ba^{2+}, and full hydration brings Mg^{2+} by ca. 0.14 Å further out of the pocket, while Ba^{2+} changes its position in the pocket by ca. 0.33 Å. We qualitatively explain the dependence of the binding pocket geometry on the level of hydration with the structural evolution of the solvent environment. In the case of full hydration, the interactions between solvent molecules and within the water network itself will exert control over the geometry of the EDTA complexes. When completely solvated, most water molecules not directly at the opening of the pocket will only bind to the outer O atoms of the carboxylate groups. These water molecules will form H-bonds with additional molecules, building a hydration network around the complex. The attractive interaction of water molecules with both the outer carboxylate O atoms and neighboring water molecules may exert a net force on the carboxylate groups that pulls the pocket open and the ion closer to the rim of the binding pocket — which would explain the increase of I_a in aqueous solution compared to *in vacuo*. This seems to be the case even if we neglect explicit hydrogen bonding and just describe the interaction of the charge distribution of the EDTA complex with a polarizable continuum, evidenced by the success of the PCM model in qualitatively capturing the changes in ion position and opening angles.

b.2. Singly Hydrated EDTA Complexes

DFT calculations produced three low-lying minimum-energy isomers of $[M(II)\cdot EDTA]^{2-}\cdot H_2O$ for each metal (see Figure 4.9), each with a unique water binding motif.

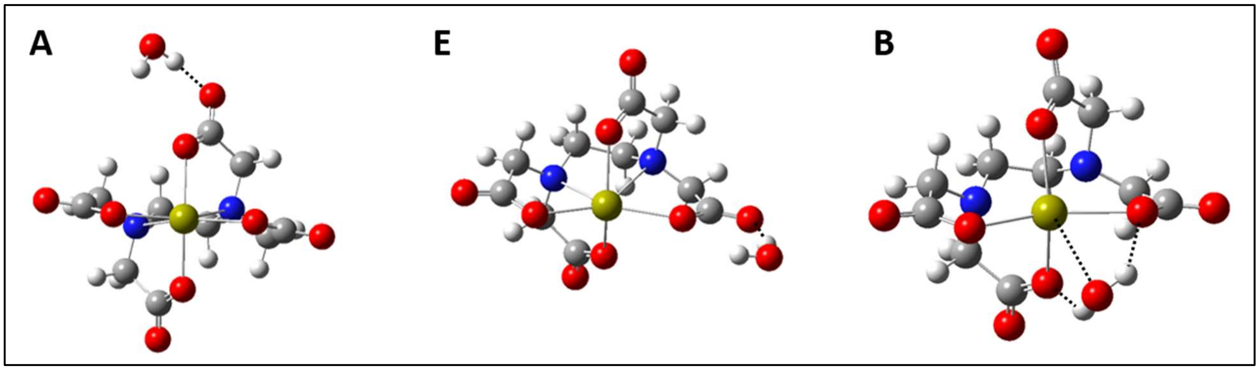

Figure 4.9. Structural motifs for $[M(II)\cdot EDTA]^{2-}\cdot H_2O$, shown using the calculated structures for M = Ca as an example. **A**: water molecule H-bonded to an axial ligand; **E**: water molecule H-bonded to an equatorial ligand; **B**: water molecule bridging axial and equatorial ligands. Color scheme: M: yellow; O: red; N: blue; C: gray; H: white. Primary interactions of the water adduct are shown as dotted lines.

The **A** structures have the water molecule adhering to one of the axial carboxylate groups. The water forms a strong, linear single hydrogen bond (H-bond) to the outer O atom of the ligand, and interacts weakly with the inner O atom without forming a second H-bond. This behavior differs from that of singly hydrated carboxylate anions, which form two H-bonds through the carboxylate O atoms to the H atom of the water molecule to create a double H-bond. [32]. In the case of our EDTA complexes, the asymmetric binding of the water adduct suggests that the proximity of the metal dication to the inner O atom of the axial carboxylate prevents the formation of a second H-bond between the water and the inner O atom. Likely, the electric field generated by the ion is sufficiently repulsive to to destabilize interactions between a H atom of the water and the inner O atom. Interestingly, the inner O atom is more negatively charged than the outer, which one may expect would encourage H-bond formation. However, structure optimizations started with an H-bond between the water molecule and the inner O atom relaxed into the structures shown in Figure 4.9.

The **E** structural motif exhibits the water molecule H-bonding to an equatorial carboxylate ligand in an analogous fashion to the water–carboxylate interaction in structure **A**.

The third structure, **B**, is characterized by the water molecule forming a double H-bond to the inner O atoms of an axial and equatorial group, in effect forming a bridge between them. We also observe the lone pair of the water O atom interacting with the positively charged metal center to a varying degree in each complex.

The relative stability of each isomer is not independent of metal identity. In fact, we observe a trend in lowest energy isomers (Table 4.1) across the series from Mg to Ba. In all cases, the axial and equatorial isomers are similar in energy, but the bridging isomer's place in the energetic hierarchy varies substantially from metal to metal.

Table 4.1. Zero-point corrected relative isomer energies of monohydrated $[M(II)\cdot EDTA]^{2-}$ complexes (in meV).

Isomer	Mg	Ca	Sr	Ba
A	0	1	65	70
E	2	0	59	53
B	79	4	0	0

For Mg, **A** and **E** are practically isoenergetic, while the bridging isomer is much higher in energy. For Ca, all three isomers are nearly isoenergetic. In Sr and Ba, the bridging isomer is lower in energy than the axial and equatorial isomers by ca. 50–70 meV. This trend is indicative of a relationship between the preferred water position and the size of the bound ion, and can be explained by the finding discussed above that larger ions are bound more closely to the opening of the binding pocket, which affords the water molecule greater access to the metal atom. Mg recedes far behind the equatorial carboxylate arms of the EDTA chelator, Ca comes closer to the rim of the pocket, Sr clears the axial carboxylate groups, and Ba is nearly coplanar with the equatorial ligands (see Figure 4.10). The more exposed the dication is, the more Coulomb interaction is possible between it and the electronegative O atom of the water molecule, which leads to the stabilization of the bridging isomer across the metal series.

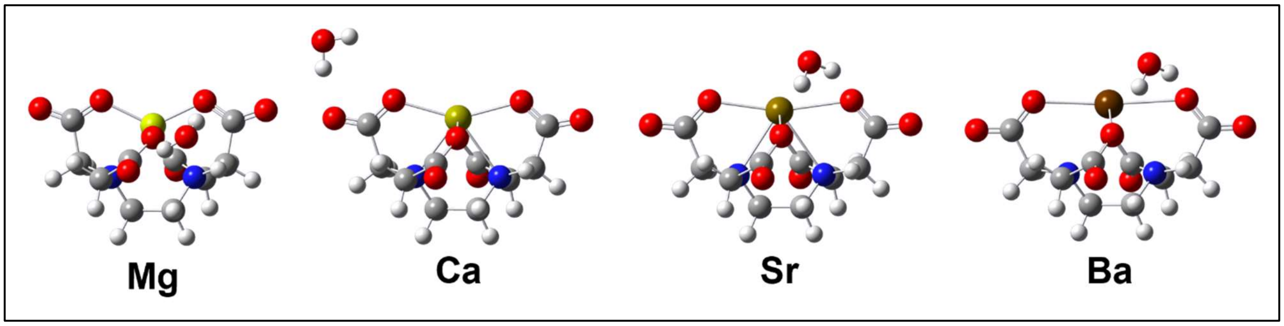

Figure 4.10. Lowest-energy isomer of each $[M(II)\cdot EDTA]^{2-}\cdot H_2O$ complex shown as equatorial slice.

The simulated spectra of the three monohydrate isomers produce good agreement between experiment and the lowest energy structures, as depicted in Figure 4.11. For Mg, not only do isomers **A** and **E** best capture the low energy shoulder at ca. 1627 cm^{-1}, but their calculated relative energies leads us to conclude that $[Mg(II)\cdot EDTA]^{2-}\cdot H_2O$ exists largely as an isomer mix of **A** and **E**. We assume that all three water binding motifs are present for $[Ca(II)\cdot EDTA]^{2-}\cdot H_2O$ based in part on their energies. Additionally, structures **A** and **E** produce virtually identical IR spectra which match the positions of the features in the experimental spectrum, but overrepresent the intensity of the low-frequency shoulder. As isomer **B** does not recover this feature, the combination of all three explains the lower intensity of the shoulder compared to that in Mg. The experimental spectra of Sr and Ba are only consistent with the bridging structural motif given that the other isomers predict moderate intensity peaks below the main feature that are not observed in the experiment. In combination with it being the lowest energy isomer in each case, we deduce that isomer **B** best represents $[M(II)\cdot EDTA]^{2-}\cdot H_2O$ for both M = Sr and Ba.

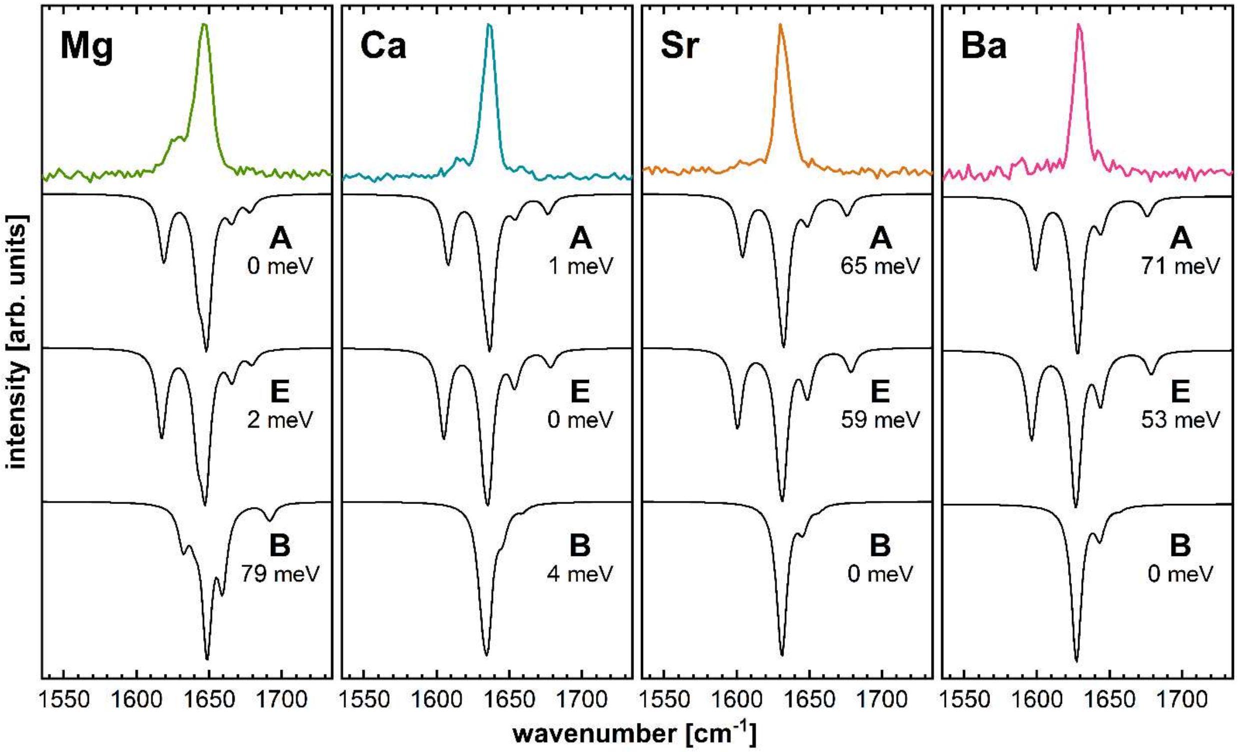

Figure 4.11. Experimental and calculated spectra for $[M(II)\cdot EDTA]^{2-}\cdot H_2O$ complexes. The identity of each metal is given in the upper left corner of each column. The experimental spectra are shown upright and in a color that varies with the identity of the metal ion, while the calculated spectra are shown inverted and in black. The calculated spectra are labeled with the hydration isomer (see Figure 4.9) and its relative energy (see Table 4.1).

In line with the calculated patterns of motion for the different ν_{as} modes, we assign the new low-frequency signatures in the Mg and Ca complexes' spectra as the antisymmetric O–C–O stretching vibrations of the hydrated carboxylate groups in the **A** and **E** isomers. The slight red shift from the mode's native position (within the peak **b** envelope in the bare ions) is rooted in small geometry changes induced by the water adduct. For both complexes, addition of a water molecule to the axial or equatorial arm shrinks the O–C–O bond angle of the H-bonded carboxylate by 0.7 – 0.9°. The H-bonding interaction also shortens the inner C–O bond and lengthens the outer, for a net effect of reducing the difference in length (Δb) between both bonds. In the non-hydrated species, Δb_{axial} = 2.8 pm (Mg), 3.0 pm (Ca) and $\Delta b_{equatorial}$ = 3.7 pm (Mg), 3.6 pm (Ca). For the monohydrates, the lengths of the C–O bonds in the H-bonded groups are more similar: Δb_{axial} = 1.5 pm and $\Delta b_{equatorial}$ =1.4 pm for both Mg and Ca complexes. These geometry changes — narrowing the O–C–O bond angle and equalizing the C–O distances — change the coupling between the affected C–O oscillators (see Chapter 6), which in turn changes the coupling between the local antisymmetric stretching oscillators of each carboxylate group, including their phase relations (Figure 4.12 for M = Ca, see Appendix B for other metals).

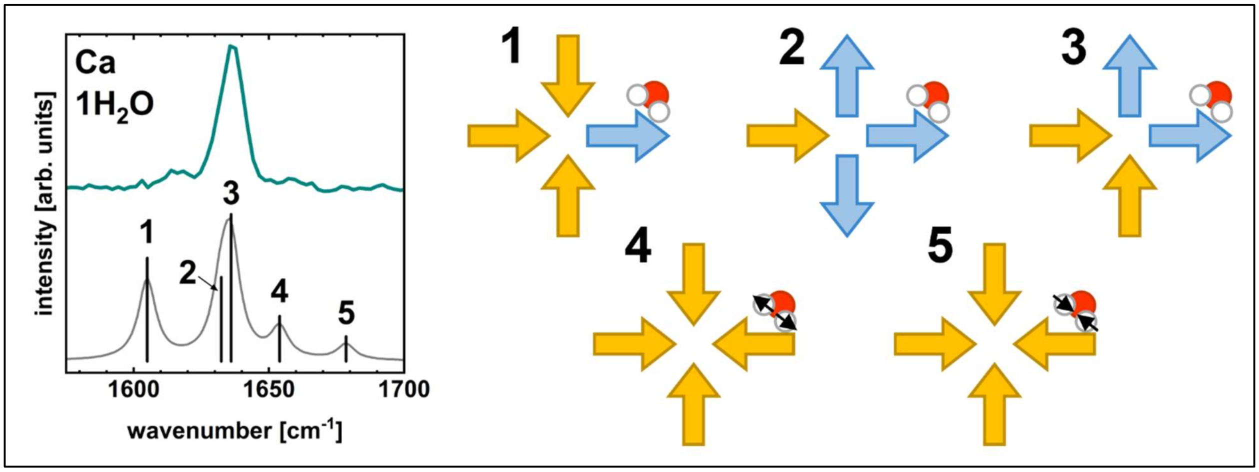

Figure 4.12. Antisymmetric O–C–O stretching modes of $[M(II)\cdot EDTA]^{2-}\cdot H_2O$ complexes using the M = Ca E isomer as an example. **Left:** Experimental and simulated spectra of M = Ca with individual ν_{as} transitions labelled to illustrate frequency ordering. **Right:** Patterns of motion for the antisymmetric O–C–O stretching modes as denoted on the left. Hydrated ligand marked with water molecule, phase relation of water bend shown with black arrows for modes with large amplitude of motion.

Furthermore, all ν_{as} modes undergo some degree of mode mixing with the water H–O–H bending vibration and they are no longer all evenly delocalized across the carboxylate groups. Isomers **A** and **E** both predict five transitions in the carboxylate antisymmetric stretching region for both Mg and Ca, and the mode assignment is analogous for all vibrations save for two exceptions in the Mg **A** calculation. The lowest frequency antisymmetric O–C–O stretching mode is now largely localized on the hydrated carboxylate group, which oscillates radially in phase with the opposing COO^- group in the axial Mg motif but out of phase with the other three ligands in the other cases. The most intense feature in the calculated spectra is comprised of two transitions. The lowest energy of the pair is mostly localized to the carboxylate group opposite the hydrated ligand, which experiences negligible amplitude of motion. The higher energy contribution is the second mode that differs for the axial isomer of the Mg complex, in which the hydrated carboxylate experiences no displacement whatsoever and the mode is localized to the equatorial arms and water bend. The non-hydrated axial ligand moves only slightly, oscillating in phase with the contraction of the water bend and one equatorial group but out of phase with the other. For Mg **E** and Ca **A**/**E**, the hydrated group is in phase with the contraction of the water bend and one neighboring arm, and out of phase with the remaining two ligands. The mode is localized to the set of arms (equatorial or axial) that is not hydrated and the water bend. Next higher in frequency is an unresolved mode on the blue edge of the most intense peak that consists of radially symmetric O–C–O antisymmetric stretching motion coupled with outward H–O–H bending. Finally, a weak mode is predicted that we do not observe experimentally. Its pattern of motion is akin to the mode before it, but with the water bend in the opposite phase, and is primarily localized to the water molecule.

The bridging isomer has its own set of vibrational modes (Figure 4.13 for M = Sr, see Appendix B for other metals), all of which are positioned at or above the most prominent peak in the spectra and so align well with the experimental data for $[M(II)\cdot EDTA]^{2-}\cdot H_2O$ with M = Sr and Ba. The absence of low-frequency features and relative stability of the bridging isomer leads us to conclude that it is the dominant binding motif of the singly hydrated Sr and Ba species.

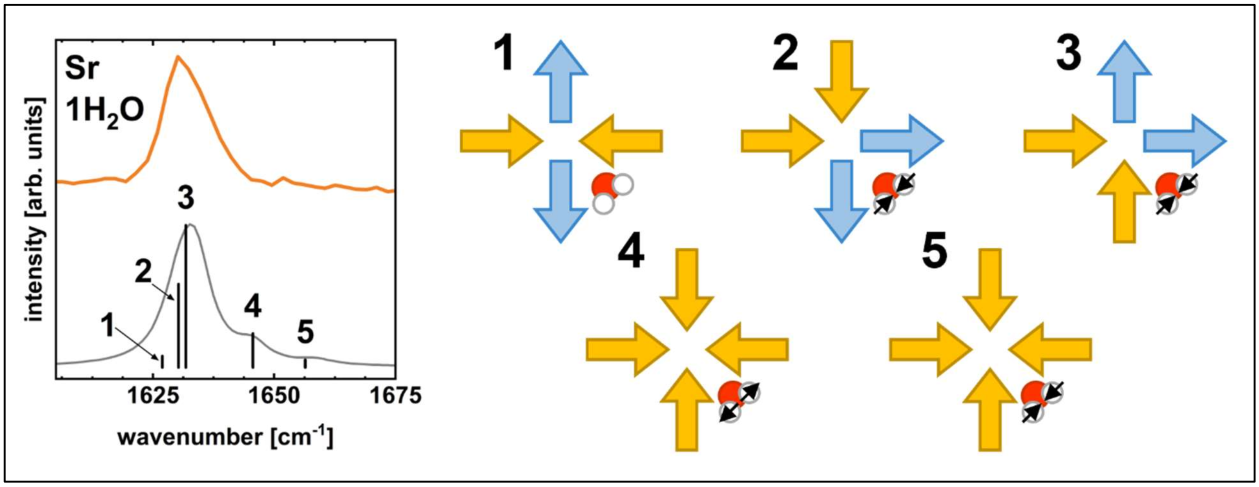

Figure 4.13. Antisymmetric O–C–O stretching modes of $[M(II)\cdot EDTA]^{2-}\cdot H_2O$ complexes using the M = Sr **B** isomer as an example. **Left:** Experimental and simulated spectra of M = Sr with individual ν_{as} transitions labelled to illustrate frequency ordering. **Right:** Patterns of motion for the antisymmetric O–C–O stretching modes as denoted on the left. Hydrated ligand marked with water molecule, phase relation of water bend shown with black arrows.

For isomer **B**, five transitions are predicted, consistent with the isomers discussed above, all of which undergo mode mixing with the H–O–H bend. The lowest three are within the envelope of the most intense feature, and the remaining two produce the blue shoulder of the main peak and a very weak high-frequency peak that we do not observe. The lowest of the five transitions couples the equatorial and axial ligands as in-phase pairs. The next higher mode is delocalized among all four COO^- groups and the water adduct. The carboxylate groups form two pairs of in-phase oscillators each consisting of the axial and equatorial arm that branch from opposite N atoms, and the pairs are out of phase with each other. Water bending motion is coupled to these oscillations. Higher in energy and intensity, the last mode comprising the main feature is similarly delocalized and is characterized by in-phase oscillation between arms connected to the same N atom moving in tandem with the water bend. The remaining two modes both consist of the radially symmetric O–C–O stretching mode in two linear combinations of opposite phase with the H–O–H bend.

b.3. Doubly Hydrated EDTA Complexes

The addition of a second water molecule to form $[M(II)\cdot EDTA]^{2-}\cdot(H_2O)_2$ complexes has a similar effect on the spectra as the first water adduct. We observe a weak blue shift, as noted above, and the low-energy shoulder of the main peak gains intensity and substructure, more so for M = Mg than M = Ca. Other than the slight change in peak position, no substantive changes occur as the M = Sr and Ba complexes accept a second solvent molecule.

Based on the analysis of the monohydrate data and calculations, we expect that the same metal-dependent water binding motifs continue for the dihydrate. Heightened relative intensity of the signatures on the low-energy side of the most intense feature indicates that the Mg complex will bind the second water in the fashion of isomers **A** and **E**. In the Ca spectrum, the new water adduct likely binds in a mixture of all three binding sites, but with a preference toward the **A** and **E** sites to account for the similar but less significant growth in low-energy features. There remains an absence of any peaks lower in energy than the most intense one in the Sr and Ba complexes, so it appears that the second water molecule is also binding in a bridging position.

This interpretation is supported by the calculations. Figure 4.14 shows the three lowest energy isomers of $[M(II)\cdot EDTA]^{2-}\cdot(H_2O)_2$ for M = Mg, Ca, Sr, and Ba (see Appendix B for higher energy structures). The Mg complex still holds the metal atom behind the carboxylate groups, preventing direct interaction with solvent molecules. The three lowest energy isomers are nearly isoenergetic, and the two most stable structures (Mg-AA and Mg-EE) depict the water molecule simply binding to the opposite arm from the first. The third isomer (Mg-AB_{ad}) forms a water dimer in which one of the water molecules binds to an axial ligand and the other forms H-bonds to the first water as well as the adjacent equatorial ligand. A higher energy structure which similarly contains a water dimer sub-cluster sees the bridge begin on an equatorial ligand and link over to an axial ligand.

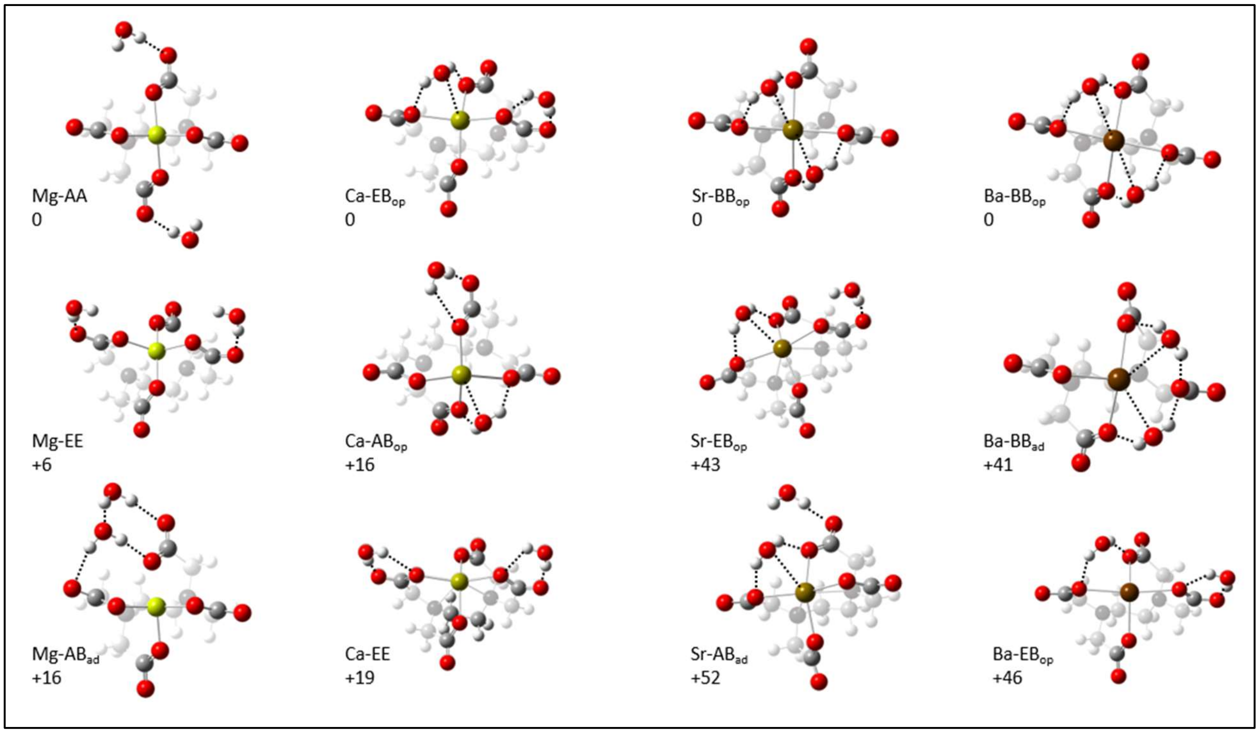

Figure 4.14. Calculated isomers with the lowest energies for each metal, with the carboxylate ligands, metal atoms, and water molecules highlighted. The labels include the metal and a description of the binding site for each water molecule as defined in Figure 4.9. Subscripts “op” and “ad” mean that the second water molecule binds to opposite or adjacent carboxylate ligands, respectively. Zero-point corrected energies are given for each structure. Metals are shown in yellow (Mg), dark yellow (Ca), brown (Sr) and dark brown (Ba); O = red; C = grey; H = light grey.

The lowest energy calculated isomers for the Ca complex are consistent with the hypothesis that there is an isomer mix with a preference toward **A**- and **E**-type water additions. The three most stable hydration motifs are still nearly isoenergetic, and now the two lowest energy structures also contain bridging water adducts which interact with one equatorial and axial arm through hydrogen bonds and with the metal center through Coulomb forces. As in the **B**-type isomers discussed for the monohydrates, the electrostatic interaction between the metal dication and O atom of the water stabilizes this configuration. Interestingly, if we assume that the $[Ca(II){\cdot}EDTA]^{2-}{\cdot}(H_2O)_2$ complex exists as an equal mix of the three lowest energy isomers (Ca-EB_{op}, Ca-AB_{op}, and Ca-EE), then we would see a 2:1 ratio of **A**/**E** type H-bonds to **B**-type H-bonds, as was anticipated above from the experimental spectra.

For the M = Sr and Ba complexes, the three lowest energy structures all contain at least one bridging water molecule, and in some cases, there are two (Sr-BB_{op}, Ba-BB_{op}, Ba-BB_{ad}). For both metals, the most stable isomer contains two bridging water adducts as a result of the ion being bound closer to the solvent layer than in the complexes of smaller alkaline earth metals. Additionally, the differences in energy between the three low energy isomers are greater in Sr and Ba, reducing the likelihood of an equal isomer mix.

Figure 4.15 compares experimental spectra of $[M(II){\cdot}EDTA]^{2-}{\cdot}(H_2O)_n$ (n = 0–2) with simulated spectrum of the isomer that best characterizes each complex and is lowest in energy. As the degree of hydration is increased, the Mg complex accommodates water adducts in primarily ligand-oriented positions, which generates substantial growth of the signatures on the low-energy side of the main feature. For the other metals, some population exists with water molecules bound with a bridging motif, which leads to the loss of intensity to the red of the dominant peak. This is the reason for the lower relative intensity in this region for Ca as compared to Mg — Ca retains some strength here due to its mix of **A**, **E**, and **B** binding geometries — and the absence of this feature for Sr and Ba whose population of H-bonds consist almost exclusively of bridging isomers.

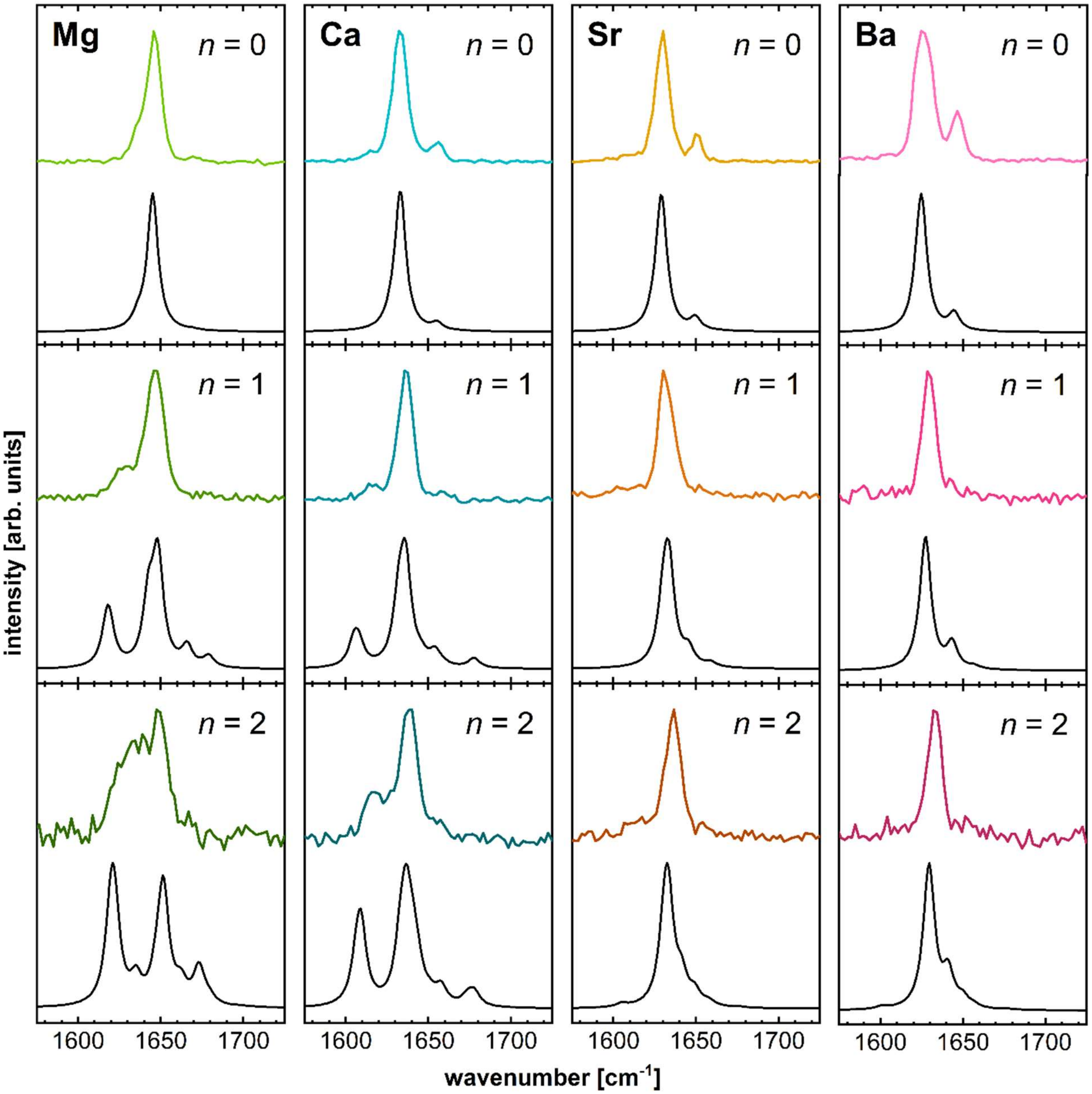

Figure 4.15. IR spectra of $[M(II)\cdot EDTA]^{2-}\cdot(H_2O)_n$ for n = 0, 1, and 2. Metal identity indicated at the top of each column, cluster size denoted in each panel. Upright, colored traces are experimental data; inverted, black traces are the Boltzmann-weighted sum of the calculated spectra for the isomers with relative energies of 46 meV or less (corresponding to isomers with at least 5% of the ground state population at 180 K). The calculated spectra are scaled to match the highest intensity feature of the corresponding experimental spectrum.

c. Transition Metal Complexes

Figure 4.16 shows the vibrational spectra for complexes of the form $[\mathrm{M(II)\text{-}EDTA}]^{2-}$ where M = Ca, Mn, Co, Ni, Cu, or Zn (the Ca spectrum is provided as a reference point).

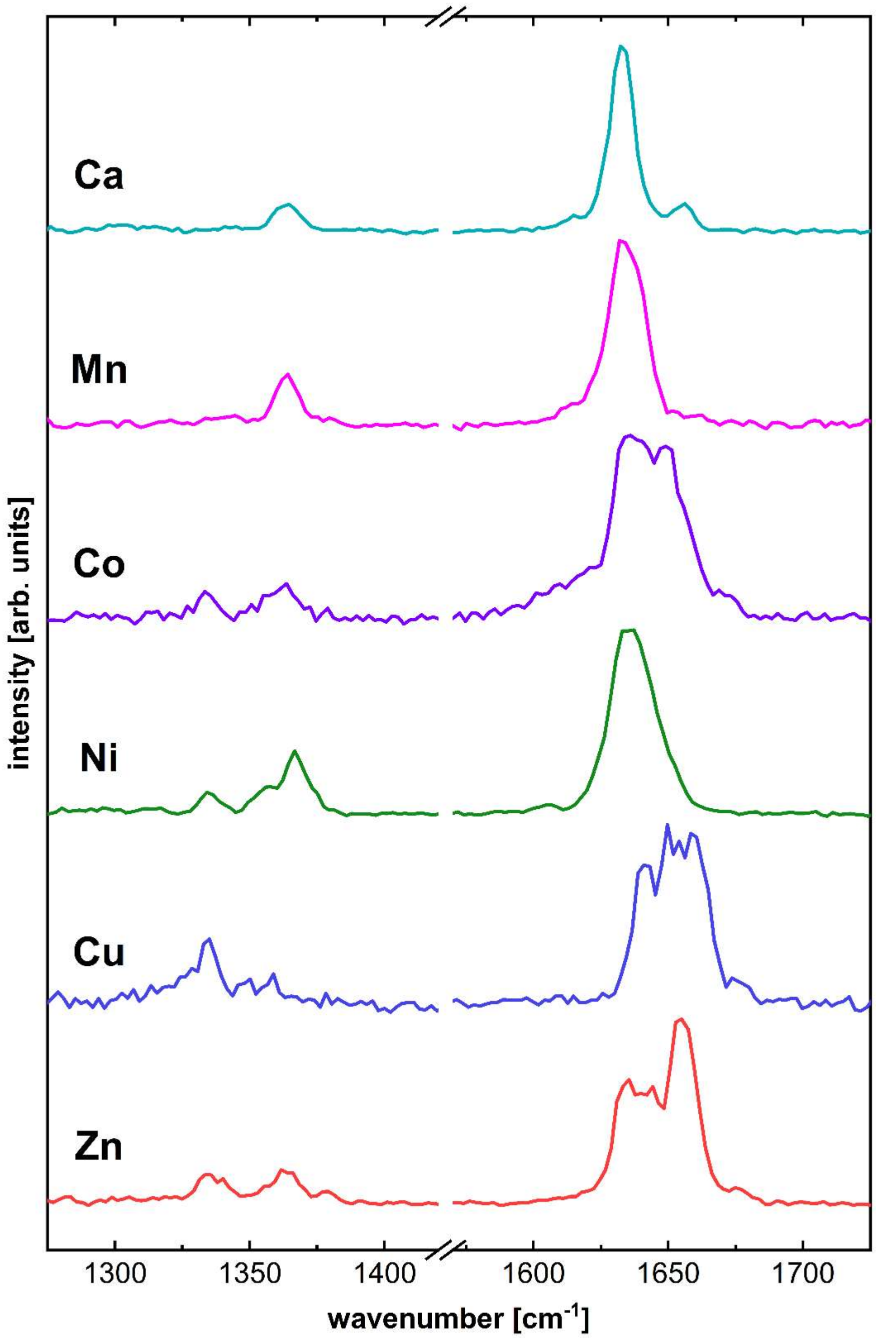

Figure 4.16. Experimental IR spectra of $[\mathrm{M(II)\text{-}EDTA}]^{2-}$ complexes. From top to bottom: M = Ca, Mn, Co, Ni, Cu, and Zn; metal identity given in each trace.

For EDTA–transition metal complexes, the observed features in both the symmetric and antisymmetric O–C–O stretching regions vary with the identity of the cation. In the cases of Mn and Ni, the high-frequency peak associated with the radially symmetric mode in the alkaline earth metals disappears entirely. In the M = Co, Cu, and Zn complexes, a significantly different substructure emerges in the ν_{as} band. Since these patterns depend on the interaction of the metal center with the carboxylate groups of the EDTA pocket, the electronic structure of the metal ions plays a key role in the spectroscopic properties. New sources of complexity emerge in these systems: (i) the bound ion does not exhibit spherically symmetric electron density; (ii) there is the possibility of different spin states; and (iii) the presence of isomers with coordination differing from the hexadentate structure of the EDTA complexes with alkaline earth metal ions.

For the Mn, Co, and Ni complexes, more than one spin state must be considered. Corroborating earlier results by Wang and co-workers, our DFT calculations predict that the high-spin states are the lowest in energy in each case (Table 4.2), and judging from natural orbital analysis, the unpaired electrons are localized on the metal center (Figure 4.17).

Table 4.2. Adiabatic energy gaps (in eV) of Mn(II) (sextet-quartet), Co(II) (quartet-doublet) and Ni(II) (triplet-singlet) compounds using B3LYP, B5050LYP, and ωB97X-D functionals with Def2-TZVPP basis set. High-spin states are lower in energy for all metal complexes under study and all functionals used here.

Metal	B3LYP	B5050LYP	ωB97X-D
Mn(II)	1.613	2.163	1.660
Co(II)	0.702	1.356	0.714
Ni(II)	0.804	1.739	0.929

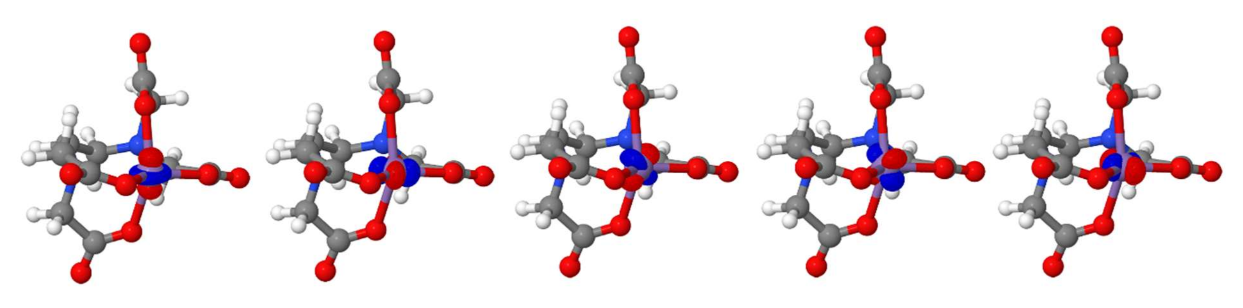

Figure 4.17. Frontier α orbitals of the lowest sextet state of [Mn(II)·EDTA]$^{2-}$, obtained from SF-B5050LYP calculations. Occupations of α and β orbitals are approximately 0.8 and 0.2, respectively.

The computed high-spin spectra match the experimental data quite well (Figure 4.18) for each complex. In the Mn complex, the symmetric stretching region is better recovered by the simulated spectrum of the sextet state, and the splitting of the modes predicted in the antisymmetric stretching region is smaller than the typical linewidth of the dominant signatures in this region. For the Ni complex, the predicted pattern of ν_{as} modes allows unambiguous assignment of the triplet state to the experimental spectrum. Both of these cases independently corroborate photoelectron spectroscopy and computational results assigning the high-spin states to [M(II)·EDTA]$^{2-}$ complexes. For M = Co, the infrared spectrum alone does not provide enough information to determine the spin state. However, we assume that the experimental spectrum belongs to the quartet state based on the relative energies of the different spin states, and we assign the substructure of the antisymmetric stretching feature to structural complexity (see below discussion of coordination geometry).

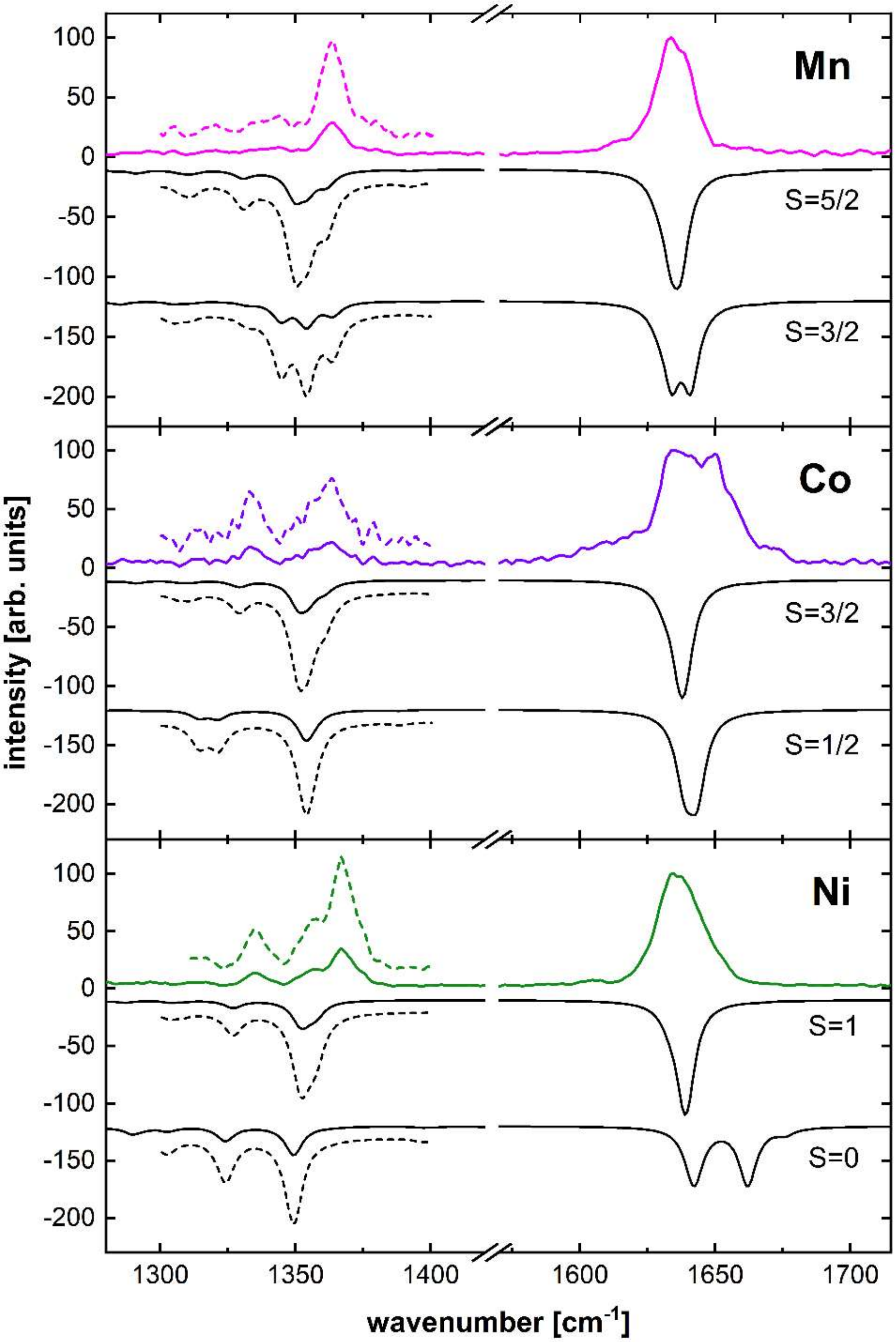

Figure 4.18. Experimental IR spectra of [M(II)-EDTA]$^{2-}$ complexes (from top to bottom: M = Mn, Co, and Ni; metal identity given in each panel; spin, S, shown for each calculated trace) in comparison with simulated spectra for hexacoordinated structures with different spin states. Dashed lines represent experimental and computed intensities multiplied by 3. The experimental spectra are shown in a color that varies with the identity of the metal ion, while the calculated spectra are shown in black. The intensities of the calculated spectra for high-spin complexes are scaled to fit the antisymmetric stretching region in each experimental spectrum. The relative intensities of low-spin and high-spin complexes are to scale.

The population of d-orbitals in the metal ion influences the orbital overlap between metal dication and chelator, causing structural differences to emerge across the different electronic structures of the metals under study. A particularly clear effect of the different d-orbital occupancies is the differences observed in the calculated distances of the metal ion to the inner carboxylate O atoms. The disparity in interaction strength causing in this structural distortion is reminiscent of a Jahn-Teller distortion in the local coordination geometry around the dication and is reflected in the ratio of the equatorial and axial metal–oxygen distances, d_{eq} and d_{ax}, respectively (see Figure 4.19).

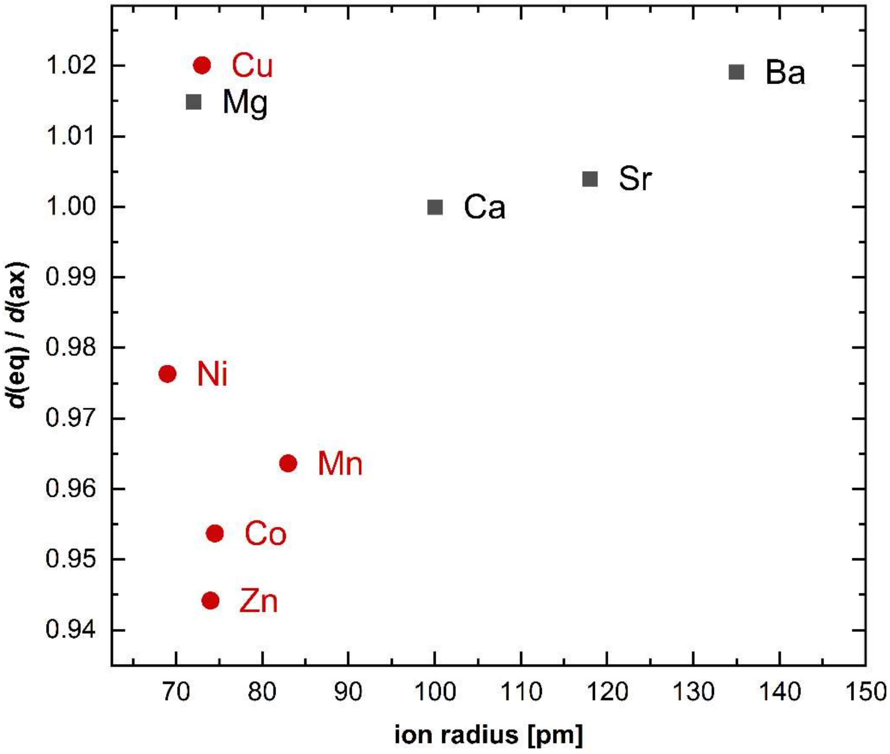

Figure 4.19. Calculated aspect ratio of equatorial to axial metal–oxygen bond distances as a function of ion radius for different divalent metal cations. Open squares show the data for alkaline earth metals, filled circles show data for transition metals.

For the alkaline earth metal complexes, the d_{eq}/d_{ax} ratio is centered around 1.01, with only small deviations (ca. 0.01), despite the drastic disparity in ion radius. Their spherical charge distribution about the metal center generates a spherically symmetric electric field with which the coordinating ligands interact, unlike the *d*-block elements studied in this work. The transition metal complexes exhibit a large range of d_{eq}/d_{ax} values that highlights the considerable difference in metal–ligand interactions with equatorial and axial ligands, despite their similar atomic radii (Figure 4.19). As a result, the kinematic coupling between the local O–C–O stretching oscillators with similar frequencies changes, and the participation of the individual carboxylate groups in each mode as well as the frequencies of each mode changes as well.

Within the hexacoordinated structures of $[M(II)\cdot EDTA]^{2-}$ complexes, the predicted overall pattern in the antisymmetric stretching region remains simple, with little structure within the realm of our experimental resolution. In contrast, the antisymmetric stretching region displays a complex set of features for M = Co, Cu, and Zn. Wang and co-workers proposed that the complexes for these metal ions could be penta- or even tetracoordinated rather than hexacoordinated (see Figure 4.20).

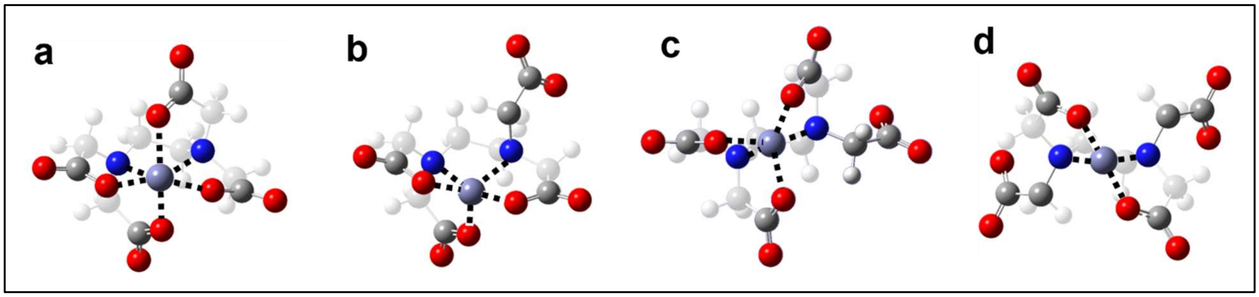

Figure 4.20. Structures of transition metal–EDTA complexes with varying coordination. (a–d) Calculated ball-and-bond-type structures of $[M(II)\cdot EDTA]^{2-}$ complexes in hexa- (a), penta- (b, c), and tetracoordinated (d) geometries using M = Zn as an example. Pentacoordinated structures can have an axial (c) or equatorial ligand (d) detached from the metal center. The metal environment in the tetracoordinated structures is approximately tetrahedral, making such distinctions less useful. Color scheme: H = white, C = gray, N = dark blue, O = red, Mn = blue-grey. Dotted lines show the coordination of the metal atom. The parts of the EDTA molecule that are not part of the binding pocket are shown in lighter gray tones.

Figure 4.21 shows the experimental IR spectra for M = Co, Cu, and Zn compared to the simulated IR spectra for different coordination isomers. The predicted infrared traces in the O–C–O antisymmetric stretching region blue-shift substantially for decreasing coordination numbers of the metal center.

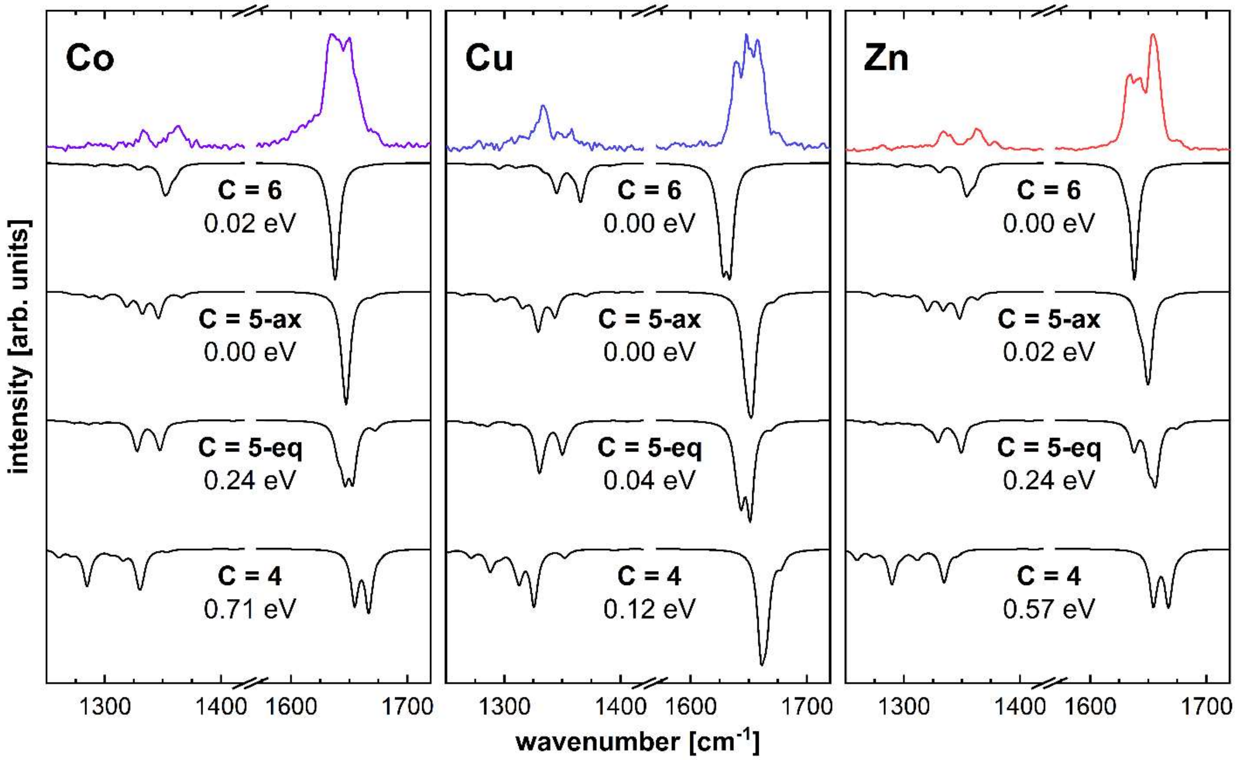

Figure 4.21. Experimental IR spectra of $[M(II)\text{-}EDTA]^{2-}$ complexes (from left to right: M = Co, Cu, and Zn; metal identity given in each panel; coordination number, C, shown for each calculated trace) in comparison with simulated spectra for different coordination numbers of the EDTA binding pocket (high-spin complexes only). The experimental spectra are shown in a color that varies with the identity of the metal ion, while the calculated spectra are shown in black. The intensities of the calculated spectra for hexacoordinated complexes are scaled to fit the antisymmetric stretching region in each experimental spectrum. The relative intensities for C = 4, 5, and 6 are to scale.

The work done by Wang et al. indicated that mostly hexacoordinated structures were represented by their photoelectron spectra of the M = Co, Cu, and Zn complexes. However, our calculations resulted in the penta- and hexacoordinated structures being virtually isoenergetic for each of these species (see Table 4.3). The differences between calculated energies are similar across both bodies of work, and we note that the spectra reported by Wang and colleagues could include some presence of pentacoordinated complexes given the degree of spectral congestion.

Table 4.3. Relative Energies (Zero Point-Corrected, in eV) of $[M(II)\cdot EDTA]^{2-}$ Isomers with Different Coordination Numbers

Coordination	Mn[a]	Co[a]	Ni[a]	Cu	Zn
6	0	0.02	0	0	0
5 (ax/eq)[b]	0.27 0.44	0 0.24	0.21 0.25	0 0.04	0.02 0.24
4	1.09	0.71	.64	0.12	0.57

[a] Only the high-spin state for each metal was used.
[b] The top number is for an axial ligand detached from the metal and the bottom for a detached equatorial ligand.

The calculated barriers between penta- and hexacoordinated isomers reported in [10] are ca. 1 eV for the cobalt and zinc complexes, and ca. 0.29 eV for the copper complex. Given the temperature of the ion trap during our experiment — 180 K — the probability of thermally occupying different isomers is negligible. However, it is worth noting that these complexes are first created and held at room temperature and in solution. In this regime, the thermal energy content of $[M(II)\cdot EDTA]^{2-}$ complexes is approximately 0.5 eV, and ions may undergo inelastic collisions in the first stages of the electrospray source that could imbue them with additional energy. Isomers generated through these means may be kinetically frozen via rapid cooling in the cryogenic ion trap. The solvation environment present during the electrospray process could also influence the relative stability of different isomers which, if formed, may possibly persist into the gas phase, but PCM calculations suggest that this potential route of generating an isomer mix is unlikely to occur. Calculations showed that the hexacoordinate geometry was the lowest in energy and that the computed gap between it and the penta- and tetracoordinated structures was in excess of ca. 200 meV, indicating that a significant population of the latter isomers would not exist in solution.

Based on these analyses, we conclude that the complex substructure in the antisymmetric stretching band of the M = Co, Cu, and Zn complexes is the result of coexisting hexa- and pentacoordinated isomers. For $[Zn(II)\cdot EDTA]^{2-}$, this conclusion is supported by work from Williams, Armentrout, and colleagues in which the Zn^{2+} ion was shown to preferentially adopt 5-fold coordination in hydrated cluster ions. [33,34] In the case of the Cu complex, both the equatorially and axially detached pentacoordinated structures are low enough in energy (see Table 4.3) to reasonably contribute to an isomer mix. Although the other metal centers generally had larger energetic barriers between these and the hexacoordinated structures, the potential energy landscapes are inevitably complex for the pentacoordinated geometries due to their conformational flexibility, and could in fact allow for the existence of additional structures not captured here.

Spectral evidence for the presence of pentacoordinated structures exists in the small shoulders at ca. 1675 cm^{-1} on the high-energy side of the antisymmetric OCO stretching region. These signatures are predicted as weak transitions in the simulated spectra of the pentacoordinated complexes but do not appear in those of the hexacoordinated structures. There exists the possibility that a very small population of tetracoordinated isomers could contribute to the spectrum of $[Cu(II)\cdot EDTA]^{2-}$, but we refrain from including them in our assignment based on their high relative energies for all other metals (see Table 4.3).

While the structural landscape of the Co, Cu, and Zn complexes gives rise to intricate spectral signatures, a simpler spectrum may not necessitate that a metal be exclusively hexacoordinated. For instance, even though the spectrum of [Ni(II)·EDTA]$^{2-}$ presents only one ν_{as} peak, this feature is sufficiently broad (full width at half-maximum, ca. 20 cm^{-1}) that it may encompass a minor contribution from the high-energy peak of the pentacoordinated structure with a detached axial COO$^-$ group (see Figure 4.22). The simulated vibrational spectrum of this isomer also captures portions of the pattern in the symmetric stretching region. In contrast, the analogous feature observed for [Mn(II)·EDTA]$^{2-}$ is unlikely to represent more than the hexacoordinated structure, as the other calculated spectra did not produce peaks within the envelope of the experimental band.

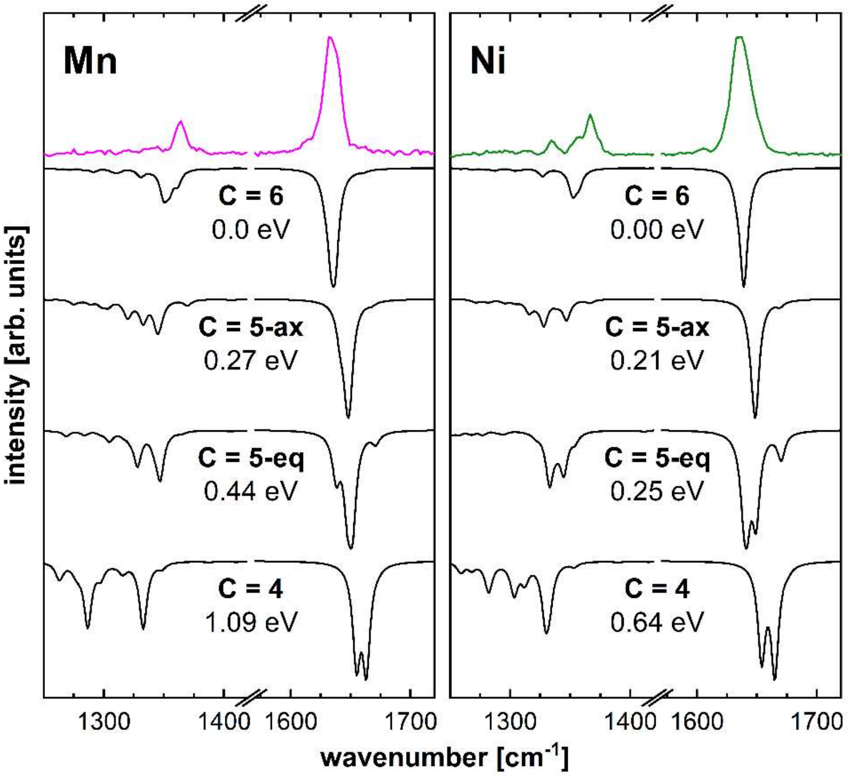

Figure 4.22. Experimental IR spectra of [M(II)-EDTA]$^{2-}$ complexes (from left to right: M = Mn, Ni; metal identity given in each panel; coordination number, C, shown for each calculated trace) in comparison with simulated spectra for different coordination numbers of the EDTA binding pocket (high-spin complexes only). The experimental spectra are shown in a color that varies with the identity of the metal ion, while the calculated spectra are shown in black. The intensities of the calculated spectra for hexacoordinated complexes are scaled to fit the antisymmetric stretching region in each experimental spectrum. The relative intensities for C = 4, 5, and 6 are to scale.

While the density of features in the region of the antisymmetric O–C–O stretching modes precludes a quantitative assignment of each isomer's relative population, the intensity variation allows us a qualitative assessment based on the blue shift of the ν_{as} modes with decreasing coordination. For $[Co(II)\cdot EDTA]^{2-}$, the roughly equal intensity distribution in the lower and higher frequency features in this region suggests that hexa- and pentacoordinated structures have similar populations, while the ratio of penta- to hexacoordinated populations is higher for $[Cu(II)\cdot EDTA]^{2-}$ and higher still for $[Zn(II)\cdot EDTA]^{2-}$. This is not completely reflected by the calculated energy differences, but these differences are rather small, and Boltzmann-weighted populations do not accurately describe kinetic trapping in different parts of the potential energy landscape, which may be at play here.

Numerous interrelated factors have been discussed here to explain the spectral variation across metal centers, many of which are encoded in the calculated structures and energies: metal-specific Jahn−Teller-like distortions, charge transfer to the metal center, and electrostatic constraints of the chelating EDTA ligand. However, we refrain from speculating on a more detailed model for the observed presence or absence of pentacoordinated isomers in EDTA complexes beyond the calculated energies and qualitative assessment described herein.

IV. Conclusions

The IR spectra of alkaline earth dication complexes with EDTA ($[M(II)\cdot EDTA]^{2-}$; M = Mg, Ca, Sr, Ba) were used to illustrate that the ion's size determines the openness of the binding pocket and its position within the pocket, which governs its exposure to the chemical environment. Both factors are likely to influence the competition of ion binding and ion hydration, impacting the selectivity of a given ion receptor.

The comparison with stepwise hydration and solution data shows the impact of the solvation environment on the structural and binding characteristics of the binding pocket. The molecular nature of the hydrogen bonding interactions with the ion and the pocket depend on the ion size, with larger ions stabilizing hydration isomers in which the metal atom interacts with the water adduct. Full solvation pulls the bound ion closer to the rim of the binding pocket, increasing its exposure to the chemical surroundings.

Complexes of EDTA with transition metals (M = Mn, Co, Ni, Cu, Zn) were generally found to be in their highest possible spin states, which is an interesting observation, since EDTA has been variously characterized as a strong- or weak-field ligand. All metal atoms showed some proclivity to form hexacoordinated EDTA structures, and the complexes with Co, Cu, and Zn dications exhibited a substructure in the region of the antisymmetric O–C–O stretching modes that indicates the presence of additional coordination isomers, particularly with C = 5.

The electronic structure of the chelated ions affects the contribution of each carboxylate group to the O–C–O stretching motions in each mode and therefore influences the corresponding IR signatures. The non-hydrated alkaline earth metal complexes have evenly delocalized O–C–O antisymmetric stretching modes across all four carboxylates, while the hydrated and transition metal complexes showed varying distributions of displacement for different modes and COO^- groups.

These results highlight the variability of EDTA in accommodating ions of different sizes and show how the size and electronic structure of the guest atom impose a shape template in the interaction with the EDTA binding pocket that informs both exposure to and interaction with a solvent environment.

V. References

(1) Ghosh, A.; Greenberg, M. E. Calcium Signaling in Neurons: Molecular Mechanisms and Cellular Consequences. *Science* **1995**, *268*, 239–247.

(2) Bers, D. M. Calcium Cycling and Signaling in Cardiac Myocytes. *Annu. Rev. Physiol*. **2008**, *70*, 23–49.

(3) Tang, L.; Gamal El-Din, T. M.; Payandeh, J.; Martinez, G. Q.; Heard, T. M.; Scheuer, T.; Zheng, N.; Catterall, W. A. Structural Basis for Ca2+ Selectivity of a Voltage-Gated Calcium Channel. *Nature* **2014**, *505*, 56–61.

(4) Harrington, J. M.; Boyd, W. A.; Smith, M. V.; Rice, J. R.; Freedman, J. H.; Crumbliss, A. L. Amelioration of Metal-Induced Toxicity in Caenorhabditis Elegans: Utility of Chelating Agents in the Bioremediation of Metals. *Toxicol. Sci.* **2012**, *129*, 49–56.

(5) Waters, S. E.; Robb, B. H.; Marshak, M. P. Effect of Chelation on Iron-Chromium Redox Flow Batteries. *ACS Energy Lett*. **2020**, *5*, 1758–1762.

(6) Burgess, D. R., National Institute of Standards and Technology. Critically Selected Stability Constants of Metal Complexes. Version 8.0 for Windows. https://data.nist.gov/od/id/mds2-2154, (accessed Aug 1, 2022).

(7) Wang, X. B.; Woo, H. K.; Wang, L. S. Vibrational Cooling in a Cold Ion Trap: Vibrationally Resolved Photoelectron Spectroscopy of Cold C60− Anions. *J. Chem. Phys*. **2005**, *123*, 051106.

(8) Yuan, Q. Q.; Cao, W. J.; Wang, X. B. Cryogenic and Temperature-Dependent Photoelectron Spectroscopy of Metal Complexes. *Int. Rev. Phys. Chem*. **2020**, *39*, 83–108.

(9) Yuan, Q. Q.; Kong, X. T.; Hou, G. L.; Jiang, L.; Wang, X. B. Photoelectron Spectroscopic and Computational Studies of EDTA M(III)− Complexes (M = H3, Al, Sc, V-Co). *Phys. Chem. Chem. Phys.* **2018**, *20*, 19458–19469.

(10) Yuan, Q. Q.; Kong, X. T.; Hou, G. L.; Jiang, L.; Wang, X. B. Electrospray Ionization Photoelectron Spectroscopy of Cryogenic EDTA·M(II)2- Complexes (M = Ca, V-Zn): Electronic Structures and Intrinsic Redox Properties. *Faraday Discuss.* **2019**, *217*, 383–395.

(11) Wang, X. B.; Woo, H. K.; Wang, L. S. Vibrational Cooling in a Cold Ion Trap: Vibrationally Resolved Photoelectron Spectroscopy of Cold C60− Anions. *J. Chem. Phys*. **2005**, *123*, 051106.

(12) Yuan, Q. Q.; Cao, W. J.; Wang, X. B. Cryogenic and Temperature-Dependent Photoelectron Spectroscopy of Metal Complexes. *Int. Rev. Phys. Chem*. **2020**, *39*, 83–108.

(13) (M10) Yuan, Q. Q.; Kong, X. T.; Hou, G. L.; Jiang, L.; Wang, X. B. Photoelectron Spectroscopic and Computational Studies of EDTA M(III)− Complexes (M = H3, Al, Sc, V-Co). *Phys. Chem. Chem. Phys.* **2018**, *20*, 19458–19469.

(14) (m11) Yuan, Q. Q.; Kong, X. T.; Hou, G. L.; Jiang, L.; Wang, X. B. Electrospray Ionization Photoelectron Spectroscopy of Cryogenic EDTA·M(II)2- Complexes (M = Ca, V-Zn): Electronic Structures and Intrinsic Redox Properties. *Faraday Discuss*. **2019**, *217*, 383–395.

(15) Gifford, J. L.; Walsh, M. P.; Vogel, H. J. Structures and MetalIon-Binding Properties of the Ca2+-Binding Helix-Loop-Helix EFHand Motifs. *Biochem. J.* **2007**, *405*, 199–221.

(16) (M9) Edington, S. C.; Gonzalez, A.; Middendorf, T. R.; Halling, D. B.; Aldrich, R. W.; Baiz, C. R. Coordination to Lanthanide Ions Distorts Binding Site Conformation in Calmodulin. *Proc. Natl. Acad. Sci. U. S. A.* **2018**, *115*, E3126–E3134.

(17) Escobar, L.; Ballester, P. Molecular Recognition in Water Using Macrocyclic Synthetic Receptors. *Chem. Rev*. **2021**, *121*, 2445–2514.

(18) Cremer, P. S.; Flood, A. H.; Gibb, B. C.; Mobley, D. L. Collaborative Routes to Clarifying the Murky Waters of Aqueous Supramolecular Chemistry. *Nat. Chem.* **2018**, *10*, 8–16.

(19) Becke, A. D.; Thermochemistry, D.-F. 3. The Role of Exact Exchange. *J. Chem. Phys*. **1993**, *98*, 5648–5652.

(20) Lee, C.; Yang, W.; Parr, R. G. Development of the ColleSalvetti Correlation-Energy Formula into a Functional of the Electron-Density. *Phys. Rev. B* **1988**, *37*, 785–789.

(21) Frisch, M. J.; Trucks, G. W.; Schlegel, H. B.; Scuseria, G. E.; Robb, M. A.; Cheeseman, J. R.; Scalmani, G.; Barone, V.; Petersson, G. A.; Nakatsuji, H., et al. Gaussian 16 Rev. C.01, Wallingford, CT, **2016**.

(22) Shao, Y.; Head-Gordon, M.; Krylov, A. I. The Spin-Flip Approach within Time-Dependent Density Functional Theory: Theory and Applications to Diradicals. *J. Chem. Phys*. **2003**, *118*, 4807–4818.

(23) Chai, J. D.; Head-Gordon, M. Long-Range Corrected Hybrid Density Functionals with Damped Atom-Atom Dispersion Corrections. *Phys. Chem. Chem. Phys*. **2008**, *10*, 6615–6620.

(24) Weigend, F.; Ahlrichs, R. Balanced Basis Sets of Split Valence, Triple Zeta Valence and Quadruple Zeta Valence Quality for H to Rn: Design and Assessment of Accuracy. *Phys. Chem. Chem. Phys*. **2005**, *7*, 3297–3305.

(25) Bernard, Y. A.; Shao, Y.; Krylov, A. I. General Formulation of Spin-Flip Time-Dependent Density Functional Theory Using NonCollinear Kernels: Theory, Implementation, and Benchmarks. *J. Chem. Phys*. **2012**, *136*, No. 204103.

(26) Wang, F.; Ziegler, T. Time-Dependent Density Functional Theory Based on a Noncollinear Formulation of the ExchangeCorrelation Potential. *J. Chem. Phys*. **2004**, *121*, 12191–12196.

(27) Miertus,ˇS.; Scrocco, E.; Tomasi, J. Electrostatic Interaction of a Solute with a Continuum. A Direct Utilizaion of Ab Initio Molecular Potentials for the Prevision of Solvent Effects. *Chem*. *Phys*. **1981**, *55*, 117–129.

(28) Lide, D. R. CRC Handbook of Chemistry and Physics, 86th ed.; Taylor & Francis Group: Boca Raton, FL, **2005**.

(29) NIST Mass Spectrometry Data Center, Wallace, W. E., "Infrared Spectra" in NIST Chemistry WebBook, NIST Standard Reference Database Number 69, Eds. P.J. Linstrom and W.G. Mallard, National Institute of Standards and Technology, Gaithersburg MD, 20899

(30) Godec, A., Smith, J. C., Merzel, F., Increase of both Order and Disorder in the First Hydration Shell with Increasing Solute Polarity. *Phys. Rev. Lett.* **2011** *107*, 267801

(31) Johnson, S. I., Baer, M. D., Raugei, S., Protonation of Serine in Gas and Condensed and Microsolvated States in Aqueous Solution. *J. Phys. Chem. A* **2022**, *126*, 1, 44–52

(32) Mitra, S., Denton, J. K., Kelleher, P. J., Johnson, M. A., Guasco, T. L., Choi, T. H., Jordan, K. D., Water Network Shape-Dependence of Local Interactions with the Microhydrated $-NO_2^-$ and $-CO_2^-$ Anionic Head Groups by Cold Ion Vibrational Spectroscopy. *J. Phys. Chem. A* **2022**, *126*, 16, 2471–2479

(33) Cooper, T. E., O'Brien, J. T., Williams, E. R., Armentrout, P. B. Zn2+ Has a Primary Hydration Sphere of Five: IR Action Spectroscopy and Theoretical Studies of Hydrated Zn2+ Complexes in the Gas Phase. *J. Phys. Chem. A* **2010**, 114, 12646-12655.

(34) O'Brien, J. T., Williams, E. R. Coordination Numbers of Hydrated Divalent Transition Metal Ions Investigated with IRPD Spectroscopy. *J. Phys. Chem. A* **2011**, 115, 14612-14619.

5. On the Bond Angle Dependance of Carboxylate Stretching Frequencies

I. Introduction

Carboxylato compounds, i.e., molecules of the form R–COO^{-}, are abundant across a huge array of chemical contexts. Their carboxylate functional groups often participate in the core functionality of a given molecule, e.g., as part of the binding pocket of a protein or by coordinating the metal center of a catalyst. [1–3] The vibrational signatures of the carboxylate groups — the symmetric (ν_s) and antisymmetric (ν_{as}) O–C–O stretching modes — are typically sharp and intense. In the case of the antisymmetric stretch, these peaks are typically in a region with low spectral congestion, making them easier to identify than many other features in the fingerprint region of the infrared spectrum. The positions of the carboxylate stretching signatures are sensitive to subtle changes in complex geometry and charge distribution, making them both challenging to interpret and desirable to model. [4,5] Here, we present a simple and generalizable relationship between the frequencies of the carboxylate stretching modes and the O–C–O bond angle (θ_{OCO}).

While quantum chemical calculations are quite useful for comparison between experimental and simulated infrared spectra in order to identify the most likely structure of a compound and assign infrared peaks, it is of fundamental interest to elucidate the structure–spectrum relationship of the individual carboxylate stretching modes. Moreover, identifying a simple relationship between the spectral and structural features of a carboxylate group makes for an easy assignment of these features in congested spectra, where even quantum chemical calculations may not allow a simple recognition of spectral patterns for peak identification.

II. Lay of the Land

A seemingly simple task at first glance, the search for an unambiguous correlation between the positions of the carboxylate bands and molecular geometry has spanned decades. Deacon and Phillips wrote an extensive, foundational review in 1980 which relates the symmetric and antisymmetric O–C–O stretching frequencies of carboxylato compounds (specifically, the splitting between them, $\Delta\nu_{\text{s-a}}$) with the coordination motif of the carboxylate group. [6] They classified carboxylates into unidentate, bidentate, bridging, and pseudo-bridging binding motifs, and found a rough empirical relationship between binding motif and $\Delta\nu_{\text{s-a}}$. This work was instrumental in establishing the influence of carboxylate coordination geometry on spectral signatures, and specifically identified both the length difference between connected C–O bonds and the O–C–O bond angle as the likely drivers of shifts in the carboxylate spectral features.

However, the authors noted many exceptions to the reported trends, and further explained that their observations did not generalize to multi-carboxylate systems, concluding their paper with the statement: "It is evident that factors affecting the separations between the carbon–oxygen stretching frequencies are more complex than differences between carbon-oxygen bond lengths or the size of the O–C–O angles alone." While this is a pioneering body of work, their necessary reliance on solution-phase and crystallographic data introduced spectral effects not solely dependent on intramolecular structure, obscuring the very relationships they were examining.

Sixteen years later, in 1996, Nara and colleagues took up the mantle and performed an investigation based on *ab initio* molecular orbitals of coordinated carboxylate groups and their stretching frequencies. [7] They produced the following relationship between the structure and peak splitting, $\Delta\nu_{\text{s-a}}$, of the carboxylate groups (in cm^{-1}):

$$\Delta\nu_{\mathrm{s-a}} = 1818.1\,\delta_r + 16.47(\theta_{OCO} - 120^\circ) + 66.8\ \mathrm{cm}^{-1}, \tag{1}$$

where δ_r is the difference between the two CO bond lengths (in Å) and θ_{OCO} is the O–C–O bond angle (in degrees). This result proposes a functional form for the two key structural influences on the carboxylate stretches highlighted by Deacon and Phillips — the C–O bond lengths and O–C–O angle — and the authors made a vital observation: the dependence of $\Delta\nu_{\text{s-a}}$ on the bond angle must have an angular offset. However, they employed a harmonic treatment of these modes over a limited range of O–C–O angles, which led them to linearize the more complicated relationship between $\Delta\nu_{\text{s-a}}$ and θ_{OCO}. Similar to a linear approximation in a Taylor series, this treatment does not yield the correct periodic behavior in θ_{OCO} — specifically for a bond angle approaching 180° — and in addition, the harmonic approximation is incompatible with experimental results. Overall, the predictive power of the model is therefore severely limited.

The next major development in pursuit of an elegant correlation between structural parameters of O–C–O type complexes and their spectral signatures came from Brinzer and colleagues in 2015. They reported a two-dimensional infrared spectroscopic study of CO_2 dissolved in a variety of ionic liquids. [8] In discussing their results, they posited that the stretching modes of the CO_2 molecules they observed could be described with a simple model of the vibrational Hamiltonian constructed in a vibrational local-mode basis:

$$\underline{\boldsymbol{H}} = \begin{pmatrix} \hbar\omega_1 & \beta \\ \beta & \hbar\omega_2 \end{pmatrix}, \tag{2}$$

where ω_i is the local mode frequency of C-O oscillator i, and β is the coupling between the two local modes. Extracting the eigenvalues of this matrix produces the symmetric and antisymmetric O–C–O stretching modes. The frequencies of these modes depend on the individual oscillator energies ($\hbar\omega_i$) which are related to the individual C–O bond lengths, and the coupling constant between the two local modes (β), a function of the O–C–O bond angle.

The authors then applied a linear fit to both of these parameters, generating equations that reproduce their experimental values quite well. This model is not generalizable to carboxylato complexes with significantly more acute O–C–O angles, owing to the limited dataset they are based on which consists of CO_2 molecules that remain largely linear across different solvent environments. This linearity not only prevents sampling the relationship between the positions of the CO_2 stretches and the O–C–O bond angle through a wide range of values, but also renders the symmetric stretch effectively IR inactive, preventing a more rigorous experimental benchmarking of this model. However, their local-mode approach to dissecting individual contributions to the carboxylate stretching energies is important, as it formulates a physical picture for the connection between the O–C–O stretching modes and molecular geometry.

In the present work, we describe the relation between the O–C–O bond angle and the splitting between positions of the symmetric and antisymmetric O–C–O stretches. The proposed model is quantitative, has concrete physical origins, is generalizable to a multitude of systems, and successfully describes existing data.

III. Results and Discussion

The local-mode approach used by Brinzer et al. describes the coupling of two local C–O oscillators to produce two molecular normal modes — the symmetric and antisymmetric stretches. [8] We begin with an analogous ansatz for the vibrational Hamiltonian:

$$\underline{\boldsymbol{H}} = h\begin{pmatrix} \nu_1 & \alpha \\ \alpha & \nu_2 \end{pmatrix} \tag{3}$$

Here, $h\nu_1$ and $h\nu_2$ are the oscillator energies of the two individual CO oscillators, and $h\alpha$ represents the coupling of the two oscillators. Diagonalizing the Hamiltonian and extracting the eigenvalues yields an expression for the normal mode energies, which can be expressed in the frequencies of the symmetric and antisymmetric stretching modes:

$$\nu_{\mathrm{as,s}} = \bar{\nu}_{1,2} \pm \frac{1}{2}\sqrt{4\alpha^2 + \Delta\nu_{1,2}{}^2} \tag{4}$$

In this description, $\bar{\nu}_{1,2}$ is the average of the two local oscillator frequencies, $\Delta\nu_{1,2}$ is their difference, and the antisymmetric and symmetric stretching modes result from the addition or subtraction of the second term, respectively. In the case of a symmetric carboxylato group, i.e., if the C–O bond lengths are equal and thereby the corresponding force constants and anharmonicities can be assumed to be the same, $\Delta\nu_{1,2}$ becomes 0. [9,10] In this regime, the expression for the splitting between the antisymmetric and the symmetric mode can be reduced as such:

$$\Delta\nu_{\mathrm{s-a}} = \nu_{\mathrm{as}} - \nu_{\mathrm{s}} = 2\left(\frac{1}{2}\sqrt{4\alpha^2 + \Delta\nu_{1,2}{}^2}\right) = 2\alpha, \tag{5}$$

resulting in a singular dependence on the coupling parameter α. In the case that $\alpha = 0$, the uncoupled C–O components would oscillate independently of one another. It has long been realized that the coupling between oscillators in carboxylato complexes is related to the O–C–O bond angle in some form or function. [6, 11-12] Although the exact relation may be more complex, we find that α can be expressed as a function only of θ_{OCO} with a remarkable degree of accuracy (discussed below). To quote Badger's remarks on his observation of the empirical relationship between the equilibrium bond length r_e and the force constant of the associated oscillator, "The fact that such a simple relation can be found is apparently due to the fact that the several factors on which r_e depends do not vary in an arbitrary and independent fashion through a set of molecules, but change in a more or less parallel manner." [9] In the present case, the many factors influencing α seem to vary together as well, allowing θ_{OCO} to serve as a descriptive parameter of the system as a whole.

Experimentally determined values of $\Delta\nu_{\mathrm{s-a}}$ were extracted from a series of gas-phase vibrational spectra of symmetric carboxylate complexes (see Appendix C for data set used in fit). [14-24] By plotting the observed values of $\Delta\nu_{s\text{-}a}$ against the O–C–O bond angle, as shown in Figure 5.1**,** we can extract an empirical relationship between the mode coupling constant α and θ_{OCO}.

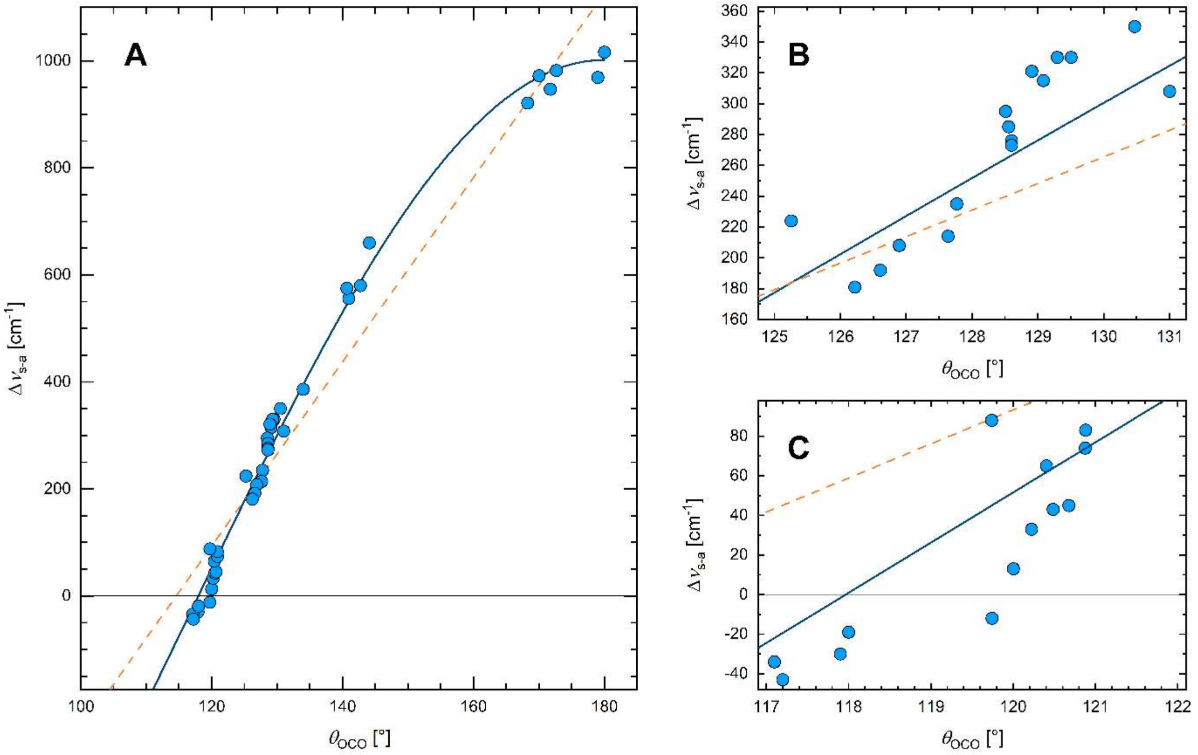

Figure 5.1. Blue circles represent experimental $\Delta\nu_{s\text{-}a}$ values of R–COO$^-$ type complexes (and CO_2) included in the fit, the full line is a cosine fit function (see text) up to θ_{OCO} = 180°, and the dashed orange line is a linear fit to the same data points. **A**: Experimental data and cosine fit function. **B**: Enlarged view of the cluster of points near θ_{OCO} = 130°. **C**: Enlarged view of points with $\Delta\nu_{s\text{-}a} < 0$.

Visually, the correlation between $\Delta\nu_{s\text{-}a}$ and θ_{OCO} suggests a trigonometric function that crosses the θ-axis just before 120° and reaches its maximum near 180°. Fitting with a cosine [eq. 6] produces an excellent match to the data and yields an R^2 value of 0.992, with residuals below 58 cm^{-1}. The seemingly periodic behavior of $\Delta\nu_{s\text{-}a}$ implies that the splitting is maximized when the O–C–O group approaches a linear geometry (θ_{OCO} = 180°) and minimized with a bent geometry (θ_{OCO} = 118°). The splitting between the symmetric and antisymmetric stretching modes in cm^{-1} is described by equation 6.

$$\Delta\tilde{\nu}_{\mathrm{s-a}} = 2\alpha = 1001.6\ \mathrm{cm}^{-1}\ cos(1.45\ \theta_{OCO} + 98.86°) \tag{6}$$

As θ_{OCO} varies, so too does the coupling constant α and, in turn, $\Delta\nu_{\text{s-a}}$. At ca. 120°, α approaches 0 cm^{-1}, so the uncoupled C–O bonds independently oscillate near their native frequencies (eq. 5). The opening of the bond angle to 180° brings about stronger interaction between the C–O local modes through the increasing coupling parameter and, therefore, concomitant growth in the symmetric-antisymmetric peak splitting.

We note that an overall linear fit to the data (see Figure 5.1) performs poorly. Even a linear fit limited to the range 116° ≤ θ_{OCO} ≤ 144° (representing a Taylor series expansion to the linear term) does not produce a more accurate prediction of $\Delta\nu_{\text{s-a}}$ than eq. 6.

The functional form of this relationship is consistent with normal mode analysis following Wilson's FG method. [12] This ansatz encodes the potential energy through the force constants of the molecule in terms of a given set of internal coordinates in a matrix $\underline{\boldsymbol{F}}$. It expresses the kinetic energy through a matrix $\underline{\boldsymbol{G}}$, which represents the motion of the atoms in the same internal coordinates and has dimensions of inverse mass. We represent the carboxylate group using a general model for a nonlinear triatomic. This model neglects the residue R in the R-COO$^-$ molecule, and we further simplify it by limiting our treatment to the CO stretching coordinates, resulting in the $\underline{\boldsymbol{F}}$ and $\underline{\boldsymbol{G}}$ being 2x2 matrices.

$$\underline{\boldsymbol{F}} = \begin{bmatrix} F_r, & F_{rr}' \\ F_{rr}', & F_r \end{bmatrix}; \underline{\boldsymbol{G}} = \begin{bmatrix} G_r, & G_{rr}' \\ G_{rr}', & G_r \end{bmatrix} \tag{7}$$

Multiplying them, we obtain the matrix:

$$\underline{\boldsymbol{F}}\,\underline{\boldsymbol{G}} = \begin{bmatrix} F_r G_r + F_{rr}' G_{rr}' & F_r G_{rr}' + F_{rr}' G_r \\ F_{rr}' G_r + F_r G_{rr}' & F_{rr}' G_{rr}' + F_r G_r \end{bmatrix} \tag{8}$$

Obtaining the eigenvalues of this matrix produces the eigenvalues $\lambda_{\pm}$

$$\lambda_{\pm} = F_r G_r + F_{rr}{}' G_{rr}' \pm 2(F_{rr}{}' G_r + F_r G_{rr}{}'), \tag{9}$$

which are equal to the squares of the normal mode energies, as given by:

$$\lambda_{\pm} = 4\pi^2\, \nu_{\mathrm{as,s}}{}^2 \tag{10}$$

If we use the normal coordinates (in the language of reference 12, a valence-type potential function without interaction terms), then the matrix $\underline{\boldsymbol{F}}$ becomes diagonal, and $F_{rr}' = 0$. Substituting the known G matrix values for this case [12], we obtain:

$$\lambda_{\pm} = F_r G_r \pm 2(F_r G_{rr}{}') = \; F_r(\mu_{\mathrm{C}} + \mu_{\mathrm{O}} \pm 2\, \mu_{\mathrm{C}}\, cos\theta_{OCO}) \tag{11}$$

where μ_x is the reciprocal mass of atom x. It is of note that, while μ_{O} is constant for all of the systems discussed in this text, the effect that μ_{C} has on the rest of the complex will vary with different carbon substituent groups, and we consider it an effective reciprocal mass. The splitting between eigenvalues is then given by:

$$\Delta\lambda_{\pm} = \; 4F_r \mu_{\mathrm{C}} cos\theta_{OCO} \tag{12}$$

Substituting eqs. 4 and 10 into eq. 12 gives an expression for the splitting between the symmetric and antisymmetric stretches as determined by normal mode analysis:

$$\Delta\nu_{\mathrm{s-a}} = \frac{F_r\, \mu_{\mathrm{C}}}{\pi^2 \bar{\nu}_{\mathrm{s,as}}}\, cos\theta_{OCO}, \tag{13}$$

where $\bar{\nu}_{s,as}$ is the average of the symmetric and antisymmetric O–C–O stretching frequencies.

Based on this relation, we should expect that $\Delta\nu_{\mathrm{s\text{-}a}}$ varies with the effective reciprocal mass of the carbon atom, the force constants of both local oscillators (reflected in both the F_r and $\bar{\nu}_{s,as}$ terms), and the cosine of the O–C–O bond angle. Our empirical model reflects this trigonometric dependence on the bond angle but includes a deviation of the period from 2π and an angular offset. We posit that these modifications serve to account for the simplicity of the model. A more realistic treatment of R-COO$^-$ would require including stretching as well as bending coordinates in a planar tetra-atomic system. We judge that for the purpose of the present work, a simple empirical relationship that captures most of the relevant physics is preferable over a more accurate, but also more complicated description.

Following the logic of the discussion above, deviations from the predicted curve can be attributed to three main factors: i) differences in the effective reciprocal mass of the carbon atom, ii) differences in local C–O oscillator force constants, and iii) different quality of the fit in different regions of θ due to the sparseness of available data.

Both the mass of the R group and its interaction with the carbon atom contribute to the effective reciprocal mass of C. As μ_C increases, so does the predicted splitting. Similarly, the C–O bond strength varies throughout the complexes included in the fit, which is inversely proportional to the predicted splitting. Since the empirical fit does not account for these parameters, it corresponds to an average representation of the variations in effective μ_C and local oscillator energies, which appear to largely vary together. Additionally, the available data on carboxylate complexes that meets the inclusion criteria (gas phase, symmetric) is sparse in some regions of θ_{OCO}. Least-squares fitting favors areas with a higher density of data points, as minimizing the error in a more populous region of the fit will lower the overall error more than by optimizing sparser regions of the fit that contribute fewer residual values to the total. All of these factors contribute to the fit function underestimating $\Delta\nu_{s\text{-}a}$ for many of the complexes near $\theta_{OCO} = 130°$ and overestimating near $\theta_{OCO} = 0°$.

If infrared spectra of carboxylato compounds with varying O–C–O bond angles and inequivalent C-O bond lengths are being compared, it may be useful to predict the lower bound (in $\mathrm{cm^{-1}}$) of the splitting between the antisymmetric and symmetric stretching modes as a function of θ_{OCO}, and the following relation may be used to do so:

$$\Delta\tilde{\nu}_{\mathrm{s-a}} = 979.0\ \mathrm{cm}^{-1}\ cos(1.47\ \theta_{\mathrm{OCO}} + 95.08°) \tag{14}$$

A cosine fit function was applied to data points selected from the pool of values included in the fit shown in Figure 5.1. Points were chosen that lie on the "inner" side of the main fit. Figure 5.2 shows where the minimum fit curve lies in relation to the data and fit discussed above (Figure 5.1, eq 6).

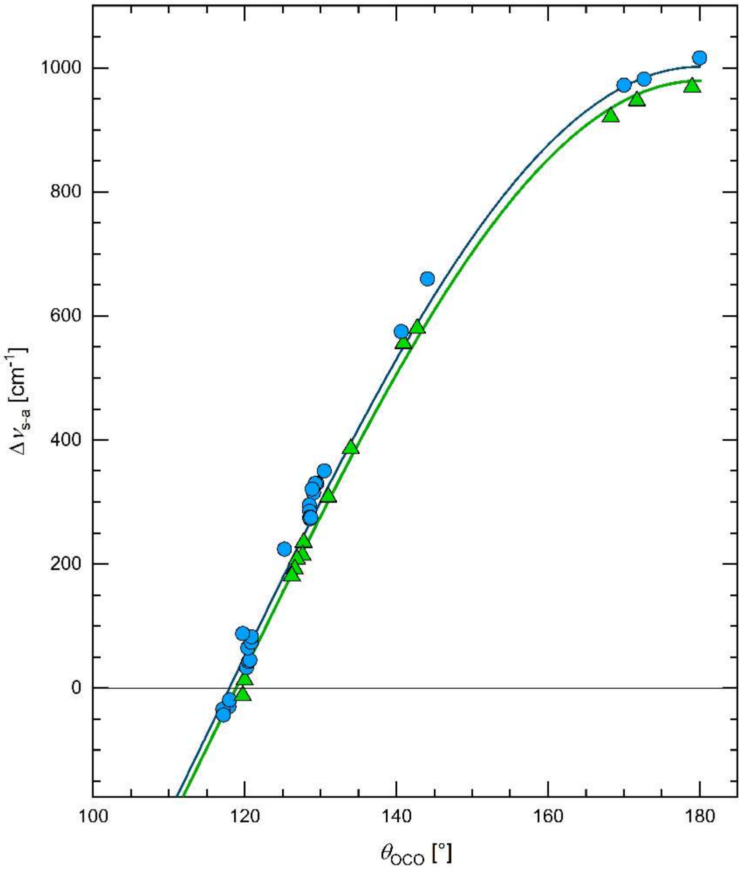

Figure 5.2. Blue circles represent experimental $\Delta\nu_{s\text{-}a}$ values of R-COO$^-$ type complexes included in the main fit; the full grey line is the corresponding cosine fit function (see Figure 5.1 and associated discussion). Green triangles represent values included in the lower bound fit, and the green line is the corresponding cosine fit function.

Figure 5.3 demonstrates the comparison to selected data points from Deacon and Phillips's work, with the inclusion criteria being that the compound is monocarboxylic and that both the symmetric and antisymmetric stretching modes were reported (and that only one frequency was reported per mode), as well as the calculated O–C–O bond angle and C–O bond lengths.

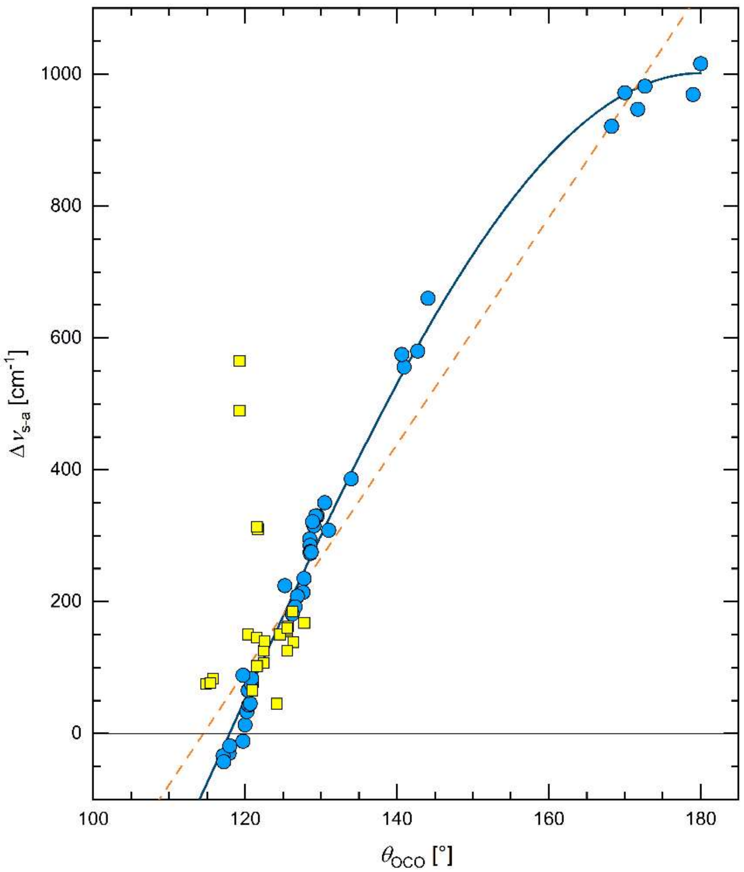

Figure 5.3. Yellow squares represent data from Deacon and Phillips's review. [2] Blue circles represent experimental $\Delta\nu_{s\text{-}a}$ values of R-COO$^-$ type complexes included in the fit, the full line is a cosine fit function (see Figure 5.1 and associated discussion), and the dashed orange line is a linear fit to the same data points.

The compounds with larger disparities between carboxylate C–O bond lengths deviate significantly from the predicted curve — the points with $\Delta\nu_{s\text{-}a}$ > 200 cm^{-1} have reported differences of more than 5 pm. Even though the data is crystallographic and many of the complexes are asymmetric, comparison of the empirical fit to experimental data from the original review by Deacon and Phillips yields a fairly good match.

IV. Conclusions

In summary, we have presented a straightforward model that quantifies the splitting between the symmetric and antisymmetric stretching frequencies in carboxylato complexes as a function of the O–C–O bond angle alone [eq 6]. This relation is semi-empirically derived, using a vibrational local-mode mathematical framework informed by several independent gas-phase measurements of R-COO$^-$ type compounds. Through normal mode analysis, the physical origins of the model are examined: O–C–O bond angle, C–O bond lengths, and the effective mass of the R-C segment. These structural parameters appear to serendipitously vary in tandem with one another, permitting the simplicity of our proposed model. The relation put forth here generalizes to a multitude of systems, and we anticipate that it may be used to further understand or predict experimental spectra of carboxylato compounds.

V. References

(1) Nara, M.; Morii, H.; Tanokura, M. Coordination to Divalent Cations by Calcium-Binding Proteins Studied by FTIR Spectroscopy. *Biochimica et Biophysica Acta (BBA) - Biomembranes* **2013**, *1828* (10), 2319–2327.

(2) Foreman, M. M.; Hirsch, R. J.; Weber, J. M. Effects of Formate Binding to a BipyridineBased Cobalt-4N Complex. *J. Phys. Chem*. A **2021**, *125* (33), 7297–7302.

(3) Costentin, C.; Robert, M.; Savéant, J.-M. Catalysis of the Electrochemical Reduction of Carbon Dioxide. *Chem. Soc. Rev*. **2013**, *42* (6), 2423–2436.

(4) Mitra, S.; Werling, K.; Berquist, E. J.; Lambrecht, D. S.; Garrett-Roe, S. CH Mode Mixing Determines the Band Shape of the Carboxylate Symmetric Stretch in Apo-EDTA, Ca 2+ –EDTA, and Mg 2+ –EDTA. *J. Phys. Chem. A* **2021**, *125* (22), 4867–4881.

(5) Brewer, E. I.; Green, A. E.; Gentleman, A. S.; Beardsmore, P. W.; Pearcy, P. A. J.; Meizyte, G.; Pickering, J.; Mackenzie, S. R. An Infrared Study of CO 2 Activation by Holmium Ions, Ho + and HoO +. *Phys. Chem. Chem. Phys*. **2022**, *24* (37), 22716–22723.

(6) Deacon, G. B.; Phillips, R. J. Relationships between the Carbon-Oxygen Stretching Frequencies of Carboxylato Complexes and the Type of Carboxylate Coordination. *Coordination Chemistry Reviews* **1980**, *33* (3), 227–250.

(7) Nara, M.; Torii, H.; Tasumi, M. Correlation between the Vibrational Frequencies of the Carboxylate Group and the Types of Its Coordination to a Metal Ion: An Ab Initio Molecular Orbital Study. *J. Phys. Chem*. **1996**, *100* (51), 19812–19817.

(8) Brinzer, T.; Berquist, E. J.; Dutta, S.; Johnson, C. A.; Krisher, C. S.; Lambrecht, D. S.; Garrett-Roe, S. Ultrafast Vibrational Spectroscopy (2D-IR) of CO 2 in Ionic Liquids: Carbon Capture from Carbon Dioxide's Point of View. *The Journal of Chemical Physics* **2015**, *142* (21), 212425.

(9) Badger, R. M. The Relation Between the Internuclear Distances and Force Constants of Molecules and Its Application to Polyatomic Molecules. *The Journal of Chemical Physics* **1935**, *3* (11), 710–714.

(10) Boyer, M. A.; Marsalek, O.; Heindel, J. P.; Markland, T. E.; McCoy, A. B.; Xantheas, S. S. Beyond Badger's Rule: The Origins and Generality of the Structure–Spectra Relationship of Aqueous Hydrogen Bonds. *J. Phys. Chem. Lett*. **2019**, *10* (5), 918–924.

(11) Dodson, L. G.; Thompson, M. C.; Weber, J. M. Characterization of Intermediate Oxidation States in CO 2 Activation. *Annu. Rev. Phys. Chem.* **2018**, *69* (1), 231–252.

(12) Wilson, E. B.; Decius, J. C.; Cross, P. C. Molecular Vibrations: The Theory of Infrared and Raman Vibrational Spectra; Dover Publications: New York, **1980**.

(13) Coblentz Society, Inc. Evaluated Infrared Reference Spectra. In NIST Chemistry WebBook, NIST Standard Reference Database Number 69; Linstrom, P. J., Mallard, W. G., Eds.; National Institute of Standards and Technology: Gaithersburg, MD, 20899.

(14) Gerardi, H. K.; DeBlase, A. F.; Su, X.; Jordan, K. D.; McCoy, A. B.; Johnson, M. A. Unraveling the Anomalous Solvatochromic Response of the Formate Ion Vibrational Spectrum: An Infrared, Ar-Tagging Study of the HCO 2 ⁻ , DCO 2 ⁻ , and HCO 2 ⁻ ·H 2 O Ions. *J. Phys. Chem. Lett*. **2011**, 2 (*19*), 2437–2441.

(15) Steill, J. D.; Oomens, J. Action Spectroscopy of Gas-Phase Carboxylate Anions by Multiple Photon IR Electron Detachment/Attachment. *J. Phys. Chem. A* **2009**, *113* (17), 4941–4946.

(16) DePalma, J. W.; Kelleher, P. J.; Tavares, L. C.; Johnson, M. A. Coordination-Dependent Spectroscopic Signatures of Divalent Metal Ion Binding to Carboxylate Head Groups: H 2 - and He-Tagged Vibrational Spectra of M 2+ ·RCO 2 ¯ (M = Mg and Ca, R = −CD 3 , −CD 2 CD 3) Complexes. *J. Phys. Chem. Lett.* **2017**, *8* (2), 484–488.

(17) Oomens, J.; Steill, J. D. Free Carboxylate Stretching Modes. *J. Phys. Chem. A* **2008**, *112* (15), 3281–3283.

(18) Thompson, M. C.; Ramsay, J.; Weber, J. M. Solvent-Driven Reductive Activation of CO2 by Bismuth: Switching from Metalloformate Complexes to Oxalate Products. *Angewandte Chemie International Edition* **2016**, *55* (48), 15171–15174.

(19) Knurr, B. J.; Weber, J. M. Solvent-Mediated Reduction of Carbon Dioxide in Anionic Complexes with Silver Atoms. *J. Phys. Chem. A* **2013**, *117* (41), 10764–10771.

(20) Denton, J. K.; Kelleher, P. J.; Johnson, M. A.; Baer, M. D.; Kathmann, S. M.; Mundy, C. J.; Wellen Rudd, B. A.; Allen, H. C.; Choi, T. H.; Jordan, K. D. Molecular-Level Origin of the Carboxylate Head Group Response to Divalent Metal Ion Complexation at the Air– Water Interface*. Proc. Natl. Acad. Sci. U.S.A.* **2019**, *116* (30), 14874–14880.

(21) Thompson, M. C.; Weber, J. M. Enhancement of Infrared Activity by Moving Electrons through Bonds – The Case of CO2 Anion and Carboxylate. *Chemical Physics Letters* **2017**, *683*, 586–590.

(22) Schneider, H.; Boese, A. D.; Weber, J. M. Infrared Spectra of O2−·(CO2)n Clusters (N=1– 6): Asymmetric Docking at the Π* Orbital. *The Journal of Chemical Physics* **2005**, *123* (7), 074316.

(23) Boese, A. D.; Schneider, H.; Glöß, A. N.; Weber, J. M. The Infrared Spectrum of Au−·CO2. *The Journal of Chemical Physics* **2005**, *122* (15), 154301.

Bibliography

Xu, S.; Gozem, S.; Krylov, A. I.; Christopher, C. R.; Mathias Weber, J., Ligand influence on the electronic spectra of monocationic copper–bipyridine complexes. *PCCP* **2015**, *17* (47), 31938-31946.

Wiley, W. C.; McLaren, I. H., Time-of-Flight Mass Spectrometer with Improved Resolution. *Review of Scientific Instruments* **1955**, *26* (12), 1150-1157.

Fenn, J. B.; Mann, M.; Meng, C. K.; Wong, S. F.; Whitehouse, C. M., Electrospray ionization for mass spectrometry of large biomolecules. *Science* **1989**, *246* (4926), 64.

Griffiths, J. A Brief History of Mass Spectrometry. *Anal. Chem.* **2008**, 80, 15, 5678–5683

Earnshaw, S., On the Nature of the Molecular Forces which Regulate the Constitution of the Luminiferous Ether. *Trans. Cambridge Philos. Soc.* **1847**, *7*, 97

Garand, E., Spectroscopy of Reactive Complexes and Solvated Clusters: A Bottom-Up Approach Using Cryogenic Ion Traps. *J. Phys. Chem. A* **2018**, *122*, 32, 6479–6490

Weber, J. M.; Robertson, W. H.; Johnson, M. A., Argon predissociation and electron autodetachment spectroscopy of size-selected CH3NO2−·Arn clusters. *The Journal of Chemical Physics* **2001**, *115* (23), 10718-10723.

Xu, S.; Smith, J. E. T.; Weber, J. M., The electronic spectrum of cryogenic ruthenium-tris-bipyridine dications in vacuo. *The Journal of Chemical Physics* **2016**, *145* (2), 024304.

Sampson, M. D., Froehclich, J. D., Smieja, J. M., Benson, Sharp, I. D., Kubiak, C. P., Direct observation of the reduction of carbon dioxide by rhenium bipyridine catalysts. *Energy Environ. Sci.*, **2013**, 6, 3748-3755

Benson, E. E., Kubiak, C. P., Sathrum, A. J., Smieja, J. M. Electrocatalytic and homogeneous approaches to conversion of CO2 to liquid fuels. *Chem. Soc. Rev.,* **2009**, *38*, 89-99

Costentin, C., Robert, M., Saveant, J-M., Catalysis of the electrochemical reduction of carbon dioxide. Chem. Soc. Rev., 2013,42, 2423-2436

Smieja, J. M., Kubiak C. P., Re(bipy-tBu)(CO)3Cl−improved Catalytic Activity for Reduction of Carbon Dioxide: IR-Spectroelectrochemical and Mechanistic Studies. Inorg. Chem. 2010, 49, 20, 9283–9289

Costentin, C., Drouet, S., Robert, M., Saveant, J-M., A Local Proton Source Enhances CO2 Electroreduction to CO by a Molecular Fe Catalyst. Science. 2012, 338, 6103, 90-94

Cosnier, S., Deronzier, A., Moutet, J-C., Electrocatalytic reduction of CO2 on electrodes modified by fac-Re(2,2'-bipyridine)(CO)3Cl complexes bonded to polypyrrole films. J. Mol. Catal. 1988, 45, 3, 380-391

Saveant, J.-M. Molecular Catalysis of Electrochemical Reactions. Mechanistic Aspects. Chem. Rev. 2008, 108, 2348−2378.

Manbeck, G. F.; Fujita, E. A Review of Iron and Cobalt Porphyrins, Phthalocyanines and Related Complexes for Electrochemical and Photochemical Reduction of Carbon Dioxide. J. Porphyrins Phthalocyanines 2015, 19, 45−64.

Lin, S.; Diercks, C. S.; Zhang, Y.-B.; Kornienko, N.; Nichols, E. M.; Zhao, Y.; Paris, A. R.; Kim, D.; Yang, P.; Yaghi, O. M.; et al. Covalent Organic Frameworks Comprising Cobalt Porphyrins for Catalytic CO2 Reduction in Water. Science 2015, 349, 1208−1213.

Beley, M.; Collin, J. P.; Ruppert, R.; Sauvage, J. P. Electrocatalytic Reduction of CO2 by Ni Cyclam2+ in Water: Study of the Factors Affecting the Efficiency and the Selectivity of the Process. J. Am. Chem. Soc. 1986, 108, 7461−7467.

Ogata, T.; Yanagida, S.; Brunschwig, B. S.; Fujita, E. Mechanistic and Kinetic Studies of Cobalt Macrocycles in a Photochemical CO2 Reduction System - Evidence of Co-CO2 Adducts as Intermediates. J. Am. Chem. Soc. 1995, 117, 6708−6716.

Hawecker, J.; Lehn, J. M.; Ziessel, R. Electrocatalytic Reduction of Carbon Dioxide Mediated by Re(Bipy)(CO)3Cl (Bipy = 2,2′- Bipyridine). J. Chem. Soc., Chem. Commun. 1984, 328−330.

Keith, J. A.; Grice, K. A.; Kubiak, C. P.; Carter, E. A. Elucidation of the Selectivity of Proton-Dependent Electrocatalytic CO2 Reduction by fac-Re(Bpy)(CO)3Cl. J. Am. Chem. Soc. 2013, 135, 15823−15829.

Takeda, H.; Koizumi, H.; Okamoto, K.; Ishitani, O. Photocatalytic CO2 Reduction Using a Mn Complex as a Catalyst. Chem. Commun. 2014, 50, 1491−1493.

Tanaka, K.; Ooyama, D. Multi-Electron Reduction of CO2 Via Ru-CO2, -C(O)OH, -CO, -CHO, and -CH2OH Species. Coord. Chem. Rev. 2002, 226, 211−218.

Hawecker, J., Lehn, J-M., Ziessel, R., Electrocatalytic Reduction of Carbon Dioxide Mediated by Re(bipy)(CO)3Cl (bipy = 2,2'-bipyridine) . J. Chem. Soc., Chem. Commun., 1984, 328-330

Shimoda, T.; Morishima, T.; Kodama, K.; Hirose, T.; Polyansky, D. E.; Manbeck, G. F.; Muckerman, J. T.; Fujita, E. Photocatalytic CO2 Reduction by Trigonal-Bipyramidal Cobalt(II) Polypyridyl Complexes: The Nature of Cobalt(I) and Cobalt(0) Complexes Upon Their Reactions with CO2, CO, or Proton. Inorg. Chem. 2018, 57, 5486−5498.

Bochlin, Y.; Korin, E.; Bettelheim, A. Different Pathways for CO2 Electrocatalytic Reduction by Confined CoTMPyP in Electrodeposited Reduced Graphene Oxide. ACS Appl. Energy Mater. 2019, 2, 8434−8440.

Dey, S.; Todorova, T. K.; Fontecave, M.; Mougel, V. Electroreduction of CO2 to Formate with Low Overpotential Using Cobalt Pyridine Thiolate Complexes. Angew. Chem., Int. Ed. 2020, 59, 15726−15733.

Becke, A. D. Density-Functional Thermochemistry 0.3. The Role of Exact Exchange. J. Chem. Phys. 1993, 98, 5648–5652.

Hay, P. J., Wadt, W. R., Ab initio effective core potentials for molecular calculations. Potentials for K to Au including the outermost core orbitals. J. Chem. Phys. 82, 299 (1985)

Frisch, M. J.; Trucks, G. W.; Schlegel, H. B.; Scuseria, G. E.; Robb, M. A.; Cheeseman, J. R.; Scalmani, G.; Barone, V.; Petersson, G. A.; Nakatsuji, H.; et al. Gaussian 16, Rev. C.01; Gaussian Inc.: Wallingford, CT, 2016.

Gerardi, H. K.; DeBlase, A. F.; Su, X.; Jordan, K. D.; McCoy, A. B.; Johnson, M. A. Unraveling the Anomalous Solvatochromic Response of the Formate Ion Vibrational Spectrum: An Infrared, Ar-Tagging Study of the HCO 2 ¯ , DCO 2 ¯ , and HCO 2 ¯ ·H 2 O Ions. J. Phys. Chem. Lett. 2011, 2 (19), 2437–2441.

Ghosh, A.; Greenberg, M. E. Calcium Signaling in Neurons: Molecular Mechanisms and Cellular Consequences. Science 1995, 268, 239–247.

Bers, D. M. Calcium Cycling and Signaling in Cardiac Myocytes. Annu. Rev. Physiol. 2008, 70, 23–49.

Tang, L.; Gamal El-Din, T. M.; Payandeh, J.; Martinez, G. Q.; Heard, T. M.; Scheuer, T.; Zheng, N.; Catterall, W. A. Structural Basis for Ca2+ Selectivity of a Voltage-Gated Calcium Channel. Nature 2014, 505, 56–61.

Harrington, J. M.; Boyd, W. A.; Smith, M. V.; Rice, J. R.; Freedman, J. H.; Crumbliss, A. L. Amelioration of Metal-Induced Toxicity in Caenorhabditis Elegans: Utility of Chelating Agents in the Bioremediation of Metals. Toxicol. Sci. 2012, 129, 49–56.

Waters, S. E.; Robb, B. H.; Marshak, M. P. Effect of Chelation on Iron-Chromium Redox Flow Batteries. ACS Energy Lett. 2020, 5, 1758–1762.

Burgess, D. R., National Institute of Standards and Technology. Critically Selected Stability Constants of Metal Complexes. Version 8.0 for Windows. https://data.nist.gov/od/id/mds2-2154, (accessed Aug 1, 2022).

Wang, X. B.; Woo, H. K.; Wang, L. S. Vibrational Cooling in a Cold Ion Trap: Vibrationally Resolved Photoelectron Spectroscopy of Cold C60− Anions. J. Chem. Phys. 2005, 123, 051106.

Yuan, Q. Q.; Cao, W. J.; Wang, X. B. Cryogenic and Temperature-Dependent Photoelectron Spectroscopy of Metal Complexes. Int. Rev. Phys. Chem. 2020, 39, 83–108.

Yuan, Q. Q.; Kong, X. T.; Hou, G. L.; Jiang, L.; Wang, X. B. Photoelectron Spectroscopic and Computational Studies of EDTA M(III)− Complexes (M = H3, Al, Sc, V-Co). Phys. Chem. Chem. Phys. 2018, 20, 19458–19469.

Yuan, Q. Q.; Kong, X. T.; Hou, G. L.; Jiang, L.; Wang, X. B. Electrospray Ionization Photoelectron Spectroscopy of Cryogenic EDTA·M(II)2- Complexes (M = Ca, V-Zn): Electronic Structures and Intrinsic Redox Properties. Faraday Discuss. 2019, 217, 383–395.

Wang, X. B.; Woo, H. K.; Wang, L. S. Vibrational Cooling in a Cold Ion Trap: Vibrationally Resolved Photoelectron Spectroscopy of Cold C60− Anions. J. Chem. Phys. 2005, 123, 051106.

Yuan, Q. Q.; Cao, W. J.; Wang, X. B. Cryogenic and Temperature-Dependent Photoelectron Spectroscopy of Metal Complexes. Int. Rev. Phys. Chem. 2020, 39, 83–108.

(M10) Yuan, Q. Q.; Kong, X. T.; Hou, G. L.; Jiang, L.; Wang, X. B. Photoelectron Spectroscopic and Computational Studies of EDTA M(III)− Complexes (M = H3, Al, Sc, V-Co). Phys. Chem. Chem. Phys. 2018, 20, 19458–19469.

(m11) Yuan, Q. Q.; Kong, X. T.; Hou, G. L.; Jiang, L.; Wang, X. B. Electrospray Ionization Photoelectron Spectroscopy of Cryogenic EDTA·M(II)2- Complexes (M = Ca, V-Zn): Electronic Structures and Intrinsic Redox Properties. Faraday Discuss. 2019, 217, 383–395.

Gifford, J. L.; Walsh, M. P.; Vogel, H. J. Structures and MetalIon-Binding Properties of the Ca2+-Binding Helix-Loop-Helix EFHand Motifs. Biochem. J. 2007, 405, 199–221.

(M9) Edington, S. C.; Gonzalez, A.; Middendorf, T. R.; Halling, D. B.; Aldrich, R. W.; Baiz, C. R. Coordination to Lanthanide Ions Distorts Binding Site Conformation in Calmodulin. Proc. Natl. Acad. Sci. U. S. A. 2018, 115, E3126–E3134.

Escobar, L.; Ballester, P. Molecular Recognition in Water Using Macrocyclic Synthetic Receptors. Chem. Rev. 2021, 121, 2445–2514.

Cremer, P. S.; Flood, A. H.; Gibb, B. C.; Mobley, D. L. Collaborative Routes to Clarifying the Murky Waters of Aqueous Supramolecular Chemistry. Nat. Chem. 2018, 10, 8–16.

Becke, A. D.; Thermochemistry, D.-F. 3. The Role of Exact Exchange. J. Chem. Phys. 1993, 98, 5648–5652.

Lee, C.; Yang, W.; Parr, R. G. Development of the ColleSalvetti Correlation-Energy Formula into a Functional of the Electron-Density. Phys. Rev. B 1988, 37, 785–789.

Frisch, M. J.; Trucks, G. W.; Schlegel, H. B.; Scuseria, G. E.; Robb, M. A.; Cheeseman, J. R.; Scalmani, G.; Barone, V.; Petersson, G. A.; Nakatsuji, H., et al. Gaussian 16 Rev. C.01, Wallingford, CT, 2016.

Shao, Y.; Head-Gordon, M.; Krylov, A. I. The Spin-Flip Approach within Time-Dependent Density Functional Theory: Theory and Applications to Diradicals. J. Chem. Phys. 2003, 118, 4807–4818.

Chai, J. D.; Head-Gordon, M. Long-Range Corrected Hybrid Density Functionals with Damped Atom-Atom Dispersion Corrections. Phys. Chem. Chem. Phys. 2008, 10, 6615–6620.

Weigend, F.; Ahlrichs, R. Balanced Basis Sets of Split Valence, Triple Zeta Valence and Quadruple Zeta Valence Quality for H to Rn: Design and Assessment of Accuracy. Phys. Chem. Chem. Phys. 2005, 7, 3297−3305.

Bernard, Y. A.; Shao, Y.; Krylov, A. I. General Formulation of Spin-Flip Time-Dependent Density Functional Theory Using NonCollinear Kernels: Theory, Implementation, and Benchmarks. J. Chem. Phys. 2012, 136, No. 204103.

Wang, F.; Ziegler, T. Time-Dependent Density Functional Theory Based on a Noncollinear Formulation of the ExchangeCorrelation Potential. J. Chem. Phys. 2004, 121, 12191−12196.

Miertus,ˇS.; Scrocco, E.; Tomasi, J. Electrostatic Interaction of a Solute with a Continuum. A Direct Utilizaion of Ab Initio Molecular Potentials for the Prevision of Solvent Effects. Chem. Phys. 1981, 55, 117−129.

Lide, D. R. CRC Handbook of Chemistry and Physics, 86th ed.; Taylor & Francis Group: Boca Raton, FL, 2005.

NIST Mass Spectrometry Data Center, Wallace, W. E., "Infrared Spectra" in NIST Chemistry WebBook, NIST Standard Reference Database Number 69, Eds. P.J. Linstrom and W.G. Mallard, National Institute of Standards and Technology, Gaithersburg MD, 20899

Godec, A., Smith, J. C., Merzel, F., Increase of both Order and Disorder in the First Hydration Shell with Increasing Solute Polarity. Phys. Rev. Lett. 2011 107, 267801

Johnson, S. I., Baer, M. D., Raugei, S., Protonation of Serine in Gas and Condensed and Microsolvated States in Aqueous Solution. J. Phys. Chem. A 2022, 126, 1, 44–52

Mitra, S., Denton, J. K., Kelleher, P. J., Johnson, M. A., Guasco, T. L., Choi, T. H., Jordan, K. D., Water Network Shape-Dependence of Local Interactions with the Microhydrated −NO2− and −CO2− Anionic Head Groups by Cold Ion Vibrational Spectroscopy. J. Phys. Chem. A 2022, 126, 16, 2471–2479

Cooper, T. E., O'Brien, J. T., Williams, E. R., Armentrout, P. B. Zn2+ Has a Primary Hydration Sphere of Five: IR Action Spectroscopy and Theoretical Studies of Hydrated Zn2+ Complexes in the Gas Phase. J. Phys. Chem. A 2010, 114, 12646-12655.

O'Brien, J. T., Williams, E. R. Coordination Numbers of Hydrated Divalent Transition Metal Ions Investigated with IRPD Spectroscopy. J. Phys. Chem. A 2011, 115, 14612-14619.

Nara, M.; Morii, H.; Tanokura, M. Coordination to Divalent Cations by Calcium-Binding Proteins Studied by FTIR Spectroscopy. Biochimica et Biophysica Acta (BBA) - Biomembranes 2013, 1828 (10), 2319–2327.

Foreman, M. M.; Hirsch, R. J.; Weber, J. M. Effects of Formate Binding to a BipyridineBased Cobalt-4N Complex. J. Phys. Chem. A 2021, 125 (33), 7297–7302.

Costentin, C.; Robert, M.; Savéant, J.-M. Catalysis of the Electrochemical Reduction of Carbon Dioxide. Chem. Soc. Rev. 2013, 42 (6), 2423–2436.

Mitra, S.; Werling, K.; Berquist, E. J.; Lambrecht, D. S.; Garrett-Roe, S. CH Mode Mixing Determines the Band Shape of the Carboxylate Symmetric Stretch in Apo-EDTA, Ca 2+ –EDTA, and Mg 2+ –EDTA. J. Phys. Chem. A 2021, 125 (22), 4867–4881.

Brewer, E. I.; Green, A. E.; Gentleman, A. S.; Beardsmore, P. W.; Pearcy, P. A. J.; Meizyte, G.; Pickering, J.; Mackenzie, S. R. An Infrared Study of CO 2 Activation by Holmium Ions, Ho + and HoO +. Phys. Chem. Chem. Phys. 2022, 24 (37), 22716–22723.

Deacon, G. B.; Phillips, R. J. Relationships between the Carbon-Oxygen Stretching Frequencies of Carboxylato Complexes and the Type of Carboxylate Coordination. Coordination Chemistry Reviews 1980, 33 (3), 227–250.

Nara, M.; Torii, H.; Tasumi, M. Correlation between the Vibrational Frequencies of the Carboxylate Group and the Types of Its Coordination to a Metal Ion: An Ab Initio Molecular Orbital Study. J. Phys. Chem. 1996, 100 (51), 19812–19817.

Brinzer, T.; Berquist, E. J.; Dutta, S.; Johnson, C. A.; Krisher, C. S.; Lambrecht, D. S.; Garrett-Roe, S. Ultrafast Vibrational Spectroscopy (2D-IR) of CO 2 in Ionic Liquids: Carbon Capture from Carbon Dioxide's Point of View. The Journal of Chemical Physics 2015, 142 (21), 212425.

Badger, R. M. The Relation Between the Internuclear Distances and Force Constants of Molecules and Its Application to Polyatomic Molecules. The Journal of Chemical Physics 1935, 3 (11), 710–714.

Boyer, M. A.; Marsalek, O.; Heindel, J. P.; Markland, T. E.; McCoy, A. B.; Xantheas, S. S. Beyond Badger's Rule: The Origins and Generality of the Structure–Spectra Relationship of Aqueous Hydrogen Bonds. J. Phys. Chem. Lett. 2019, 10 (5), 918–924.

Dodson, L. G.; Thompson, M. C.; Weber, J. M. Characterization of Intermediate Oxidation States in CO 2 Activation. Annu. Rev. Phys. Chem. 2018, 69 (1), 231–252.

Wilson, E. B.; Decius, J. C.; Cross, P. C. Molecular Vibrations: The Theory of Infrared and Raman Vibrational Spectra; Dover Publications: New York, 1980.

Coblentz Society, Inc. Evaluated Infrared Reference Spectra. In NIST Chemistry WebBook, NIST Standard Reference Database Number 69; Linstrom, P. J., Mallard, W. G., Eds.; National Institute of Standards and Technology: Gaithersburg, MD, 20899.

Gerardi, H. K.; DeBlase, A. F.; Su, X.; Jordan, K. D.; McCoy, A. B.; Johnson, M. A. Unraveling the Anomalous Solvatochromic Response of the Formate Ion Vibrational Spectrum: An Infrared, Ar-Tagging Study of the HCO 2 ¯ , DCO 2 ¯ , and HCO 2 ¯ ·H 2 O Ions. J. Phys. Chem. Lett. 2011, 2 (19), 2437–2441.

Steill, J. D.; Oomens, J. Action Spectroscopy of Gas-Phase Carboxylate Anions by Multiple Photon IR Electron Detachment/Attachment. J. Phys. Chem. A 2009, 113 (17), 4941–4946.

DePalma, J. W.; Kelleher, P. J.; Tavares, L. C.; Johnson, M. A. Coordination-Dependent Spectroscopic Signatures of Divalent Metal Ion Binding to Carboxylate Head Groups: H 2 - and He-Tagged Vibrational Spectra of M 2+ ·RCO 2 ¯ (M = Mg and Ca, R = −CD 3 , −CD 2 CD 3) Complexes. J. Phys. Chem. Lett. 2017, 8 (2), 484–488.

Oomens, J.; Steill, J. D. Free Carboxylate Stretching Modes. J. Phys. Chem. A 2008, 112 (15), 3281–3283.

Thompson, M. C.; Ramsay, J.; Weber, J. M. Solvent-Driven Reductive Activation of CO2 by Bismuth: Switching from Metalloformate Complexes to Oxalate Products. Angewandte Chemie International Edition 2016, 55 (48), 15171–15174.

Knurr, B. J.; Weber, J. M. Solvent-Mediated Reduction of Carbon Dioxide in Anionic Complexes with Silver Atoms. J. Phys. Chem. A 2013, 117 (41), 10764–10771.

Denton, J. K.; Kelleher, P. J.; Johnson, M. A.; Baer, M. D.; Kathmann, S. M.; Mundy, C. J.; Wellen Rudd, B. A.; Allen, H. C.; Choi, T. H.; Jordan, K. D. Molecular-Level Origin of the Carboxylate Head Group Response to Divalent Metal Ion Complexation at the Air– Water Interface. Proc. Natl. Acad. Sci. U.S.A. 2019, 116 (30), 14874–14880.

Thompson, M. C.; Weber, J. M. Enhancement of Infrared Activity by Moving Electrons through Bonds – The Case of CO2 Anion and Carboxylate. Chemical Physics Letters 2017, 683, 586–590.

Schneider, H.; Boese, A. D.; Weber, J. M. Infrared Spectra of O2−·(CO2)n Clusters (N=1– 6): Asymmetric Docking at the Π* Orbital. The Journal of Chemical Physics 2005, 123 (7), 074316.

Boese, A. D.; Schneider, H.; Glöß, A. N.; Weber, J. M. The Infrared Spectrum of Au−·CO2. The Journal of Chemical Physics 2005, 122 (15), 154301.

Appendices

A. Supplementary Information for Chapter 3. Bipyridine

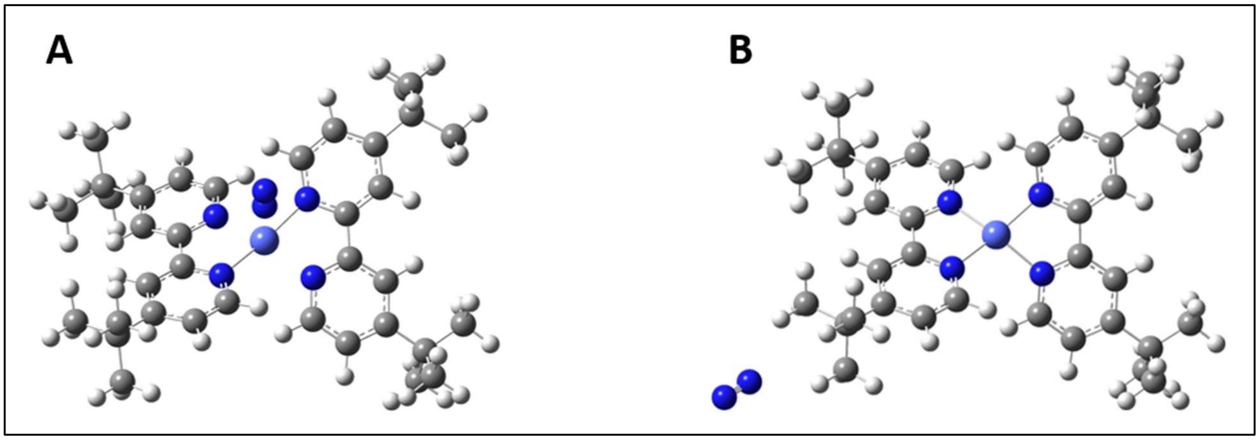

Figure A.1. Calculated structures of $[Co(DTBbpy)_2{\cdot}N_2]^{2+}$ (denoted in Chapter 3 as $[Co(DTBbpy)_2]^{2+}$ for clarity). **A:** N_2 tag binding to the metal center; **B:** N_2 tag attached to the tert-butyl group on one of the ligands. Atom colors: C = gray; H = white; N = dark blue; Co = light blue. Calculated energies show that the structure with N_2 binding to the metal center is 100 meV lower in energy, and resulting simulated infrared spectra are insensitive to the N_2 messenger tag position with calculated frequencies differing by <2 cm^{-1}. We therefore ignore the N_2 tag position in our analysis of the vibrational spectrum of $[Co(DTBbpy)_2]^{2+}$.

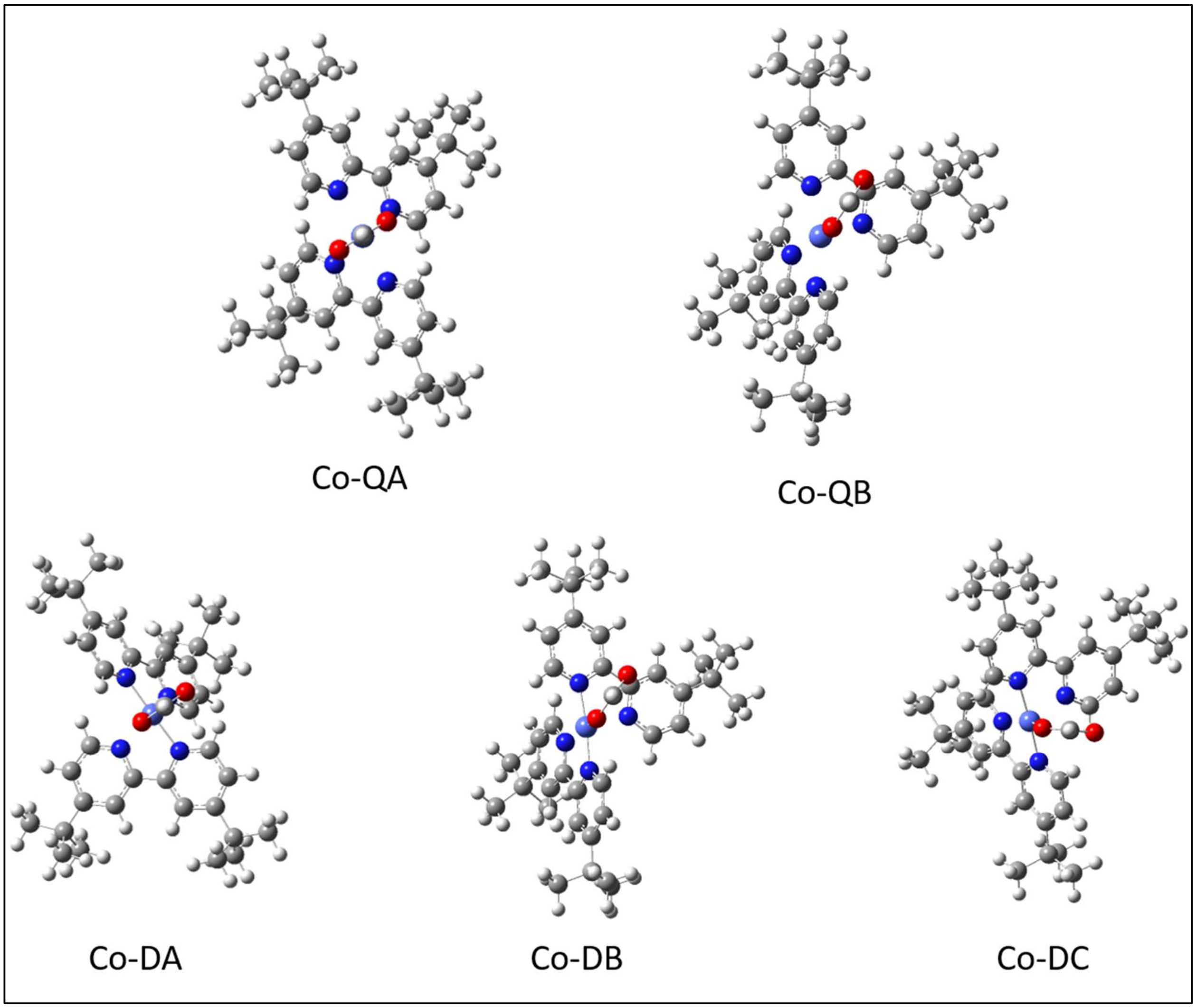

Figure A.2. Calculated structures of $[Co\cdot(bpy\text{-}tBu)_2\cdot HCOO]^+$ isomers. Structures viewed along the C–H bond axis of the formate ligand to highlight the orientation of the formate relative to the metal atom. Color scheme: H = white, C = gray, N = dark blue, Co = light blue, O = red.

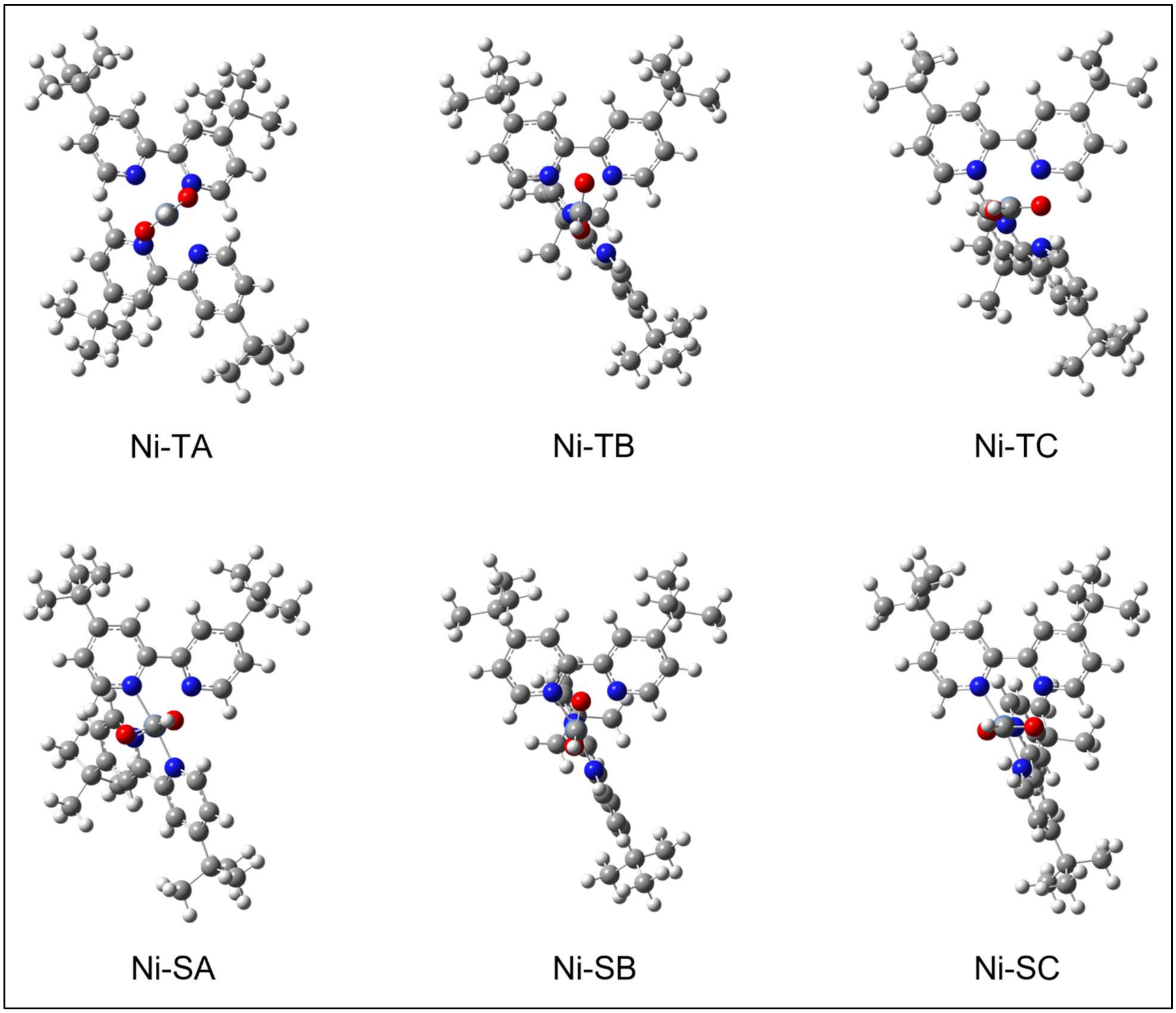

Figure A.3. Calculated structures of [Ni·(bpy-tBu)2·HCOO]+ isomers. Structures viewed along the C–Ni axis of the formate ligand to the metal to highlight the orientation of the formate relative to the metal atom. Color scheme: H = white, C = gray, N = dark blue, Ni = light blue, O = red.

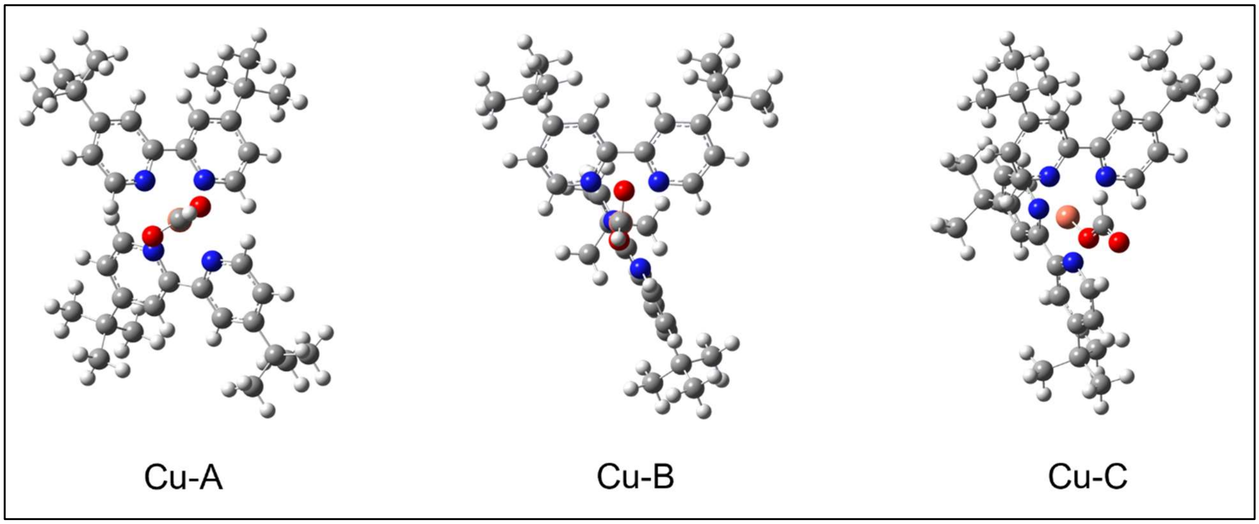

Figure A.4. Calculated structures of $[\mathrm{Cu}\cdot(\mathrm{bpy}\text{-}t\mathrm{Bu})_2\cdot\mathrm{HCOO}]^+$ isomers. Structures Cu-A and Cu-B viewed along the C–Cu axis of the formate ligand to the metal to highlight the orientation of the formate relative to the metal atom; structure Cu-C viewed offset to show O–Cu coordination of formate ligand. Color scheme: H = white, C = gray, N = dark blue, Cu = orange, O = red.

B. Supplementary Information for Chapter 4. EDTA

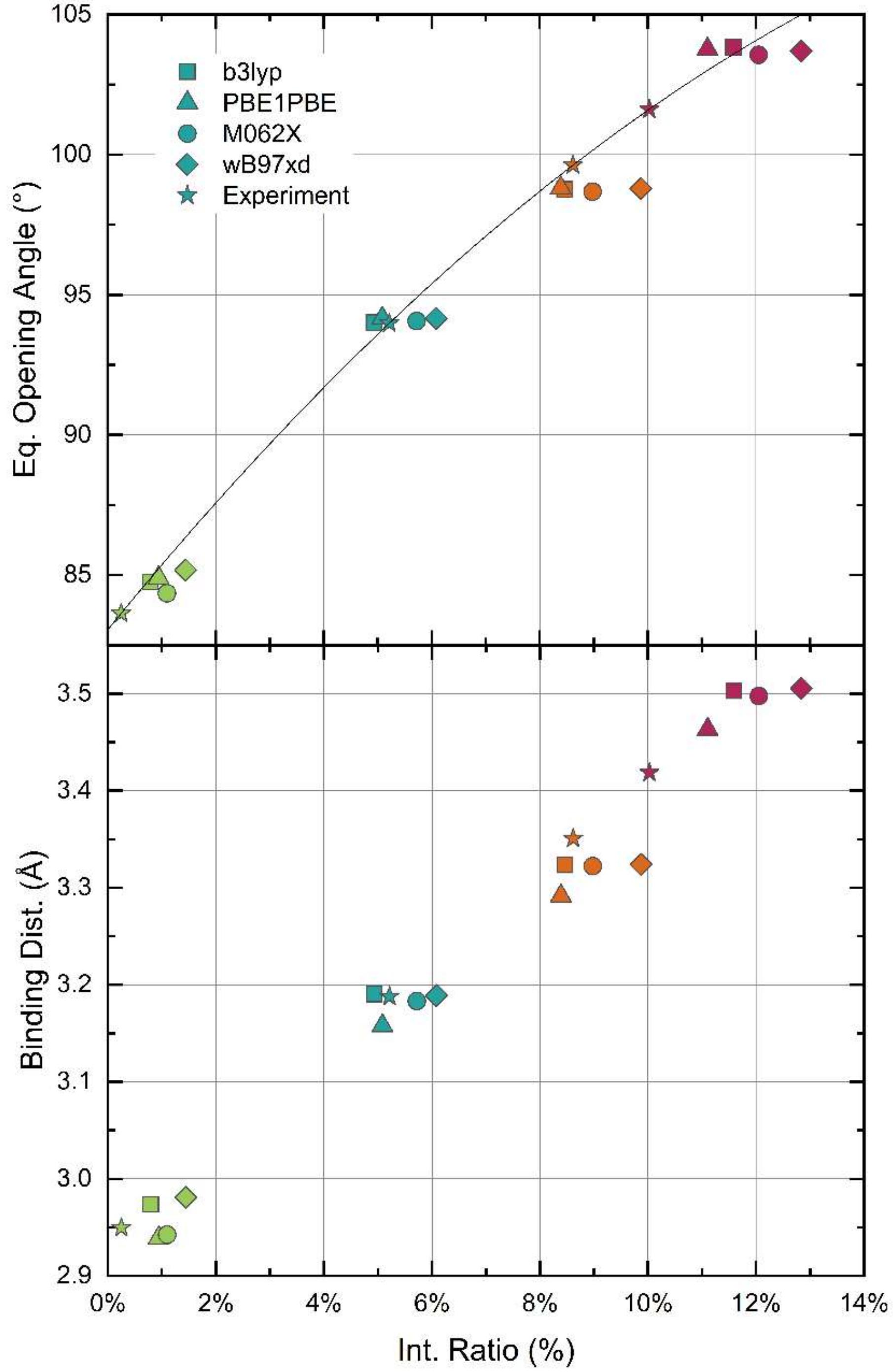

Figure B.1. Comparison of calculated geometry models from various functionals with experimental data. The fit function shown is generated by the calculated values from using the B3LYP functional.

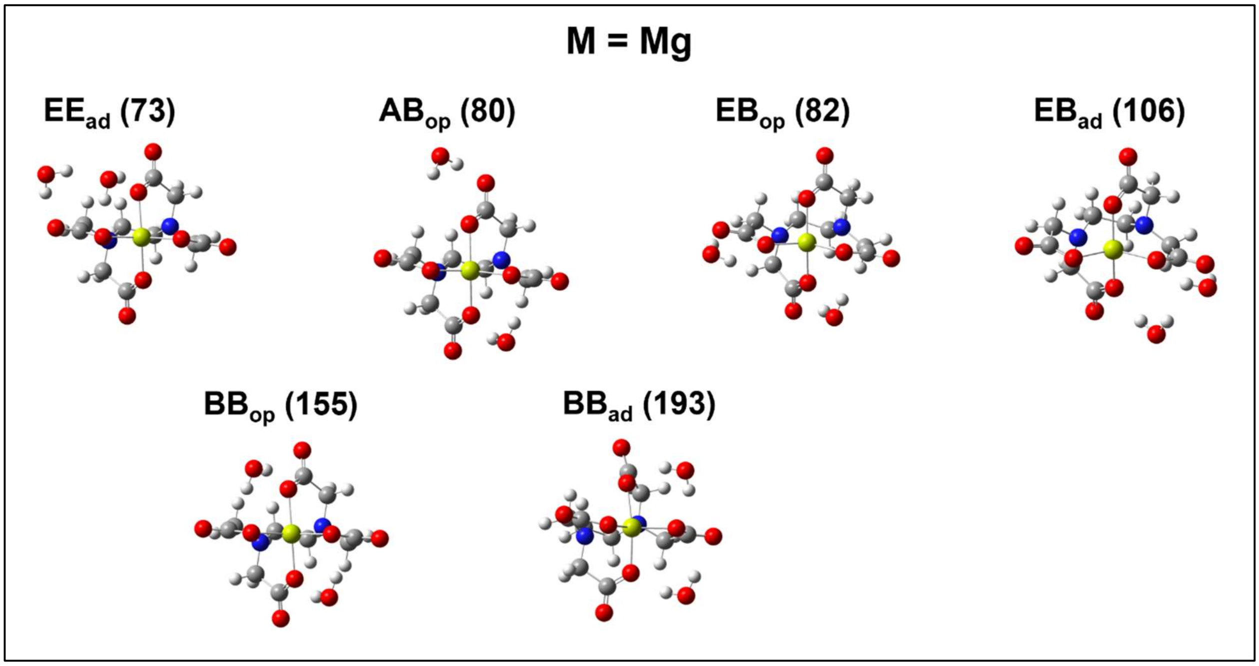

Figure B.2. Calculated dihydrate isomers for M = Mg. The labels include a description of the binding site for each water molecule as defined in Figure 4.9. Subscripts "op" and "ad" mean that the second water molecule binds to opposite or adjacent carboxylate ligands, respectively. Zero-point corrected relative energies above the lowest energy isomer (in meV) are given for each structure. Mg = yellow; O = red; C = grey; H = light grey.

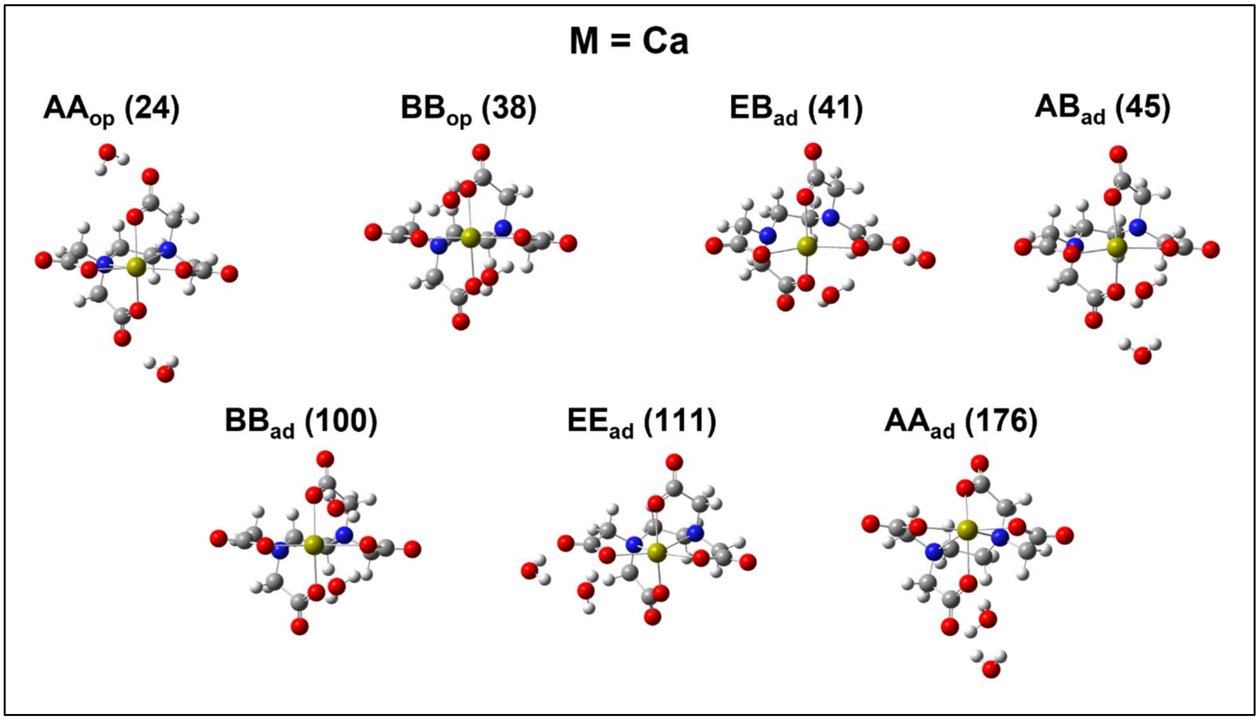

Figure B.3. Calculated dihydrate isomers for M = Ca. The labels include a description of the binding site for each water molecule as defined in Figure 4.9. Subscripts "op" and "ad" mean that the second water molecule binds to opposite or adjacent carboxylate ligands, respectively. Zero-point corrected relative energies above the lowest energy isomer (in meV) are given for each structure. Ca = dark yellow; O = red; C = grey; H = light grey.

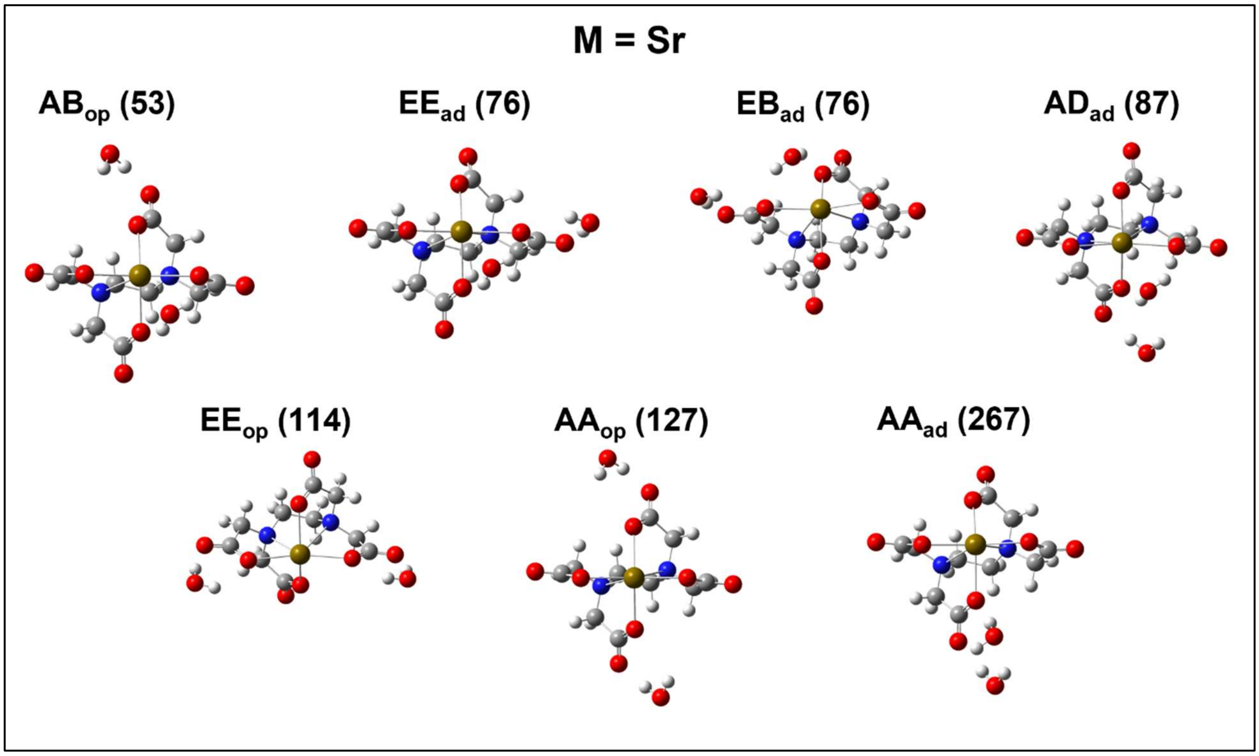

Figure B.4. Calculated dihydrate isomers for M = Sr. The labels include a description of the binding site for each water molecule as defined in Figure 4.9. Subscripts “op” and “ad” mean that the second water molecule binds to opposite or adjacent carboxylate ligands, respectively. Zero-point corrected relative energies above the lowest energy isomer (in meV) are given for each structure. Sr = brown; O = red; C = grey; H = light grey.

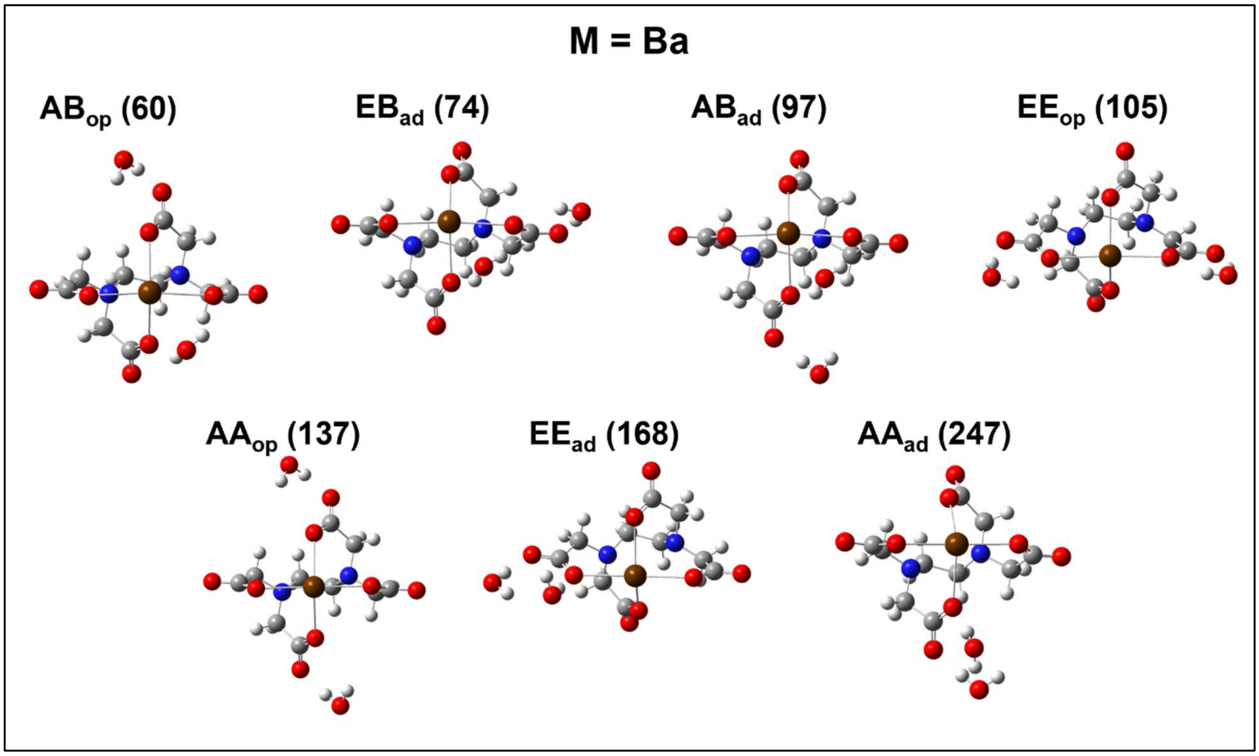

Figure B.5. Calculated dihydrate isomers for M = Ba. The labels include a description of the binding site for each water molecule as defined in Figure 4.9. Subscripts "op" and "ad" mean that the second water molecule binds to opposite or adjacent carboxylate ligands, respectively. Zero-point corrected relative energies above the lowest energy isomer (in meV) are given for each structure. Ba = dark brown; O = red; C = grey; H = light grey.

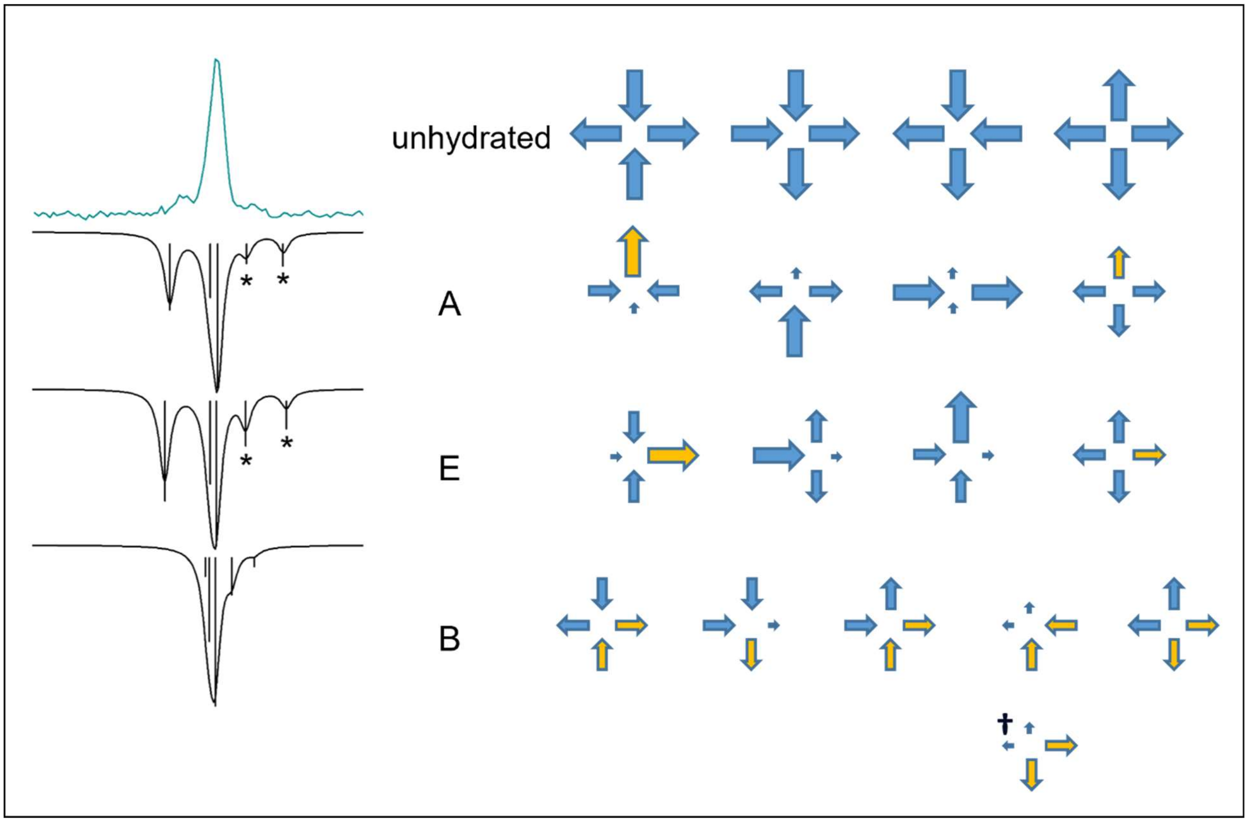

Figure B.6. Patterns of motion of the antisymmetric OCO vibrational modes for unhydrated and monohydrated EDTA complexes, using $[Ca(II) \cdot EDTA]^{2-} \cdot H_2O$ as an example. The patterns are similar for Sr and Ba except for the fourth mode of the Sr bridging isomer, denoted in the figure with †. A, E, and B denote axial, equatorial, and bridging isomers. **Left:** Experimental spectrum (upright) and the simulated spectra of the three isomers (inverted), with calculated frequencies and intensities of the transitions shown as vertical lines. The patterns on the right show the phases (direction) and amplitudes (size of each arrow) of each of the four carboxylate groups. The arrows shown in orange are the hydrated COO^- groups. Each pattern corresponds to one transition in the "stick" spectrum of the corresponding calculated spectrum, in sequence of low to high frequencies. For the A and E isomers, the two modes marked with asterisks have the same pattern on the O–C–O stretching modes, they only differ in the phase of the water bending motion that couples to the O–C–O stretching motions (not shown). For the B isomer, each mode has a characteristic pattern, so all five transitions (O–C–O stretching, mixed with H–O–H bending) are shown.

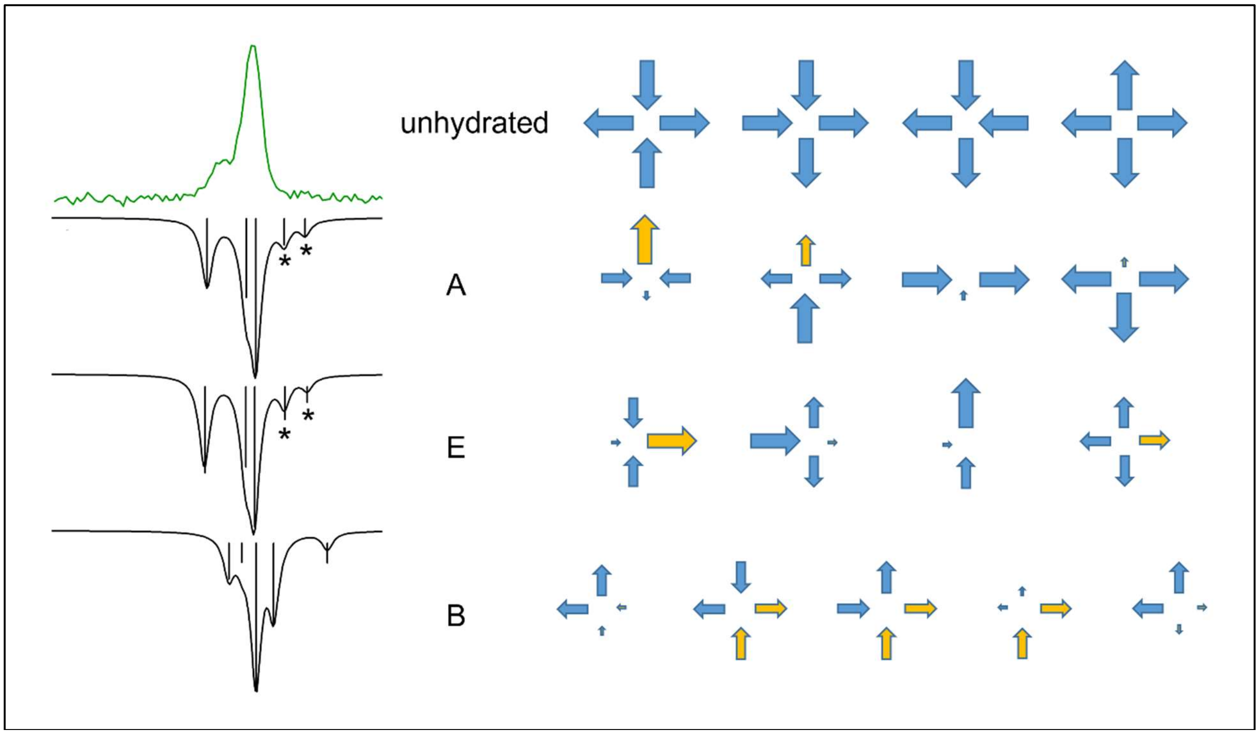

Figure B.7. Patterns of motion of the antisymmetric OCO vibrational modes for unhydrated and monohydrated EDTA complexes, using $[Mg(II)\cdot EDTA]^{2-}\cdot H_2O$ as an example. A, E, and B denote axial, equatorial, and bridging isomers. **Left:** Experimental spectrum (upright) and the simulated spectra of the three isomers (inverted), with calculated frequencies and intensities of the transitions shown as vertical lines. The patterns on the right show the phases (direction) and amplitudes (size of each arrow) of each of the four carboxylate groups. The arrows shown in orange are the hydrated COO^- groups. Each pattern corresponds to one transition in the "stick" spectrum of the corresponding calculated spectrum, in sequence of low to high frequencies. For the A and E isomers, the two modes marked with asterisks have the same pattern on the O–C–O stretching modes, they only differ in the phase of the water bending motion that couples to the O–C–O stretching motions (not shown). For the B isomer, each mode has a characteristic pattern, so all five transitions (O–C–O stretching, mixed with H–O–H bending) are shown.

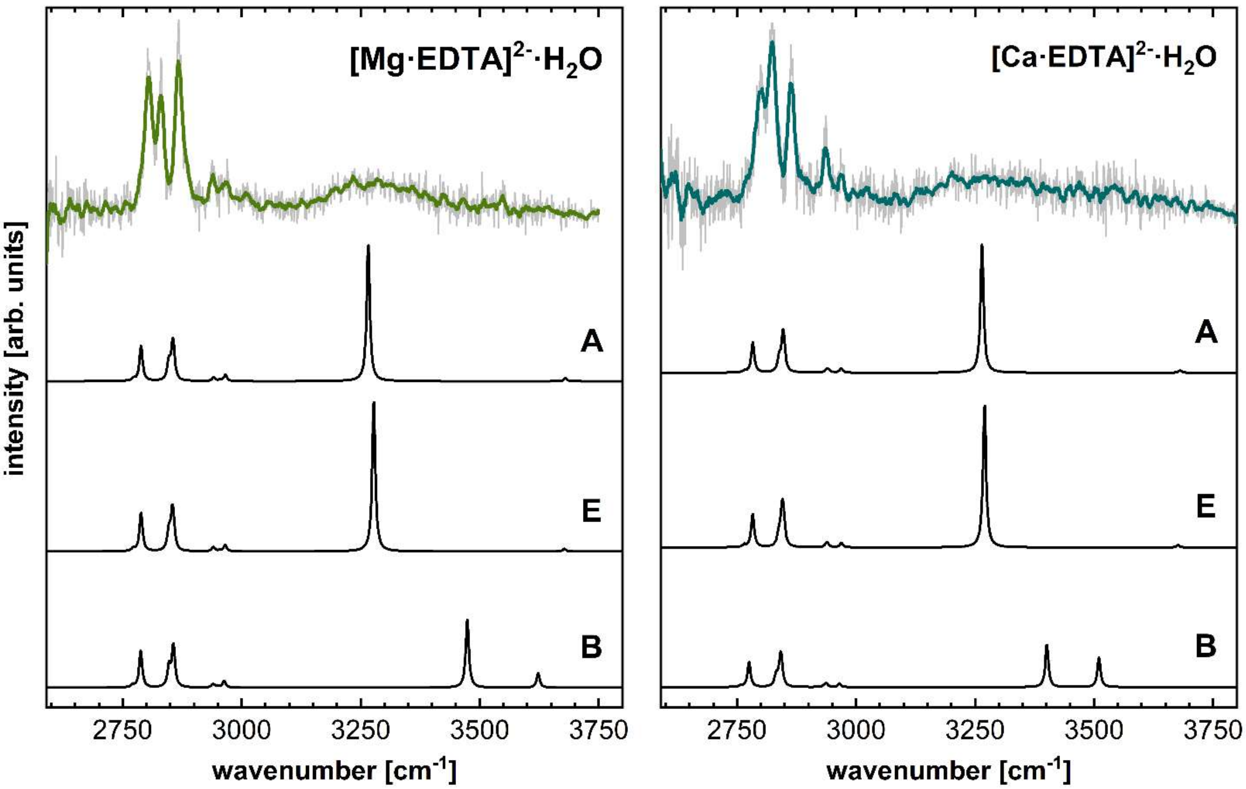

Figure B.8. Spectra of [M(II)·EDTA]$^{2-}$·H_2O in the mid-IR spectral region for M = Mg (left) and Ca (right). The experimental spectra are shown upright, with a 10-point adjacent average (darker line) overlaid to guide the eye. The calculated spectra are shown inverted, labeled with the hydration isomer (see Figure 4.9).

C. Supplementary Information for Chapter 5. On the Bond Angle Dependance of Carboxylate Stretching Frequencies

Table C.1. Experimental values used for empirical fit. Calculated OCO bond angles, experimental values of ν_s, ν_{as}, and $\Delta\nu_{s\text{-}a}$, predicted value of $\Delta\nu_{s\text{-}a}$ based on cosine fit, and error of each calculated value. Stretching energies given in cm^{-1}.

Reference (Ch. 5)	Species	θ_{OCO} [°]	ν_s	ν_as	$\Delta\nu_\mathrm{s\text{-}a}$ (exp)	$\Delta\nu_\mathrm{s\text{-}a}$ (model)	Err.
[13]	CO_2[a]	180.0	1333	2349	1016	1001.6	-14.4
[14]	formate[a]	131.0	1314	1622	308	324.6	16.6
[15]	propionate	128.5	1305	1600	295	264.2	-30.8
[15]	acetate	128.6	1305	1590	285	265.4	-19.6
[16]	*d*-propionate [(*d*-OPr)$^-$]	128.6	1344	1620	276	266.5	-9.5
[16]	*d*-acetate	128.6	1335	1608	273	266.5	-6.5
[16]	Ca^+·*d*-propionate	117.9	1461	1431	-30	-1.6	28.4
[16]	Mg^+·*d*-propionate	117.1	1449	1415	-34	-21.9	12.1
[16]	Ca^+·*d*-acetate	118.0	1459	1440	-19	0.9	19.9
[16]	Mg^+·*d*-acetate	117.2	1457	1414	-43	-19.4	23.6
[17]	benzoate	129.1	1311	1626	315	278.3	-36.7
[17]	*o*-fluorobenzoate	130.5	1300	1650	350	311.9	-38.1
[17]	*m*-fluorobenzoate	129.5	1311	1641	330	288.5	-41.5
[17]	*p*-fluorobenzoate	129.3	1309	1639	330	283.4	-46.6
[17]	*p*-aminobenzoate	128.9	1307	1628	321	274.0	-47.0
[18]	$[Bi\cdot CO_2]^-$	140.9	1169[a]	1725[a]	556	550.2	-5.7
[19]	$[Ag\cdot CO_2]^-$	140.6	1187[a]	1762[a]	575	544.0	-31.0
[20]	(*d*-OPr)$^-$·(H_2O)	127.8	1356	1591	235	246.1	11.1
[20]	(*d*-OPr)$^-$·$(H_2O)_2$	127.6	1374	1588	214	242.9	28.9
[20]	(*d*-OPr)$^-$·$(H_2O)_3$	126.9	1378	1586	208	224.6	16.6
[20]	(*d*-OPr)$^-$·$(H_2O)_4$	126.6	1384	1576	192	217.5	25.5
[20]	(*d*-OPr)$^-$·$(H_2O)_5$	125.3	1375	1599	224	183.8	-40.2
[20]	(*d*-OPr)$^-$·$(H_2O)_6$	126.2	1387	1568	181	207.9	26.9
[20]	[Ca^{2+}·(*d*-OPr)$^-$]$^+$·(H_2O)	119.7	1460	1448	-12	45.1	57.1
[20]	[Ca^{2+}·(*d*-OPr)$^-$]$^+$·$(H_2O)_2$	120.0	1458	1471	13	51.7	38.7
[20]	[Ca^{2+}·(*d*-OPr)$^-$]$^+$·$(H_2O)_3$	120.2	1453	1486	33	57.3	24.3
[20]	[Ca^{2+}·(*d*-OPr)$^-$]$^+$·$(H_2O)_4$	120.5	1451	1494	43	63.9	20.9
[20]	[Ca^{2+}·(*d*-OPr)$^-$]$^+$·$(H_2O)_5$	120.7	1451	1496	45	68.7	23.7
[20]	[Ca^{2+}·(*d*-OPr)$^-$]$^+$·$(H_2O)_6$	120.4	1446	1511	65	61.8	-3.2
[20]	[Ca^{2+}·(*d*-OPr)$^-$]$^+$·$(H_2O)_8$	120.9	1447	1521	74	73.8	-0.2
[20]	[Ca^{2+}·(*d*-OPr)$^-$]$^+$·$(H_2O)_{10}$	120.9	1444	1527	83	73.8	-9.2
[20]	[Ca^{2+}·(*d*-OPr)$^-$]$^+$·$(H_2O)_{12}$	119.7	1448	1536	88	45.0	-43.0

[21]	$CO_2^-\cdot(CO_2)_7$, anion	134.0	1274	1660	386	395.6	9.6
[21]	$CO_2^-\cdot(CO_2)_7$, solvent	179.0	1378	2347	969	1001.2	32.2
[22]	$[O_2^-\cdot CO_2]\cdot CO_2$, cluster	142.7	1265	1938	673	587.9	7.9
[22]	$[O_2^-\cdot CO_2]\cdot CO_2$, tag	172.7	1358	2340	982	984.3	2.6
[23]	$Au\cdot CO_2^-$ (A)	144.1	1236[b]	1896[b]	660	615.5	-44.5
[23]	$Au\cdot CO_2^-$ (B)	170.0	1312[b]	2284[b]	972	969.6	-2.4
	$Cl^-\cdot CO_2$	168.3[c]	1364[c]	2285[c]	921	957.6	36.7
	$Br^-\cdot CO_2$	171.7[c]	1370[c]	2316[c]	947	979.6	32.9

[a] Interpolated from data in the reference.

[b] Unpublished, based on anharmonic calculations performed in the referenced work.

[c] Calculated in the present work.

Table C.2. Geometry calculation information. Calculated C-O bond lengths of each species included in fit and the functional and basis set used to calculate each value.

Reference (Ch. 5)	Species	r_1CO [pm]	r_2CO [pm]	Functional/Basis Set for Geom. Opt.
[13]	CO_2[a]	116.7	116.7	b3lyp/cc-pVDZ
[14]	formate[a]	125.2	125.2	b3lyp/cc-pVDZ
[15]	propionate	126.1	126.2	b3lyp/aug-cc-pVDZ
[15]	acetate	126.2	126.2	b3lyp/aug-cc-pVDZ
[16]	*d*-propionate [(*d*-OPr)$^-$]	124.8	124.8	b3lyp/cc-pVDZ
[16]	*d*-acetate	124.8	124.8	b3lyp/cc-pVDZ
[16]	Ca^+·*d*-propionate	128.0	128.0	cam-b3lyp/6-311++G(3df,3pd)
[16]	Mg^+·*d*-propionate	128.3	128.3	cam-b3lyp/6-311++G(3df,3pd)
[16]	Ca^+·*d*-acetate	127.6	127.6	cam-b3lyp/6-311++G(3df,3pd)
[16]	Mg^+·*d*-acetate	128.0	128.0	b3lyp/aug-cc-pVDZ
[17]	benzoate	125.9	125.9	b3lyp/aug-cc-pVDZ
[17]	*o*-fluorobenzoate	125.6	125.3	b3lyp/aug-cc-pVDZ
[17]	*m*-fluorobenzoate	125.8	125.8	b3lyp/aug-cc-pVDZ
[17]	*p*-fluorobenzoate	125.9	125.9	b3lyp/aug-cc-pVDZ
[17]	*p*-aminobenzoate	126.0	126.0	b3lyp/aug-cc-pVDZ
[18]	$[Bi·CO_2]^-$ *	121.2	121.2	b3lyp/def2-TZVPP
[19]	$[Ag·CO_2]^-$ *	124.9	124.9	b3lyp/def2-TZVPP
[20]	(*d*-OPr)$^-$·(H_2O)	127.5	127.4	MP2/aug-cc-pVDZ
[20]	(*d*-OPr)$^-$·$(H_2O)_2$	126.8	127.8	MP2/aug-cc-pVDZ
[20]	(*d*-OPr)$^-$·$(H_2O)_3$	126.7	128.3	MP2/aug-cc-pVDZ
[20]	(*d*-OPr)$^-$·$(H_2O)_4$	127.5	127.6	MP2/aug-cc-pVDZ
[20]	(*d*-OPr)$^-$·$(H_2O)_5$	125.8	129.5	MP2/aug-cc-pVDZ
[20]	(*d*-OPr)$^-$·$(H_2O)_6$	126.9	128.4	MP2/aug-cc-pVDZ
[20]	$[Ca^{2+}$·(*d*-OPr)$^-]^+$·(H_2O)	130.0	129.1	MP2/aug-cc-pVDZ (Frozen Core)
[20]	$[Ca^{2+}$·(*d*-OPr)$^-]^+$·$(H_2O)_2$	129.2	129.4	MP2/aug-cc-pVDZ (Frozen Core)
[20]	$[Ca^{2+}$·(*d*-OPr)$^-]^+$·$(H_2O)_3$	128.8	129.2	MP2/aug-cc-pVDZ (Frozen Core)
[20]	$[Ca^{2+}$·(*d*-OPr)$^-]^+$·$(H_2O)_4$	128.7	129.0	MP2/aug-cc-pVDZ (Frozen Core)
[20]	$[Ca^{2+}$·(*d*-OPr)$^-]^+$·$(H_2O)_5$	128.1	129.2	MP2/aug-cc-pVDZ (Frozen Core)
[20]	$[Ca^{2+}$·(*d*-OPr)$^-]^+$·$(H_2O)_6$	128.4	128.5	MP2/aug-cc-pVDZ (Frozen Core)
[20]	$[Ca^{2+}$·(*d*-OPr)$^-]^+$·$(H_2O)_8$	128.2	128.5	MP2/aug-cc-pVDZ (Frozen Core)
[20]	$[Ca^{2+}$·(*d*-OPr)$^-$	127.1	129.8	MP2/aug-cc-pVDZ (Frozen Core)

	$]^{+}\cdot(H_2O)_{10}$			
[20]	$[Ca^{2+}\cdot(d\text{-OPr})^{-}]^{+}\cdot(H_2O)_{12}$	127.4	129.3	MP2/aug-cc-pVDZ (Frozen Core)
[21]	$CO_2^{-}\cdot(CO_2)_7$, anion	N/A	N/A	b3lyp-D3/def2-TZVPP
[21]	$CO_2^{-}\cdot(CO_2)_7$, solvent	N/A	N/A	b3lyp-D3/def2-TZVPP
[22]	$[O_2^{-}\cdot CO_2]\cdot CO_2$, cluster	120.6[c]	120.9[c]	b3lyp/TZVPP
[22]	$[O_2^{-}\cdot CO_2]\cdot CO_2$, tag	116.2[c]	116.2[c]	b3lyp/TZVPP
[23]	$Au\cdot CO_2^{-}$ (A)	226.0	226.0	b3lyp/various
[23]	$Au\cdot CO_2^{-}$ (B)	320.0	320.0	b3lyp/various
	$Cl^{-}\cdot CO_2$	116.5[c]	116.5[c]	b3lyp/aug-cc-pvtz
	$Br^{-}\cdot CO_2$	116.3[c]	116.3[c]	b3lyp/aug-cc-pvtz

[a] Interpolated from data in the reference.

[b] Unpublished, based on anharmonic calculations performed in the referenced work.

[c] Calculated in the present work.

Table C.3. Experimental values from [2] in Chapter 5. The OCO bond angles, experimental $\Delta\nu_{s\text{-}a}$ values, reported CO bond lengths, predicted $\Delta\nu_{s\text{-}a}$ splitting, residual $\Delta\nu_{s\text{-}a}$ values, and corrected predicted $\Delta\nu_{s\text{-}a}$ for each selected species from [2].

Compound	OCO angle	$\Delta\nu_{s\text{-}a}$ (exp)	r_1CO [pm]	r_2CO [pm]	Δ rCO [pm]	$\Delta\nu_{s\text{-}a}$ (model)	Residual $\Delta\nu_{s\text{-}a}$	$\Delta\nu_{s\text{-}a}$ (model, corrected for Δ rCO)
$Na[H(O_2CMe)_2]$	121.7	310	130	124	5	94	216	165
$Ph_3Sb(O_2CMe)_2$	121.6	313	130	121	8	91	222	78
$Si(O_2CMe)_4$ (a)	119.3	490	137	120	18	28	462	-8
$Si(O_2CMe)_4$ (b)	119.3	565	137	120	18	28	537	67
$Ni(O_2CMe)_2(H_2O)_4$ (a)	122.5	125	127	126	2	116	9	77
$Ni(O_2CMe)_2(H_2O)_4$ (b)	122.5	107	127	126	2	116	-9	59
$Ni(O_2CMe)_2(H_2O)_2Py_2$	126.4	138	126	125	1	223	-85	102
$Mn(O_2CMe)(CO)_2(Ph_3P)_2$	115.8	83	124	127	3	-69	152	-1
$Ni(O_2CMe)(tet)ClO_4$	121.6	102	125	125	0	91	11	102
$Ru(O_2CMe)H(Ph_3P)_2$	114.9	75	126	126	1	-94	169	53
$Ru(O_2CMe)R(CO)(Ph_3P)_2$	115.4	76	129	130	1	-80	156	48
$NaUO_2(O_2CMe)_3$	121	65	126	128	2	75	-10	9
$[Co_2\ (O_2CMe)NH((CH_2)_3NH_2)_2]ClO_4$	120.4	150	127	127	0	58	92	150
$Li(O_2CMe)(H_2O)_2$	125.7	162	125	125	0	204	-42	162
$Me_3Pb(O_2CMe)$	121.5	145	123	121	2	89	56	95
$Sb_2(O_2CMe)Cl_6O(OH)$	124.2	45	129	126	3	163	-118	-47
$Me_3Sn(O_2CMe)$	122.6	140	127	124	3	119	21	59

ProQuest LLC
789 East Eisenhower Parkway
P.O. Box 1346
Ann Arbor, MI 48106 - 1346 USA